5-2014

Control of Grid-Connected Photovoltaic Systems Using Fractional Order Operators

Hadi Malek
Utah State University

Recommended Citation

Malek, Hadi, "Control of Grid-Connected Photovoltaic Systems Using Fractional Order Operators" (2014). *All Graduate Theses and Dissertations*. 2157.
https://digitalcommons.usu.edu/etd/2157

CONTROL OF GRID-CONNECTED PHOTOVOLTAIC SYSTEMS USING FRACTIONAL ORDER OPERATORS

by

Hadi Malek

A dissertation submitted in partial fulfillment
of the requirements for the degree

of

DOCTOR OF PHILOSOPHY

in

Electrical Engineering

Approved:

Dr. YangQuan Chen Major Professor	Dr. Don Cripps Committee Member
Dr. Heng Ban Committee Member	Dr. Edmund Spencer Committee Member
Dr. Hunter Wu Committee Member	Dr. Mark R. McLellan Vice President for Research and Dean of the School of Graduate Studies

UTAH STATE UNIVERSITY
Logan, Utah

2014

Abstract

Control of Grid-Connected Photovoltaic Systems Using Fractional Order Operators

by

Hadi Malek, Doctor of Philosophy

Utah State University, 2014

Major Professor: Dr. YangQuan Chen
Department: Electrical and Computer Engineering

This work presents a new control strategy using fractional order operators in three-phase grid-connected photovoltaic generation systems with unity power factor for any situation of solar radiation. The modeling of the space vector pulse width modulation inverter and fractional order control strategy using Park's transformation are proposed. The system is able to compensate harmonic components and reactive power generated by the loads connected to the system. A fractional order extremum seeking control and "Bode's ideal cut-off extremum seeking control" are proposed to control the power between the grid and photovoltaic system, to achieve the maximum power point operation. Simulation results are presented to validate the proposed methodology for grid-connected photovoltaic generation systems. The simulation results and theoretical analysis indicate that the proposed control strategy improves the efficiency of the system by reducing the total harmonic distortion of the injected current to the grid and increases the robustness of the system against uncertainties. Additionally, the proposed maximum power point tracking algorithms provide more robustness and faster convergence under environmental variations than other maximum power point trackers.

(159 pages)

Public Abstract

Control of Grid-Connected Photovoltaic Systems Using Fractional Order Operators

by

Hadi Malek, Doctor of Philosophy

Utah State University, 2014

Major Professor: Dr. YangQuan Chen
Department: Electrical and Computer Engineering

This work presents a new peak seeking strategy for maximum power point operation using fractional order operators in the three-phase grid-connected photovoltaic systems. Moreover, fractional order controllers have been implemented in the voltage and current control loops. The simulation results and theoretical analysis indicate that the proposed fractional order control strategy improves the efficiency of the system by reducing the total harmonic distortion of the injected current to the grid and increases the robustness of the system against uncertainties. Additionally, the proposed maximum power point tracking algorithms provide more robustness and faster convergence speed under environmental variations than other maximum power point trackers.

To my parents ...

Acknowledgments

There are many people whom I am indebted to during my Ph.D. study. They have helped me in numerous ways that have enabled this dissertation to come into being. First, and foremost, I wish to thank my supervisor, Dr. YangQuan Chen, for introducing me into the field of Fractional Order Calculus (FOC) and giving me valuable guidance throughout the course of my study. His deep insights and positive manner have always been helpful and encouraging.

Next, special thanks go to my committee members, Dr. Cripps, Dr. Spencer, Dr. Ban, and Dr. Wu, for their numerous help, particularly for their patience in reading my draft dissertation. Their advice and assistance are highly appreciated. I would also like to give special thanks to Dr. Wu who inspired me in the field of power electronics. The friendly academic discussions in the Wireless Power Transfer Group have made my study very productive and interesting. I would like to give special thanks to Dr. Sara Dadras and Mary Lee Anderson who reviewed this dissertation.

Thirdly, I would like to express my gratitude to the Utah State University for bestowing me with a Ph.D scholarship so that I can continue my research interest in the field of power and control. Thanks go to the Utah State Research Foundation for offering me an industrial scholarship as well as technical and experimental assistance.

In addition, I wish to thank Dr. Ali Ghafourian, Majid Khalilikhah, Mohammad Shekaramiz, Dr. Ying Luo, Alex Chu, Calvin Coopmans, Dan Stuart, Austin Jensen, Jinlu Han, and Brandon Stark for their company, friendship, and help.

Last, but not least, I would like to take this limited space to express my gratitude to my mom and dad and brother for their consistent help, support, and in particular, moral support in the journey of my academic career.

Hadi Malek

Contents

List of Tables

List of Figures

Figure Page

Acronyms

AC	Alternative current
BIBO	Bounded input bounded output
BICO	Bode's ideal cut-off frequency
CSI	Current source inverter
DC	Direct current
ESC	Extremum seeking control
FO-ESC	Fractional order extremum seeking control
FO-PI	Fractional order proportional-integral controller
IC	Incremental conductance
IEC	International Electrotechnical Commission
IEEE	Institute of Electrical and Electronics Engineers
IO-ESC	Integer order extremum seeking control
IO-PI	Integer order proportional-integral controller
KCL	Kirchhoff's Current Law
LTI	Linear time invariant
MHCC	Modulated hysteresis current control
MIMO	Multi input multi output
MPC	Model predictive control
MPPT	Maximum power point tracking
PCC	Point of common coupling
PLL	Phase-locked-loop
P&O	Perturb and observe
PV	Photovoltaic
PWM	Pulse width modulation
RMS	Root mean squares
SISO	Single input single output
THD	Total harmonic distortion
SVM	Space vector modulation
VSI	Voltage source inverter

Chapter 1

Introduction

1.1 Solar Energy: An Alternative Energy Resource

At present, the total energy consumption in the world is fourteen tera-watts (TW) at any given moment, and this consumption is estimated to be about two times higher by 2050 [1]. To meet this demand, all forms of energy need to be increased rapidly in the coming years. The use of traditional energy resources such as fossils fuel is not justifiable, due to its pollution and greenhouse gas emissions.

For this reason, there has been rapid development of renewable energy technologies to meet the future energy demand and creates a sustainable free pollution energy economy. Among the various ways of harvesting energy from mother nature, solar energy has become one of the dominant forms due to its availability. According to recent data, the annual energy reaching the earth's surface from the sun is larger than all forms of traditional energy resources that have ever been available, or will ever be available, from all of the non-renewable sources on the earth including oil, coal, natural gas, and nuclear power [2].

Solar energy currently provides only a quarter of a percent of the planet electricity supply; however, this industry is growing at a staggering speed as photovoltaic (PV) panels have the advantage of being almost maintenance and pollution free.

In the past few decades, price and efficiency were two disincentive factors for the growth of PV panels in power generation applications. For instance, the price per watt of crystalline silicon PV modules was 76.67 USD in 1977 compared to 3.00 USD in 2005. More recently, due to the mass production, a further decline has been seen in the price of PV modules. In 2013 the price per watt of similar PV modules was 0.74 USD [3]. Since the price of PV panels is the major contributor in the cost of the whole system, the decrease in price of PV panels has lead power generation companies to focus on this cheap, pollution-free, maintenance-free, and innovative solution.

From an efficiency point of view, as shown in Fig. 1.1, solar cell efficiencies (measured by using the ratio of electrical output power to the total light energy covers a cell) vary from 6% to around 40% [4]. Using high efficiency cells is not always economically justifiable because of the production cost. Energy conversion efficiencies for commercially available solar cells are around 14 to 19%.

In recent years, solar energy demand has grown consistently due to the following factors:

- Increasing efficiency of solar cells,
- Manufacturing technology improvement, and
- Economies of scale.

PV panels can be used either offline or online. In offline applications, PV panels supply local loads which can be residential or commercial. In online applications, these modules not only supply local loads, but also are connected to the utility grid. In this case, the system would be called "grid-connected PV system." Recently, grid-connected PV system installation is increasing tremendously in many countries. Around 75% of the total PV systems installed in the world are grid-connected [5]. In the future, this penetration rate will become larger because of the economical advantages of these types of renewable energy systems.

Generally, one of the challenges of grid-connected renewable energy systems, including solar grid-connected systems, is their compatibility with grid utility because of their different output frequencies. This fact brings up the question of how to incorporate them into a standard utility grid. To solve this issue, these systems have to employ some sort of interface which makes them able to convert their output frequency and inject synchronized power into the grid.

Since the output of PV panels are direct current (in the case of grid-connected PV systems), the interface is typically a DC-AC converter (inverter) which inverts the DC

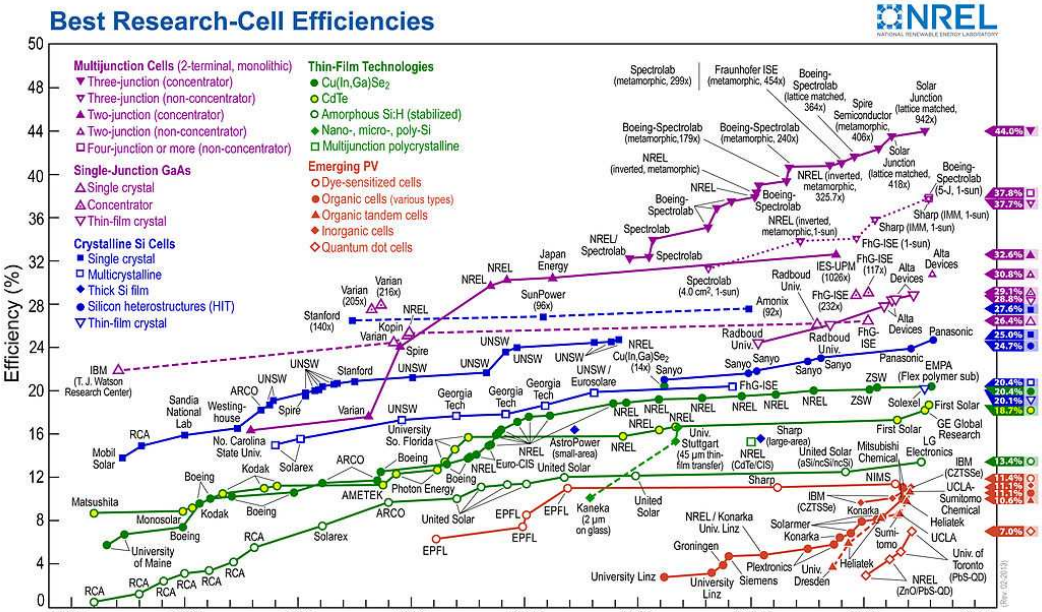

Fig. 1.1: Energy conversion efficiency in some PV cell manufacturers.

output current that comes from the PV arrays into a synchronized sinusoidal waveform as shown in Fig. 1.2 [6].

Another challenge is the way of power extraction from sun and is mostly related to the nature of PV arrays. Each PV module is a nonlinear system that its output power is influenced by solar irradiation and weather conditions. To match the nonlinear output of PV modules with the load for all atmospheric conditions, a maximum power point tracking (MPPT) technique is usually implemented and applied to a grid-connected system to always find and track the maximum power point of the PV panel. The MPPT algorithm is applied to the power conversion stage to adjust the operating point of the system.

Therefore, each grid-connected PV system has to perform two essential functions [7]:

- Extract maximum power output from PV arrays, and
- Inject an almost harmonic free sinusoidal current into the grid.

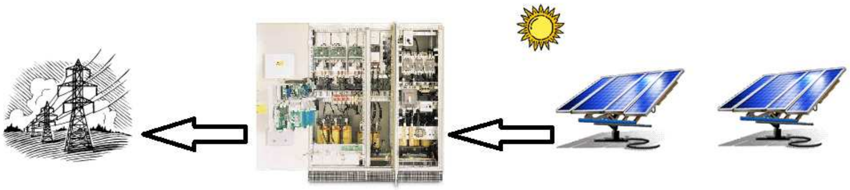

Fig. 1.2: General schematic of grid-connected PV system.

There are numerous ways of injecting synchronized power from PV modules into the utility grid. In each of these approaches, the MPPT and inverters have been implemented with different techniques. In the next section, different structures and topologies for grid-connected inverters will be reviewed and discussed.

1.2 Grid-Connected PV System Topologies

1.2.1 Classification of Inverter Structures

One classification for grid-connected inverters is based on their internal topology. As can be seen in Fig. 1.3, grid-connected inverters for PV panel application are divided into the following categories:

- Current Source Inverter (CSI), or
- Voltage Source Inverter (VSI).

The standard voltage source inverter or current source inverter are the trivial choices to provide single stage DC-AC conversion. Figure 1.3(a) illustrates the standard voltage source inverter topology. The VSI is fed from a DC-link capacitor which is connected in parallel with PV panels. Figure 1.3(b) presents the topology of a standard current source inverter [8]. The inverter is fed from a large DC-link inductor.

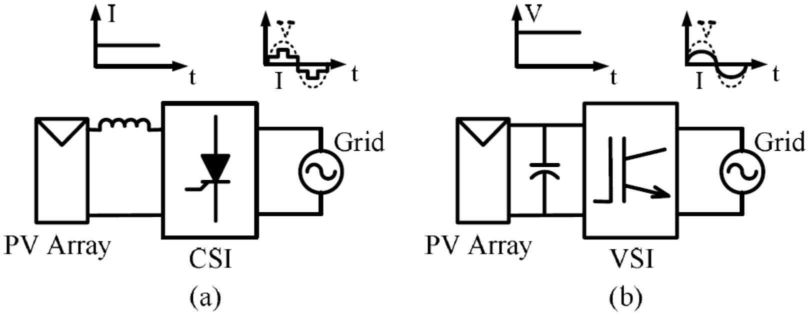

Fig. 1.3: Different topologies of grid-connected PV systems: (a) current source inverter, and (b) voltage source inverter.

1.2.2 Classification of Inverter Configurations

Generally, there are several classifications for inverter configurations with respect to the number of power stages. According to this classification, all the configurations can be divided into three classes [6, 8–12]:

- Single-stage inverters,
- Dual-stage inverters, or
- Multi-stage inverters.

For single-stage inverters, the maximum power point tracking and control loops (current and voltage control loops) are handled all in one stage (Fig. 1.4(a)). For dual-stage inverters, the maximum power point tracking is handled by additional DC-DC converter in between the PV panels and inverter, and control loops are applied to the inverter (Fig. 1.4(b)). For multi-stage inverters, a DC-DC converter takes care of the maximum power point tracking control of each string and one control inverter handles the control loops (Fig. 1.4(c)) [6].

Despite these classifications for grid connected PV systems, for commercial applications there are four acceptable configurations [6]:

- Central plant inverter,
- Multiple string DC-DC converter,

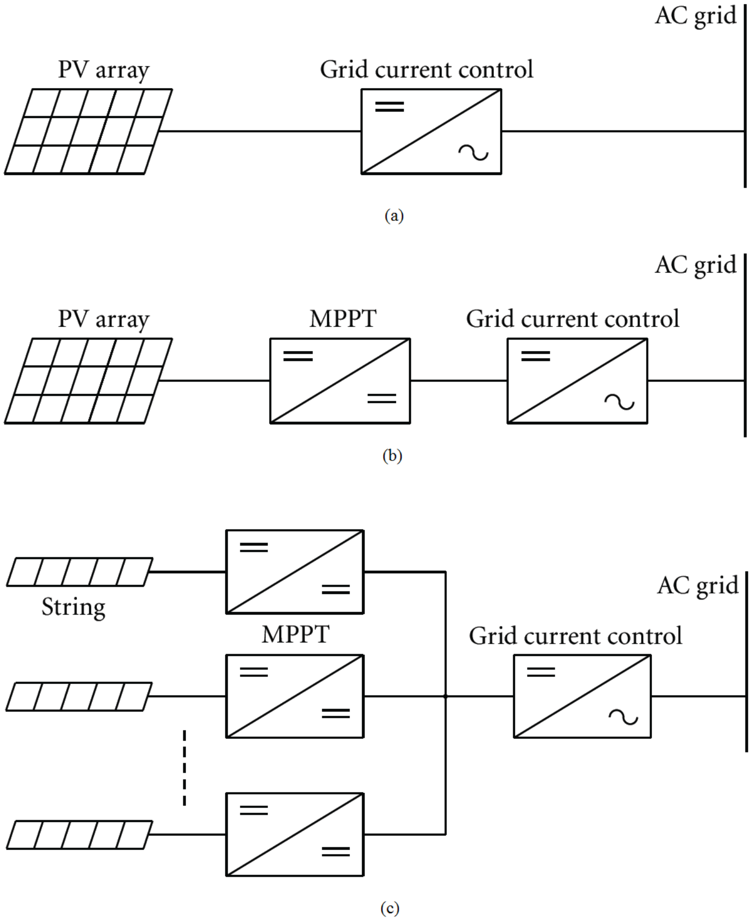

Fig. 1.4: Different configurations of inverters: (a) single-stage inverter, (b) dual-stage inverter, and (c) multi-stage inverter.

- Multiple string inverter, or
- Module integrated inverter.

The central plant inverter configuration as shown in Fig. 1.5(a) consists of a large capacity inverter which is interfaced between the PV modules and utility grid to convert the output DC to AC power [6]. The PV modules are divided into series connections (called strings) and the series strings are connected in parallel. The strings produce sufficiently high voltage, and the parallel connections increase the output power level.

As can be seen in Fig. 1.5(b), the multiple string DC-DC converter employs an additional DC-DC converter between each string and the common DC link which feeds the inverter [6].

Figure 1.5(c) illustrates the multiple string inverter configuration which includes one inverter for each string of PV modules [6]. The outputs of these inverters are fed directly into the utility grid.

In module integrated inverters, as shown in Fig. 1.5(d), each PV module has its own inverter which is synchronized with the utility grid.

There are some advantages and disadvantages in using each of these configurations. As mentioned earlier, since the efficiency of commercial PV modules is not high ($< 20\%$), extracting and delivering the most achievable power to the utility grid is one of the most important factors in grid-connected PV systems. To reach this goal, the inverter (converter) is designed to achieve high power conversion efficiency.

Additionally, the inverter (converter) cost per watt is as important as efficiency of the inverter (converter) because these two factors (efficiency and manufacturing cost) directly influence final price of the generated power.

Typically, a single-stage (central plant) inverter has higher efficiency, lower cost, and higher reliability, since the chance of component failure is lower (with respect to other configurations with higher number of components). However, this configuration requires higher DC voltage in order to provide voltage/var control [13]. Also, it has been indicated

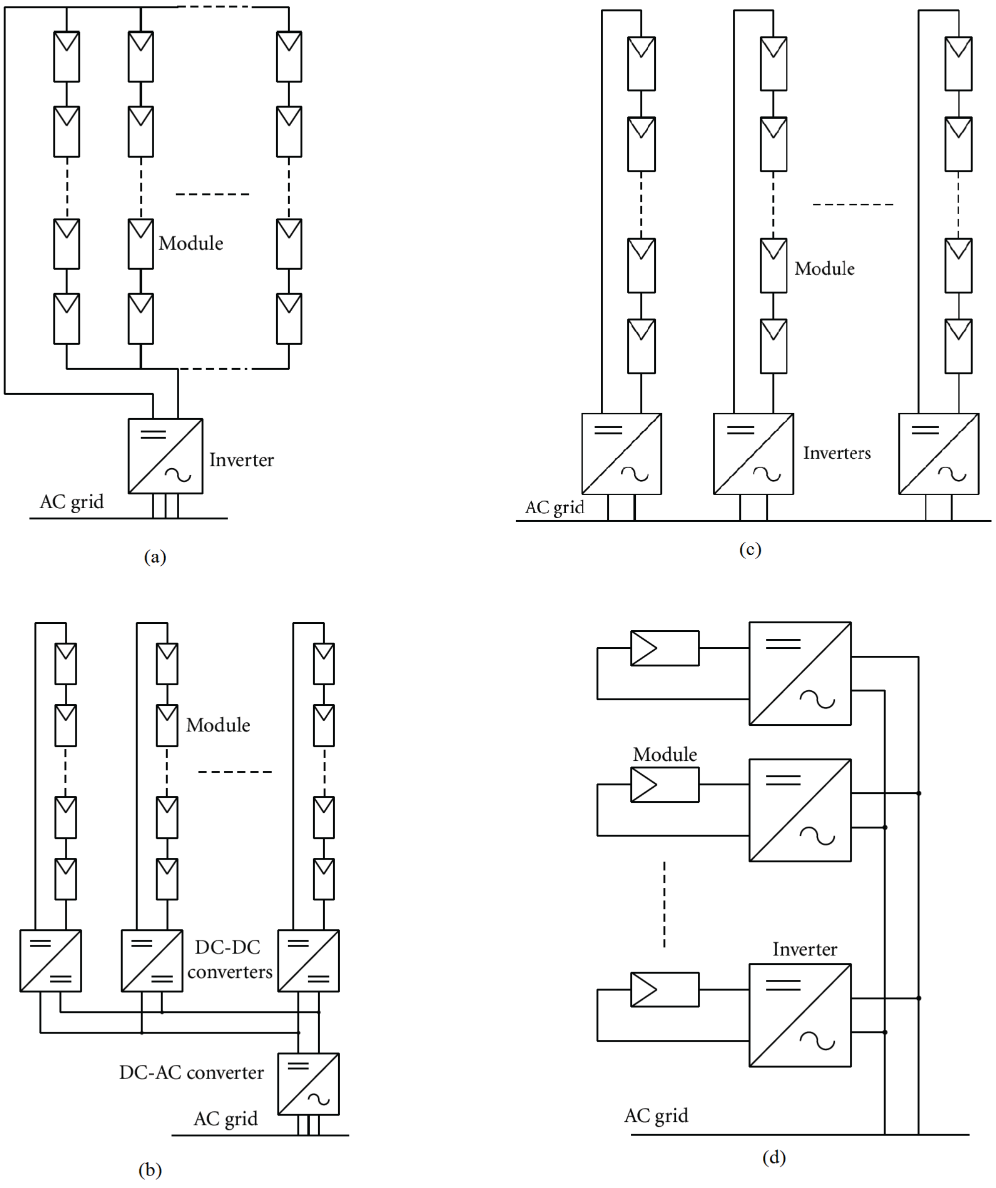

Fig. 1.5: Different commercial configurations of grid-connected PV systems: (a) central plant inverter, (b) multiple string DC-DC converter, (c) multiple string inverter, and (d) module integrated inverter.

that eliminating a DC-DC converter stage reduces the total cost of grid-connected PV systems [14] and makes this option more attractive on the market.

The other feature which affects the design structure of grid-connected PV systems is the use of a single-phase or a three-phase system. From the inverter structure point of view, in high-power applications, using a three-phase system has the following advantages [6]:

- Decreasing the stresses on the inverter switches,
- Reducing the size and ratings of reactive components,
- Increasing the frequency of output current which reduces the size of output filter, and
- Creating a uniform distribution of losses.

Therefore, a three-phase single-stage grid-connected PV system has been considered in this work (Fig. 1.6). Inverter interfacing PV module(s) with the grid involves different requirements and standards. In the next section, these topics will be discussed.

1.3 Grid-Connected PV Standards and Demands

As the capacity of PV systems is growing significantly, the impact of PV modules on utility grids cannot be ignored. Grid-connected PV systems can cause problems on the grid, such as injecting more harmonics or reducing the stability level or margin by exciting the resonant mode of the power system [15]. This problem can be severe when a large scale PV module is connected to the grid. Current harmonics produce voltage distortions, current distortions, and cause unsatisfactory operation of power systems.

Therefore, harmonic mitigation plays an essential role in grid-connected PV system. To both increase the capacity of PV arrays and maintain power quality, it is necessary to comply with some requirements such as harmonic compensation [16].

The IEEE Standard [17], which was introduced in 1981 and revised in 2003, provides direction on dealing with harmonics produced by static power converters and nonlinear loads. This standard helps to prevent harmonics from negatively affecting the utility grid.

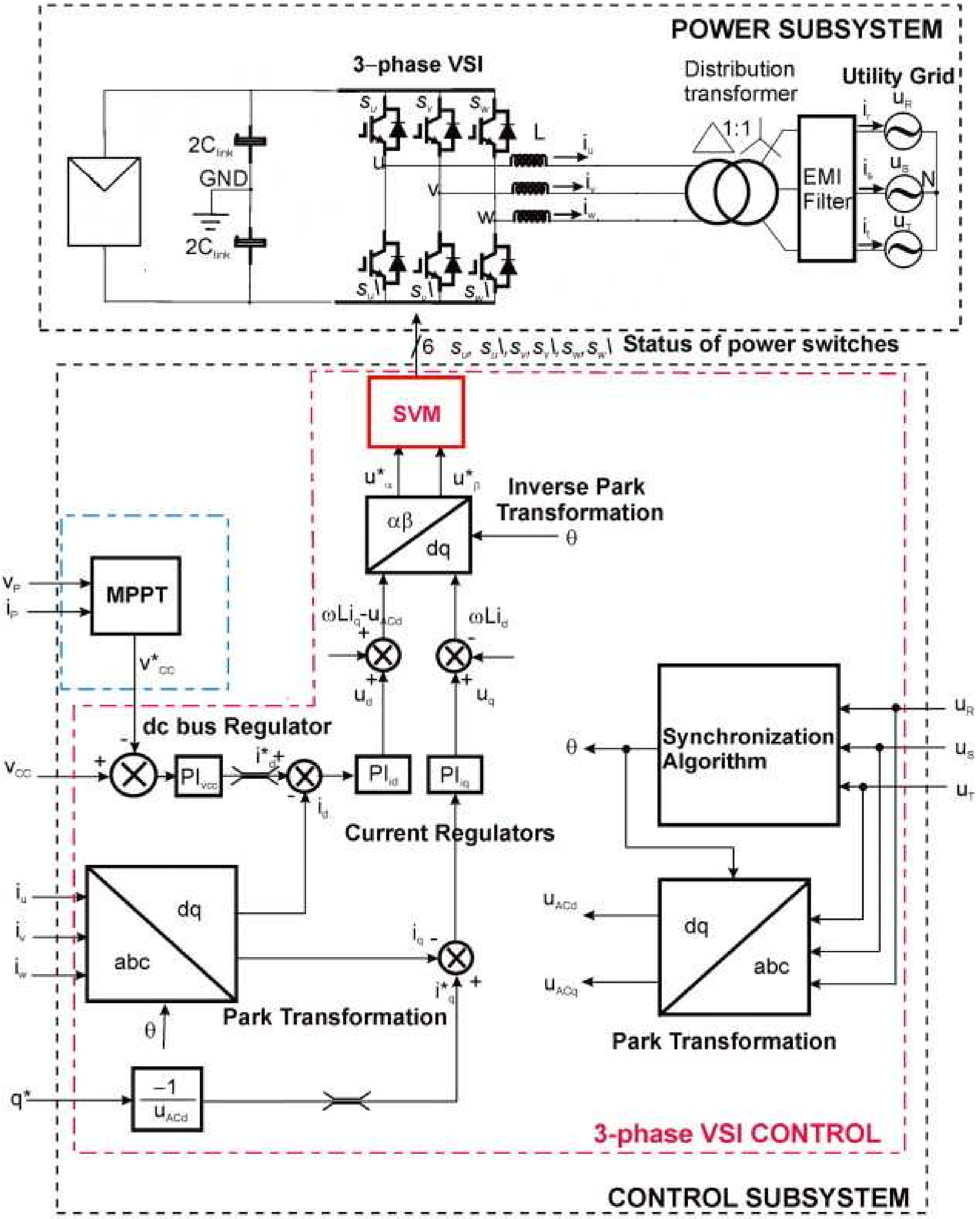

Fig. 1.6: A grid-connected PV system scheme.

To design a grid-connected PV system, in addition to grid standards, other demands and constraints is preferably required. These constraints can be divided into the following three categories:

- Demands defined by the grid,
- Demands defined by the PV modules, and
- Demands defined by customers.

1.3.1 Demands Defined by the Grid

Since the output of any grid-tie inverter is eventually connected to a utility grid, the standards given by the utility companies must be obeyed. These standards deal with power quality, detection of islanding operation, grounding, etc. For instance, the negative pole of the PV panels must be grounded.

Typically, grid-connected PV systems do not control and observe the voltage of the utility grid. Therefore, the inverter must respond to any unusual grid condition in a certain amount of time (depend on the voltage level) in order to prevent islanding. The maximum allowable response time for a grid-tie inverter to cut the energy, in the situation of occurring an event in the grid, are listed in Table 1.1 [18].

In this table, V_{nom} is the RMS nominal voltage of the grid at the point of common coupling (PCC).

Also, according to these standards ($IEC61727$ and $IEEE929$), the allowable injected DC current to the grid has to be less than 0.5% of the rated inverter output current into the

Table 1.1: Maximum trip time for grid-connected systems.

Voltage	Maximum time to cut the injected energy
$V < 50\%V_{nom}$	0.1s
$50\%V_{nom} \leq V < 85\%V_{nom}$	2.0s
$85\%V_{nom} \leq V < 110\%V_{nom}$	Continuous operation
$110\%V_{nom} \leq V < 135\%V_{nom}$	2.0s
$135\%V_{nom} \leq V$	0.05s

utility grid under any operating condition [18]. The IEEE [17] and the IEC [11] standards define these requirements on the maximum allowable amount of injected DC current into the grid to avoid saturation of the distribution transformers [9].

Moreover, if the grid frequency deviates outside of a specified range, the inverter must stop injecting power to the grid within a specified time. The acceptable operating frequency and trip time limit for North America have been defined in $IEEE929$. According to this standard, the frequency operating range is between $59.3 - 60.5$Hz, and the inverter has to cease to energize the grid within 6 cycles (0.1s) in the case of detecting out of range frequencies on the utility grid. [18].

Beside these requirements, it is desirable to have a low level of injected current harmonics into the grid. The allowable current distortion that converter can inject into the grid is given in Table 1.2 [18].

Power factor is another constraint that should be considered when designing an inverter. The inverter should have a power factor greater than 0.85 when the output of inverter is greater than 10% of the rated output power and it should be greater than 0.9 if the output of inverter is greater than 50% of the rated output power [18].

Some of the key points of these standards are listed in Table 1.3 [19].

1.3.2 Demands Defined by the Photovoltaic Module(s)

As mentioned before, to extract the maximum power from each PV module, implementation of MPPT algorithm is highly required in all PV systems. The maximum allowable

Table 1.2: Distortion limitation.

Odd harmonic order h	THD of odd harmonics	THD of even harmonics
THD	5%	25% of odd harmonic limit
3rd - 9th	< 4.0%	25% of odd harmonic limit
11th - 15th	< 2.0%	25% of odd harmonic limit
17th - 21st	< 1.5%	25% of odd harmonic limit
23rd - 33rd	< 0.6%	25% of odd harmonic limit
>33rd	< 0.3%	25% of odd harmonic limit

Table 1.3: IEEE and IEC standards.

Issue	$IEC61727$	$IEEE1547$
Nominal power	$10kW$	$30kW$
Maximum current THD	5%	5%
Power factor at 50% of rated power	0.90	0.90
Voltage range for Nominal operation	$85\% - 110\%$ (196V-121V)	$88\% - 110\%$ (97V-121V)
Frequency range	$50 \pm 1Hz$	59.3Hz - 60.5Hz
DC current injection	$< 1\% I_{out}$	$< 0.5\% I_{out}$

voltage ripple in the output terminal of PV panel is given as [20]

$$\hat{V} = \sqrt{\frac{2(K_{PV} - 1)P_{MPP}}{3\alpha V_{MPP} + \beta}} = 2\sqrt{\frac{(K_{PV} - 1)P_{MPP}}{\frac{d^2 p_{pv}}{dv_{pv}^2}}}, \tag{1.1}$$

where $\hat{V}$ is the maximum amplitude of desired voltage ripples, P_{MPP} and U_{MPP} are the power and voltage at the maximum power point, α and β are the coefficients of second order polynomial which is used for the curve fitting of the behavior of current versus voltage ($i_{PV} = \alpha V_{PV}^2 + \beta V_{PV} + \gamma$), and K_{PV} (utilization ratio) is the average generated power divided by the theoretical maximum power point.

According to (1.1), in order to obtain a utilization ratio of 98%, the amplitude of the ripple voltage is required to be lower than 8.5% of the MPP voltage [20]. For example, in a PV module with a maximum power point voltage of $35V$, the voltage ripple should not exceed $3.0V$ (amplitude), in order to have a utilization ratio of 98%.

1.3.3 Demands Defined by the Operator

As discussed before, output voltage and power of a PV system are influenced by solar irradiation and ambient temperature. Since these two parameters vary in a very wide range, from the operator's point of view, a grid-connected PV system is required to have a high efficiency over a wide range of output voltage and output power.

Figure 1.7 shows the average irradiation range during a normal year in Utah, USA

[21]. Delivering a high efficiency conversion in such a wide range of variations is highly desirable in the grid-connected PV systems. Furthermore, a grid-connected PV system must be highly reliable and have a long operational lifetime [22].

1.4 Literature Review

This research focuses on a three-phase single-stage grid-connected PV system, as depicted in Fig. 1.6 [23]. In this system, a DC-AC inverter has been interfaced between the PV modules and utility grid. The inverter operates in the current controlled mode to ensure a high-power factor is achieved. An inductor output filter is employed to reduce the current ripples due to the switching operation.

Typically, a three-phase Voltage Source Inverter (VSI), in most applications and especially in the grid-connected application, requires a fast dynamic response and high performance current controller to meet the standard requirements. Consequently, the preliminary design objectives are to simultaneously maximize the closed-loop controller bandwidth to achieve a fast transient response and minimize the steady state tracking error. These objectives must be balanced with ensuring that the system is stable and robust and can maintain the standard requirements in the presence of system parameter variations, measurement noises and uncertainties. All the VSI current control techniques discussed in the literature are analyzed for advantages and disadvantages to satisfy these objectives [24,25].

Various control strategies have been proposed on grid-connected PV systems. Although these control strategies can achieve the same goals, their performances are quite different. Three major controllers have been widely investigated over the last few decades: hysteresis regulators, linear PI regulators and predictive dead-beat regulators [25–27].

The advantages of hysteresis controllers are their simplicity, fast dynamic response, and robustness. The major drawback of this type of controller is an uneven and random switching frequency pattern, due to the variation of current reference or DC-link voltage, which makes the filtering of output waveform quite expensive. Moreover, it results in additional stresses on the switching devices [26, 28, 29]. Although there are a number of active researches to improve the hysteresis current control technique [30–32], but applying

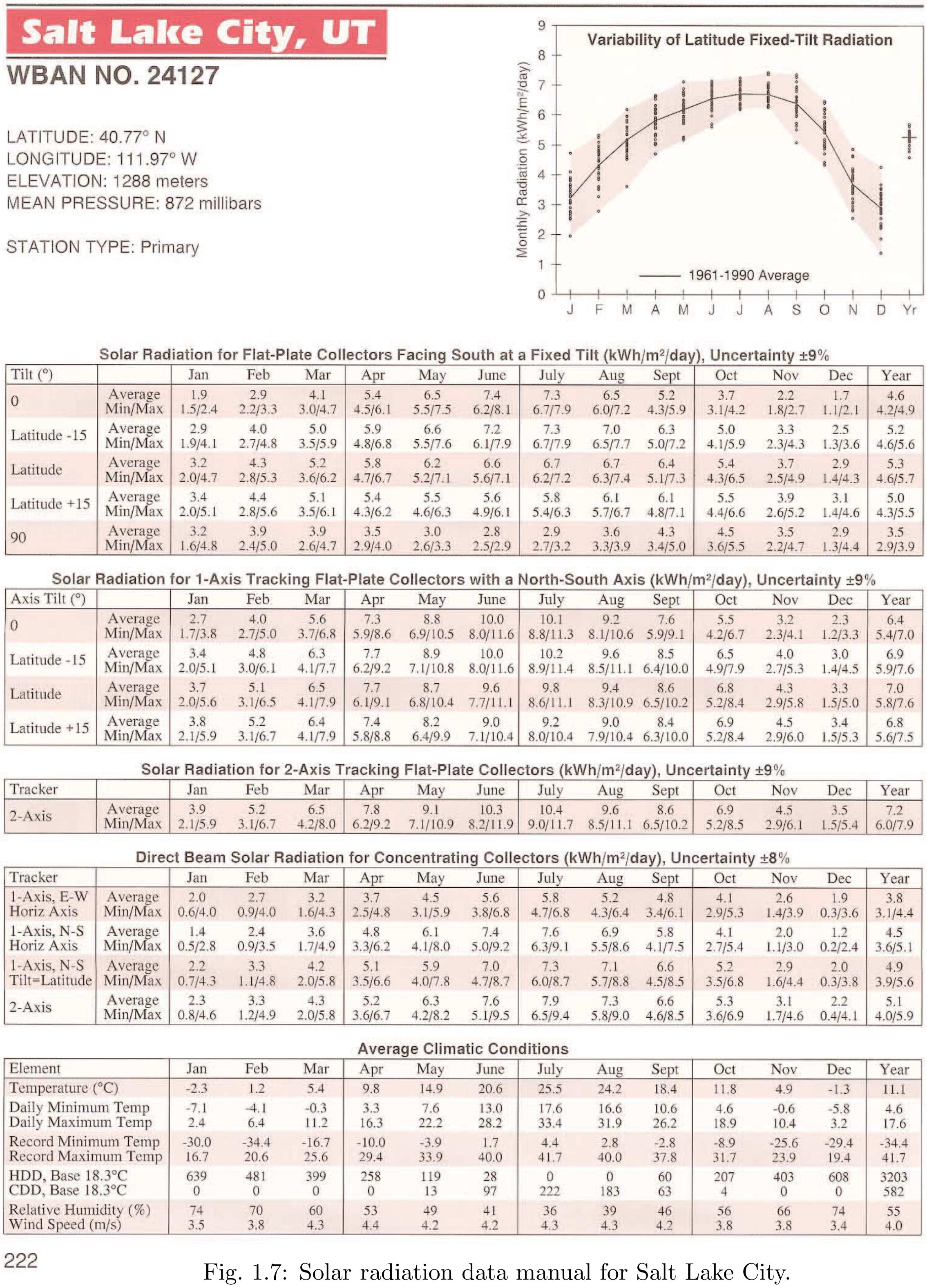

Salt Lake City, UT

WBAN NO. 24127

LATITUDE: 40.77° N
LONGITUDE: 111.97° W
ELEVATION: 1288 meters
MEAN PRESSURE: 872 millibars

STATION TYPE: Primary

Solar Radiation for Flat-Plate Collectors Facing South at a Fixed Tilt (kWh/m²/day), Uncertainty ±9%

Tilt (°)		Jan	Feb	Mar	Apr	May	June	July	Aug	Sept	Oct	Nov	Dec	Year
0	Average	1.9	2.9	4.1	5.4	6.5	7.4	7.3	6.5	5.2	3.7	2.2	1.7	4.6
	Min/Max	1.5/2.4	2.2/3.3	3.0/4.7	4.5/6.1	5.5/7.5	6.2/8.1	6.7/7.9	6.0/7.2	4.3/5.9	3.1/4.2	1.8/2.7	1.1/2.1	4.2/4.9
Latitude -15	Average	2.9	4.0	5.0	5.9	6.6	7.2	7.3	7.0	6.3	5.0	3.3	2.5	5.2
	Min/Max	1.9/4.1	2.7/4.8	3.5/5.9	4.8/6.8	5.5/7.6	6.1/7.9	6.7/7.9	6.5/7.7	5.0/7.2	4.1/5.9	2.3/4.3	1.3/3.6	4.6/5.6
Latitude	Average	3.2	4.3	5.2	5.8	6.2	6.6	6.7	6.7	6.4	5.4	3.7	2.9	5.3
	Min/Max	2.0/4.7	2.8/5.3	3.6/6.2	4.7/6.7	5.2/7.1	5.6/7.1	6.2/7.2	6.3/7.4	5.1/7.3	4.3/6.5	2.5/4.9	1.4/4.3	4.6/5.7
Latitude +15	Average	3.4	4.4	5.1	5.4	5.5	5.6	5.8	6.1	6.1	5.5	3.9	3.1	5.0
	Min/Max	2.0/5.1	2.8/5.6	3.5/6.1	4.3/6.2	4.6/6.3	4.9/6.1	5.4/6.3	5.7/6.7	4.8/7.1	4.4/6.6	2.6/5.2	1.4/4.6	4.3/5.5
90	Average	3.2	3.9	3.9	3.5	3.0	2.8	2.9	3.6	4.3	4.5	3.5	2.9	3.5
	Min/Max	1.6/4.8	2.4/5.0	2.6/4.7	2.9/4.0	2.6/3.3	2.5/2.9	2.7/3.2	3.3/3.9	3.4/5.0	3.6/5.5	2.2/4.7	1.3/4.4	2.9/3.9

Solar Radiation for 1-Axis Tracking Flat-Plate Collectors with a North-South Axis (kWh/m²/day), Uncertainty ±9%

Axis Tilt (°)		Jan	Feb	Mar	Apr	May	June	July	Aug	Sept	Oct	Nov	Dec	Year
0	Average	2.7	4.0	5.6	7.3	8.8	10.0	10.1	9.2	7.6	5.5	3.2	2.3	6.4
	Min/Max	1.7/3.8	2.7/5.0	3.7/6.8	5.9/8.6	6.9/10.5	8.0/11.6	8.8/11.3	8.1/10.6	5.9/9.1	4.2/6.7	2.3/4.1	1.2/3.3	5.4/7.0
Latitude -15	Average	3.4	4.8	6.3	7.7	8.9	10.0	10.2	9.6	8.5	6.5	4.0	3.0	6.9
	Min/Max	2.0/5.1	3.0/6.1	4.1/7.7	6.2/9.2	7.1/10.8	8.0/11.6	8.9/11.4	8.5/11.1	6.4/10.0	4.9/7.9	2.7/5.3	1.4/4.5	5.9/7.6
Latitude	Average	3.7	5.1	6.5	7.7	8.7	9.6	9.8	9.4	8.6	6.8	4.3	3.3	7.0
	Min/Max	2.0/5.6	3.1/6.5	4.1/7.9	6.1/9.1	6.8/10.4	7.7/11.1	8.6/11.1	8.3/10.9	6.5/10.2	5.2/8.4	2.9/5.8	1.5/5.0	5.8/7.6
Latitude +15	Average	3.8	5.2	6.4	7.4	8.2	9.0	9.2	9.0	8.4	6.9	4.5	3.4	6.8
	Min/Max	2.1/5.9	3.1/6.7	4.1/7.9	5.8/8.8	6.4/9.9	7.1/10.4	8.0/10.4	7.9/10.4	6.3/10.0	5.2/8.4	2.9/6.0	1.5/5.3	5.6/7.5

Solar Radiation for 2-Axis Tracking Flat-Plate Collectors (kWh/m²/day), Uncertainty ±9%

Tracker		Jan	Feb	Mar	Apr	May	June	July	Aug	Sept	Oct	Nov	Dec	Year
2-Axis	Average	3.9	5.2	6.5	7.8	9.1	10.3	10.4	9.6	8.6	6.9	4.5	3.5	7.2
	Min/Max	2.1/5.9	3.1/6.7	4.2/8.0	6.2/9.2	7.1/10.9	8.2/11.9	9.0/11.7	8.5/11.1	6.5/10.2	5.2/8.5	2.9/6.1	1.5/5.4	6.0/7.9

Direct Beam Solar Radiation for Concentrating Collectors (kWh/m²/day), Uncertainty ±8%

Tracker		Jan	Feb	Mar	Apr	May	June	July	Aug	Sept	Oct	Nov	Dec	Year
1-Axis, E-W Horiz Axis	Average	2.0	2.7	3.2	3.7	4.5	5.6	5.8	5.2	4.8	4.1	2.6	1.9	3.8
	Min/Max	0.6/4.0	0.9/4.0	1.6/4.3	2.5/4.8	3.1/5.9	3.8/6.8	4.7/6.8	4.3/6.4	3.4/6.1	2.9/5.3	1.4/3.9	0.3/3.6	3.1/4.4
1-Axis, N-S Horiz Axis	Average	1.4	2.4	3.6	4.8	6.1	7.4	7.6	6.9	5.8	4.1	2.0	1.2	4.5
	Min/Max	0.5/2.8	0.9/3.5	1.7/4.9	3.3/6.2	4.1/8.0	5.0/9.2	6.3/9.1	5.5/8.6	4.1/7.5	2.7/5.4	1.1/3.0	0.2/2.4	3.6/5.1
1-Axis, N-S Tilt=Latitude	Average	2.2	3.3	4.2	5.1	5.9	7.0	7.3	7.1	6.6	5.2	2.9	2.0	4.9
	Min/Max	0.7/4.3	1.1/4.8	2.0/5.8	3.5/6.6	4.0/7.8	4.7/8.7	6.0/8.7	5.7/8.8	4.5/8.5	3.5/6.8	1.6/4.4	0.3/3.8	3.9/5.6
2-Axis	Average	2.3	3.3	4.3	5.2	6.3	7.6	7.9	7.3	6.6	5.3	3.1	2.2	5.1
	Min/Max	0.8/4.6	1.2/4.9	2.0/5.8	3.6/6.7	4.2/8.2	5.1/9.5	6.5/9.4	5.8/9.0	4.6/8.5	3.6/6.9	1.7/4.6	0.4/4.1	4.0/5.9

Average Climatic Conditions

Element	Jan	Feb	Mar	Apr	May	June	July	Aug	Sept	Oct	Nov	Dec	Year
Temperature (°C)	-2.3	1.2	5.4	9.8	14.9	20.6	25.5	24.2	18.4	11.8	4.9	-1.3	11.1
Daily Minimum Temp	-7.1	-4.1	-0.3	3.3	7.6	13.0	17.6	16.6	10.6	4.6	-0.6	-5.8	4.6
Daily Maximum Temp	2.4	6.4	11.2	16.3	22.2	28.2	33.4	31.9	26.2	18.9	10.4	3.2	17.6
Record Minimum Temp	-30.0	-34.4	-16.7	-10.0	-3.9	1.7	4.4	2.8	-2.8	-8.9	-25.6	-29.4	-34.4
Record Maximum Temp	16.7	20.6	25.6	29.4	33.9	40.0	41.7	40.0	37.8	31.7	23.9	19.4	41.7
HDD, Base 18.3°C	639	481	399	258	119	28	0	0	60	207	403	608	3203
CDD, Base 18.3°C	0	0	0	0	13	97	222	183	63	4	0	0	582
Relative Humidity (%)	74	70	60	53	49	41	36	39	46	56	66	74	55
Wind Speed (m/s)	3.5	3.8	4.3	4.4	4.2	4.2	4.3	4.3	4.2	3.8	3.8	3.4	4.0

222

Fig. 1.7: Solar radiation data manual for Salt Lake City.

the variable frequency noises into the utility grid is not recommended because it can trigger unpredictable resonances in the grid utility [26].

The other control strategy which has been applied to the grid-connected system is the model predictive control (MPC). The advantages of predictive dead-beat control are fast dynamic response and accurate reference tracking. However, this controller has a model-based regulator and therefore it is quite sensitive to parameter variations, uncertainties, inaccuracies and delays [26, 28, 33, 34].

In several research studies, proportional-integral (PI) controllers are employed to control the AC side currents [25, 26, 35–40]. In these control schemes, the DC-link voltage is controlled by a voltage control loop, where a PI controller acts on the DC voltage error to generate references for the AC current in the stationary (*abc* or *dq*) or synchronous (*dq*) frames. PI current regulators ensure that a clean, in phase AC current feeds the grid [29]. Since the reference signals for the current controllers in this scheme are sinusoidal, a PI controller implemented in standard way under a stationary frame is not able to adequately track these references, and this results in steady-state error due to the limited controller gain at the frequency of interest [41]. In contrast, since usually a PI controller can guarantee zero tracking error on constant signals, if a PI controller is implemented in the *dq* reference frame, without any additional provisions, will be able to track the DC reference and the tracking error will be zero [26].

The other method to control the voltage and current in a three-phase inverter is using a Proportional Resonant (PR) regulator in the stationary frame, which is the equivalent form of a PI regulator in the synchronous frame [26].

Since PI controller has been largely used in the grid-connected PV systems, this controller will be benchmarked for this research to compare with the fractional order controllers. Fractional order controllers, which use fractional order operators in their structures, provides more robustness and more degree of freedom compared to the integer order controllers.

Since solar radiation and ambient temperature variations have a fractional order dynamics [42], and because some sub-components of PV systems (for instance, storage devices) have shown fractionality in their dynamics [43], fractional order controllers are more compatible with the nature of these types of systems. This compatibility will improve the performance and efficiency of power conversion.

In the last decade, the generalized form of PI and PID controllers, fractional order PI (FO-PI) and fractional order PID (FO-PID) controllers, have been investigated widely in various practical systems and have shown better performance especially in the transient states [36, 44–47]. Although fractional order controllers have been successfully applied to other fields of science (from modeling to control aspects), there is limited amount of research efforts on the applications of these controllers in the power electronics systems.

Several research studies present some alternative methods for the control of power electronic buck converters applying fractional order control [48, 49]. The controller design methods are given, and simulations and experimental step responses are presented in order to show the performance of the controlled system and the flexibility and feasibility of this methods.

In other studies, a new control strategy is proposed for the variable speed operation of wind turbines with PMSG/full power converter topology, based on fractional order controllers [50, 51]. The simulation results show that the proposed fractional order control strategy improves the performance of disturbance attenuation and system robustness.

A fractional order proportional integral derivative (FO-PID) controller is investigated for a three-level inverter called multi-neutral point (MNP) [52]. This paper claims that the FO-PID controller has a good dynamic response along with an excellent start-up response. The experimental results validate the performance and robustness of the FO-PID controller.

Another study deals with the study and implementation of a multi-level inverter simultaneously controlled by Modulated Hysteresis Current Control (MHCC) and Fractional Order PID (FO-PID) controllers [53]. The operation described in this work effectively produces a suitable waveform for the grid voltage.

1.5 Objectives of This Dissertation Research

The theme in this dissertation is to demonstrate the advantages of fractional order operators in the control loops and peak power point tracking of a grid-connected PV system with both theoretical analysis and simulation studies.

In summery, the two main objectives of this dissertation are:

- To improve the MPPT algorithm in a three-phase grid-connected PV system using fractional operators, and
- To improve the performance of a three-phase grid-connected PV system using fractional order controllers.

Two types of fractional order controllers, FO-PI and FO-[PI], is applied to a three-phase grid-connected PV system model and their performances is compared with a traditional integer order PI controller.

In addition, the fractional order extremum seeking control is proposed and its capability to track the peak power point is compared with the integer order extremum seeking control. Furthermore, the stability of fractional order extremum seeking control is investigated analytically.

Moreover, using Bode's Ideal cut-off filter, the BICO extremum seeking control is proposed and its performance will be compared to the integer order extremum seeking control. The stability and robustness of this novel MPPT algorithm are studied.

1.6 Dissertation Organization

This dissertation consists of six chapters, with the first chapter introducing the importance of solar energy. This topic followed by reviewing different type of grid-connected PV system topologies and grid-connected system standards. The literature review and objective of this dissertation are presented in this chapter.

Chapter 2 presents the mathematical definition of fractional order operators and fractional order systems. The time response and frequency response analysis of this class of systems has been introduced. Some useful properties of fractional order operators and controllers, which will be used in the further analysis, are breifly reviewed. Moreover, an analytical approach for tuning integer order PID and PI as the most popular controllers in power electronic systems is derived. Furthermore, a tuning method for fractional order PI and fractional order [PI] is proposed.

In Chapter 3, the mathematical modeling of a three-phase grid-connected PV system as the benchmark for this research will be derived. This topic is followed by introduction of some fundamental transformations which are used in analysis of three-phase grid-connected system. The advantages and disadvantages of different drive algorithms for a three-phase system are identified and eventually a general mathematical model, which is acceptable as a case study is introduced.

Chapter 4 presents the importance of maximum power point trackers in the PV systems and then identifies the reasons for choosing extremum seeking control as the maximum power point algorithm in this dissertation. The structure of extremum seeking control is presented in this chapter and then by introducing Bode's ideal cut-off filter, this filter is applied to the extremum seeking structure and the advantages of new scheme are analyzed. This topic is followed by introducing fractional order extremum seeking control and its stability analysis.

In Chapter 5, the PI, FO-PI, and FO-[PI] controllers are tuned for the mathematical model of current control loop and voltage control loop of the designed grid-connected PV system, using the proposed tuning methods. Using PLECS/MATLAB, the performance of these three controllers is compared and advantages of fractional order controllers are presented.

Chapter 6 presents the summary of the dissertation and conclusion of this research work as well as the future works.

Chapter 2

Fractional Order Calculus

2.1 Fractional Order Derivative and Integral

In recent years, the fractional order paradigm has been applied to many different engineering disciplines, including signal processing, control engineering, and many other fields such as biology and neuroscience. Fractional operators are the generalization of integration and differentiation of integer order calculus that allow us to present more accurate descriptions of real systems which includes a combination of multi-disciplinary field of engineering.

What makes the fractional order system interesting is the fact that all the real dynamic systems have certain degree of fractionality. But in many cases, this fractionality is not strong enough to affect the behavior of the system, and therefore this behavior can be described by an approximated integer order differential equation [54].

There are some special functions which play an important role in the fractional order calculus. In the following section these functions will be introduced.

2.1.1 Gamma Function

The Gamma function is one of the most essential building blocks of fractional order calculus. This function is defined as

$$\Gamma(n) = \int_0^\infty t^{n-1} e^{-t} dt. \tag{2.1}$$

This function is the general form of factorial function $n! = n \times (n-1) \times ... \times 1$ when $n \in \mathbb{R}$.

2.1.2 Mittag-Leffler Function

Another function which plays an essential role in fractional order calculus is the Mittag-Leffler function. This function has the similar fundamental role of the exponential function in integer order calculus.

$$E_{\alpha,\beta} = \sum_{k=0}^{\infty} \frac{z^k}{\Gamma(\alpha k + \beta)} \quad \mathbb{R}(\alpha) > 0, \mathbb{R}(\beta) > 0 \tag{2.2}$$

When $\beta = 1$, one parameter Mittag-Leffler function is obtained.

$$E_{\alpha,1} = E_{\alpha} = \sum_{k=0}^{\infty} \frac{z^k}{\Gamma(\alpha k + 1)} \quad \mathbb{R}(\alpha) > 0 \tag{2.3}$$

In the following, some special cases of the Mittag-Leffler function are introduced [55].

$$\begin{aligned} &E_{1,1}(z) = e^z \\ &E_{0,1}(z) = \tfrac{1}{1-z} \\ &E_{2,1}(z) = \cosh(\sqrt{z}) \\ &E_{2,1}(-z^2) = \cos(z) \\ &E_{0.5,1}(z) = e^{z^2} erfc(-z) \end{aligned} \tag{2.4}$$

Figure 2.1 presents the difference between the Mittag-Leffler function and an exponential function in the range of $[-1, 1]$.

2.2 Fractional Order Integral and Derivative

2.2.1 Grunwald-Letnikov Fractional Order Integral and Derivative

For any real continuous function, $f(t)$, the αth order Grunwald-Letnikov derivative is [56]

$${}_aD_t^{\alpha} f(t) = \lim_{h \to 0} h^{-\alpha} \sum_{j=0}^{\left[\frac{t-a}{h}\right]} (-1)^j \begin{pmatrix} \alpha \\ j \end{pmatrix} f(t - jh), \tag{2.5}$$

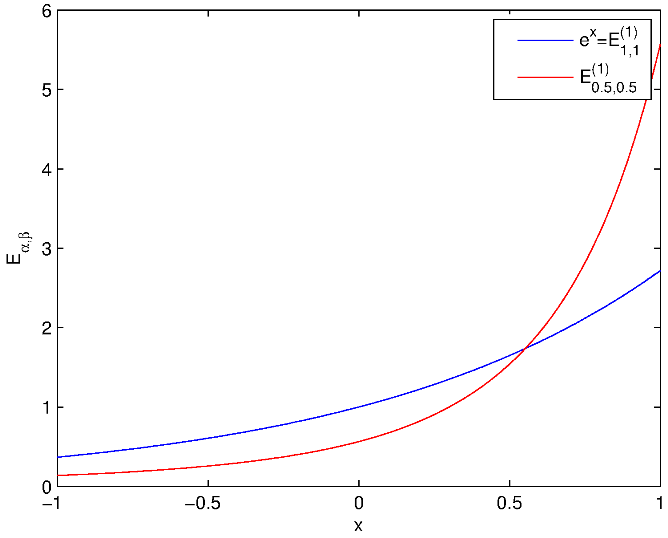

Fig. 2.1: Mittag-Leffler function vs. exponential function.

where $[x]$ means the integer part of x, a and t are the upper and lower limits of the derivative, and

$$\begin{pmatrix} \alpha \\ j \end{pmatrix} = \frac{\alpha!}{j!(\alpha-j)!} = \frac{\Gamma(\alpha+1)}{\Gamma(j+1)\Gamma(\alpha-j+1)}. \tag{2.6}$$

An alternative definition of the Grunwald-Letnikov derivative is

$$_aD_t^\alpha f(t) = \sum_{k=0}^{n} \frac{f^{(k)}(0^+)t^{k-\alpha}}{\Gamma(n+1-\alpha)} + \frac{1}{\Gamma(n+1-\alpha)} \int_0^t \frac{f^{(n+1)}(\tau)}{(t-\tau)^{\alpha-n}} d\tau \quad n \leq \alpha < n+1. \tag{2.7}$$

2.2.2 Reimann-Liouville Fractional Order Integral and Derivative

The Reimann-Liouville integral of order α for function $f(t)$ and for $\alpha \in \mathbb{R}^+$ is expressed by [57]

$$_aI_t^\alpha f(t) =_a D_t^{-\alpha} f(t) = \frac{1}{\Gamma(-\alpha)} \int_a^t \frac{f(\tau)}{(t-\tau)^{\alpha+1}} d\tau. \tag{2.8}$$

The Reimann-Liouville derivative of order α for $f(t)$ is expressed by

$$
{}_aD_t^{\alpha} f(t) = \frac{1}{\Gamma(n-\alpha)} \frac{d^n}{dt^n} \int_{\alpha}^{t} \frac{f(\tau)}{(t-\tau)^{\alpha-n+1}} d\tau, \tag{2.9}
$$

where $n - 1 \leq \alpha < n$ and $n \in \mathbb{N}$. In the special case where $f(t)$ is causal and $0 < \alpha < 1$, the fractional order integral (2.8) can be rewritten as

$$
{}_0D_t^{-\alpha} f(t) = \frac{1}{\Gamma(\alpha)} \int_{0}^{t} \frac{f(\tau)}{(t-\tau)^{1-\alpha}} d\tau, \tag{2.10}
$$

and in this case the fractional order derivative can be rewritten as

$$
{}_0D_t^{\alpha} f(t) = \frac{1}{\Gamma(n-\alpha)} \frac{d}{dt} \int_{\alpha}^{t} \frac{f(\tau)}{(t-\tau)^{\alpha}} d\tau. \tag{2.11}
$$

2.2.3 Caputo Fractional Order Derivative

The Caputo derivative is obtained by reformatting the Reimann-Liouville definition. The advantage of using the Caputo definition is that the initial conditions of the fractional order differential equations are in the same form as the initial conditions of integer order differential equations [57]

$$
{}_aD_t^{\alpha} f(t) = \frac{1}{\Gamma(n-\alpha)} \int_{\alpha}^{t} \frac{f^{(n)}(\tau)}{(t-\tau)^{\alpha-n+1}} d\tau, \tag{2.12}
$$

where $n - 1 \leq \alpha < n$. If the initial conditions for Reimann-Liouville and Caputo are homogenous, these two definitions are equivalent. In general, the relationship between these two definitions is

$$
{}_a^{RL}D_t^{\alpha} f(t) ={}_a^{C} D_t^{\alpha} f(t) + \sum_{k=0}^{n-1} \frac{(t-a)^{k-\alpha}}{\Gamma(k-\alpha+1)} f^{(k)}(a), \tag{2.13}
$$

where ${}^{RL}D$ and ${}^{C}D$ are Reimann-Leiouville and Caputo derivatives, respectively.

2.3 Laplace Transform of Fractional Order Operators

Similar to integer order calculus, Laplace transform is an important tool to solve the fractional order differential equations. The Laplace transform of $f(t)$ is defined by

$$F(s) = \int_0^\infty e^{-st} f(t)dt. \tag{2.14}$$

The Laplace transform of a function, $f(t)$, exists if, when $t \to \infty$, the function does not grow faster than an exponential function. In the mathematical form

$$\exists M, T; \quad e^{\alpha t} \parallel f(t) \parallel \leqslant M \quad \forall t > T. \tag{2.15}$$

The Laplace transform of an integer order derivative is expressed as

$$\mathcal{L}\{f^{(n)}(t)\} = s^n F(s) - \sum_{k=0}^{n-1} s^{n-k-1} f^{(k)}(0) = s^n F(s) - \sum_{k=0}^{n-1} s^k f^{(n-k-1)}(0). \tag{2.16}$$

The Laplace transform of fractional order Riemann-Liouville derivative is

$$\mathcal{L}\{{}_0D_t^\alpha f(t)\} = s^\alpha F(s) - \sum_{k=0}^{n-1} s^k_0 D_t^{\alpha-k-1} f(t)\Big|_{t=0} \quad n-1 \leq \alpha < n. \tag{2.17}$$

The Laplace transformation of Caputo derivative is

$$\mathcal{L}\{{}_0D_t^\alpha f(t)\} = s^\alpha F(s) - \sum_{k=0}^{n-1} s^{\alpha-k-1} f^{(n)}(t)\Big|_{t=0} \quad n-1 \leq \alpha < n. \tag{2.18}$$

Under zero initial condition, the Laplace transform of fractional order derivatives of Grunwald-Letnikov, Riemann-Liouville, and Caputo are equal to

$$\mathcal{L}\{{}_0D_t^\alpha f(t)\} = s^\alpha F(s). \tag{2.19}$$

An explanatory table of fractional order Laplace transformation has been presented in Oberhrttinger and Baddi [58].

Some of the important properties of fractional derivatives and integral are expressed in this section.

Property 1:

According to Fig. 2.2, from the geometrical point of view, fractional order integral of $f(t)$ for fixed t is the shadow of this function on (g, f) wall, where, g scales f with the following equation [59]

$$g_t(\tau) = \frac{1}{\Gamma(\alpha+1)}\{t^{\alpha} - (t-\tau)^{\alpha}\}. \tag{2.20}$$

Property 2:

According to the "short memory principal" of fractional order derivatives [47], if $t > a + L$,

$$_aD_t^{\alpha} f(t) \simeq {}_{t-L} D_t^{\alpha} f(t), \tag{2.21}$$

where L is the memory length. This principle means the fractional order derivative depends on mainly the "recent past" values of $f(t)$. The associated estimated error has the following upper bound

$$|_aD_t^{\alpha} f(t) - {}_{t-L} D_t^{\alpha} f(t)| \leq \frac{ML^{-\alpha}}{\Gamma(1-\alpha)} \quad \forall a + L \leq t \leq T, \tag{2.22}$$

where M is the upper bound of $f(t)$ in the interval of $[a, T]$.

Property 3:

If $f(t)$ is an analytical function of t, then $_0D_t^{\alpha} f(t)$ is an analytical function of t and α [56].

Property 4:

Fractional order derivatives and integrals are the general form of integer order derivatives and integrals. Therefore, if the order of fractional order operators becomes integer, the result will be the same as integer order operators. In the special case, zero'th order fractional order derivative and integral result in the original function [56].

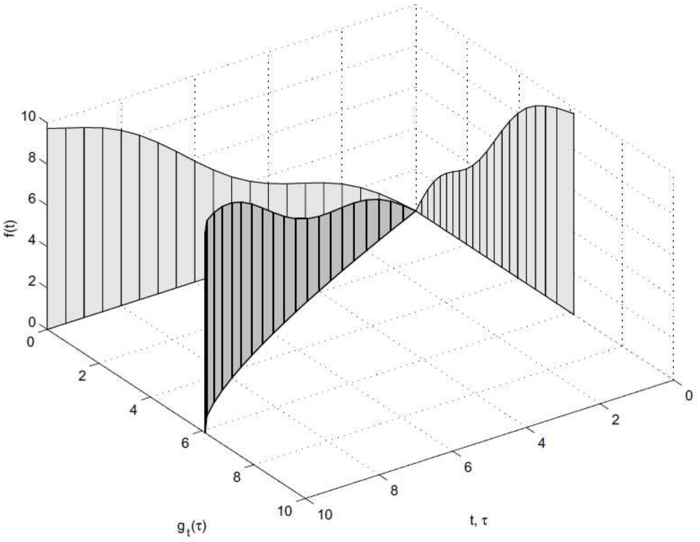

Fig. 2.2: Geometrical interpretation of fractional order integral.

Property 5:

Fractional order integral and derivative are linear operators, meaning for all constants a and b [47]

$$ {}_0D_t^\alpha(af(t)+bg(t)) = a{}_0D_t^\alpha f(t) + b{}_0D_t^\alpha g(t). \tag{2.23}$$

Property 6:

The integer order and fractional order derivatives of $f(t)$ are interchangeable in the Caputo definition [60]

$$\forall m \in \mathbb{Z}^+; \quad {}_a^C D_t^\alpha \left({}_a^C D_t^m f(t) \right) = {}_a^C D_t^m \left({}_a^C D_t^\alpha \right) = {}_a^C D_t^{\alpha+m} f(t), \tag{2.24}$$

if $n-1 \leq \alpha < n \in \mathbb{N}$, then $\forall n < k < m$; $f^{(k)}(0) = 0$. In the Riemann-Liouville case, (2.24) holds if $\forall k < m; f^{(k)}(0) = 0$.

For the mixed integral and derivative operators in the case of Riemann-Liouville,

$$ {}_aD_t^{\alpha}\Big({}_aI_t^{\beta}f(t)\Big) = \begin{cases} {}_aD_t^{\alpha-\beta}f(t), & \alpha > \beta, \\ {}_aI_t^{\beta-\alpha}f(t), & \alpha \le \beta. \end{cases} \tag{2.25} $$

Property 7:

In the fractional order integral case,

$$ {}_aI_t^{\alpha}\Big({}_aI_t^{\beta}f(t)\Big) = {}_aI_t^{\beta}\Big({}_aI_t^{\alpha}f(t)\Big) = {}_aI_t^{\alpha+\beta}f(t). \tag{2.26} $$

But, generally, in the fractional order derivative,

$$ {}_aD_t^{\alpha}\Big({}_aD_t^{\beta}f(t)\Big) \neq {}_aD_t^{\beta}\Big({}_aD_t^{\alpha}f(t)\Big) \neq {}_aD_t^{\alpha+\beta}f(t). \tag{2.27} $$

In the case of the Riemann-Liouville derivative, if $\alpha = \beta$ or $\forall k < \max(n,m) - 1; f^{(k)}(0) = 0$, where $n-1 \le \alpha < n$ and $m-1 \le \beta < m$, then,

$$ {}_aD_t^{\alpha}\Big({}_aD_t^{\beta}f(t)\Big) = {}_aD_t^{\beta}\Big({}_aD_t^{\alpha}f(t)\Big) = {}_aD_t^{\alpha+\beta}f(t). \tag{2.28} $$

In the case of the Caputo derivative, if $m = n$ and $f^{(n)}(0) = f^{(m)}(0) = 0$, then (2.28) holds [60].

Property 8:

If $f(t)$ and $g(t)$ and all their derivatives are continuous in $[a,t]$, the Leibniz's rule for fractional order derivatives is

$$ {}_aD_t^{\alpha}\big(f(t)g(t)\big) = \sum_{k=0}^{\infty} \begin{pmatrix} r \\ k \end{pmatrix} f^{(k)}(t)\,{}_aD_t^{\alpha-k}g(t). \tag{2.29} $$

Property 9:

The Caputo and Riemann-Liouville derivatives of a constant result differently. The Caputo derivative of a constant is zero, ${}_a^CD_t^{\alpha}K = 0$, where K is a constant. However, the Riemann-Liouville derivative of a constant is

$$ {}_aD_t^\alpha K = \frac{K(t-a)^\alpha}{\Gamma(1-\alpha)}, \tag{2.30}$$

and if $a \to -\infty$ then, ${}_aD_t^\alpha K = 0$.

2.4 Linear Fractional Order Dynamic Systems

All the phenomena have some degree of fractionality, which sometimes is dominant and sometimes is negligible. Therefore, in some cases, an integer order differential equation (IODE) is the closest and the best approximated model to a system with fractional order dynamics. A general fractional order differential equation is expressed by

$$\begin{aligned} &{}_{a_n}D^{\alpha_n}y(t) +_{a_{n-1}} D^{\alpha_{n-1}}y(t) + \dots +_{a_0} D^{\alpha_0}y(t) \\ &= b_m D^{\beta_m}u(t) +_{b_{m-1}} D^{\beta_{m-1}}u(t) + \dots +_{b_0} D^{\beta_0}u(t), \end{aligned} \tag{2.31}$$

where a_k and b_k are constants ($k \in \mathbb{Z}^+$), $y(t)$ and $u(t)$ are output and input of the system respectively, and α_k and β_k are arbitrary real or rational numbers, and D^α and D^β can be the Grunwald-Letnikov, Riemann-Liouville, or Caputo derivatives. Using Laplace transformation, the corresponding transfer function is

$$G(s) = \frac{b_m s^{\beta_m} + b_{m-1}s^{\beta_{m-1}} + \dots + b_0 s^{\beta_0}}{a_n s^{\alpha_n} + a_{n-1}s^{\alpha_{n-1}} + \dots + a_0 s^{\alpha_0}}. \tag{2.32}$$

In the particular case of commensurate order system, where $\forall k \in \mathbb{Z}^+; \alpha_k = k\alpha$, $\beta_k = k\alpha$ and $0 < \alpha < 1$, the transfer function is described by

$$G(s) = \frac{\sum_{k=0}^m b_k s^{\alpha k}}{\sum_{k=0}^n a_k s^{\alpha k}}, \tag{2.33}$$

which can be considered as a pseudo-rational function of $\lambda = s^\alpha$,

$$G(\lambda) = \frac{\sum_{k=0}^m b_k \lambda^k}{\sum_{k=0}^n a_k \lambda^k}. \tag{2.34}$$

In this case, the transfer function can be expanded to the following form

$$G(s) = K_0\Big[\sum_{k=1}^{n} \frac{A_k}{s^{\alpha} + p_k}\Big], \tag{2.35}$$

where p_k's are the transfer function poles (which are assumed to be simple). Therefore, the analytical solution of the fractional order differential equation in this specific case is [58]

$$y(t) = K_0 \sum_{k=1}^{n} A_k t^{\alpha} E_{\alpha,\alpha}(-p_k t^{\alpha}), \tag{2.36}$$

where $E_{\alpha,\alpha}(.)$ is the Mittag-Leffler function.

2.5 Stability of Linear Fractional Order System

A general way to study the stability of a system is to consider the solution(s) of its differential equation(s). An alternative way in the case of integer order LTI system is to study the root locations of its characteristic polynomial. In the case of fractional order LTI systems, (2.32), the characteristic polynomial of the system is

$$a_n s^{\alpha_n} + a_{n-1} s^{\alpha_{n-1}} + ... + a_0 s^{\alpha_0}, \tag{2.37}$$

which is a multi-valued function of complex variable s. (2.37) has an infinite number of roots, but only a finite number of these roots are placed on the principal sheet of the Riemann surface. Among all of these roots, those which are in the secondary sheets of the Riemann surface are related to solutions that go to zero when $t \to \infty$ without oscillation. The roots which are placed in the principal sheet of the Riemann surface are responsible for the transient response dynamics [47].

2.5.1 Stability of LTI Fractional Order System

LTI irrational fractional order transfer function with $G(s) = \frac{Z(s)}{P(s)}$, is bounded input-bounded output (BIBO) stable if and only if [56]

$$\mathbb{R}(s) \geq 0, \exists M; |G(s)| \leq M \quad \forall s. \tag{2.38}$$

This condition is satisfied if

- All the roots of characteristic polynomial of $G(s)$ which is located on principal Riemann sheet have negative real parts, and
- All the roots of characteristic polynomial of $G(s)$ which is located on principal Riemann sheet do not satisfy $Z(s) = 0$.

In the case of commensurate order system (2.33), the stability condition is described by [56]

$$|arg(p_k)| > \alpha\frac{\pi}{2} \quad \forall p_k, \tag{2.39}$$

where p_k's are the roots of the characteristic polynomial of pseudo-rational function of (2.33). The stability region of this type of systems is depicted in Fig. 2.3.

In the special case of integer order transfer function where $\alpha = 1$, the stability condition of (2.39), turns out to be

$$|arg(p_k)| > \frac{\pi}{2}, \tag{2.40}$$

which means to satisfy the stability condition, the argument of all the poles of integer order transfer function need to be greater than $\frac{\pi}{2}$ or in other words, these poles should be located on the left side of $j\omega$ axis on complex plane.

2.5.2 Time Domain Analysis of LTI Fractional Order System

The transient response of an LTI fractional order system can be described according to Table 2.1 [47]. In this table, PSRS stands for Principal Sheet of the Riemann Surface.

According to the discussion in the previous sections, in the case of commensurate order system, where its step response is

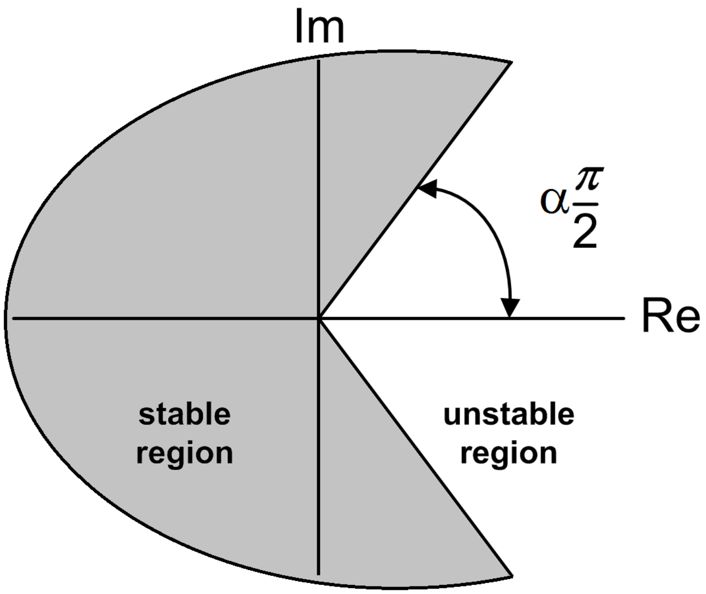

Fig. 2.3: Stability region of commensurate order systems.

Table 2.1: Transient response of LTI fractional order systems.

Place of the roots	Response
No roots on PSRS	Monotonically decreasing
Real negative roots on PSRS	Monotonically decreasing
Roots with negative real part on PSRS	Damped oscillation
Imaginary roots on PSRS	Oscillation with constant amplitude
Roots with positive real part on PSRS	Oscillation with increasing amplitude
Real positive roots on PSRS	Monotonically increasing

$$y(t) = \sum_{k=0}^{n} A_k t^{\alpha} E_{\alpha,\alpha+1}(p_k t^{\alpha}), \tag{2.41}$$

the transient responses for different α's are depicted in Fig. 2.4 [47].

2.6 Fractional Order Nonlinear Systems

A fractional order non-commensurate nonlinear system is described by [56]

$$\begin{cases} {}_0D_t^{\alpha_k}\bar{x}(t) = f_k(\bar{x}(t), t) \\ \bar{x}_k(0) = c_k, \quad k = 1, 2, ..., n, \end{cases} \tag{2.42}$$

where $\bar{x}(t) = [x_1, x_2, ..., x_k]$, and c_k's are initial conditions. The equilibrium points of (2.42) are the solution of $f_k(\bar{x}(t), t) = 0$.

Generally, stability analysis of nonlinear systems is more complex than LTI systems because some of the phenomena like limit-cycle do not exist in the linear systems and other than that there are different types of stability in the nonlinear systems. For instance, in these systems, asymptotically stable, globally stable, exponentially stable has been defined which are not applicable to the linear systems.

Asymptotical Stability of Fractional Order Nonlinear Systems:

If there is a positive real α so that

$$\forall \|x(t)\| \quad with \quad t \le t_0, \exists N(x(t)) \quad ; \quad \forall t \le t_0, \|x(t)\| \le N t^{-\alpha}, \tag{2.43}$$

trajectory $x(t) = 0$ of the system (2.42) is $t^{-\alpha}$ asymptotically stable [56]. The fact that the components of $x(t)$ slowly decay toward zero following t^{-q} envelope sometimes called long memory systems.

Theorem: According to the stability theorem for nonlinear fractional order systems [61], the equilibrium points of (2.42) are asymptotically stable for α if all the eigenvalues of the Jacobian matrix, $\bar{J} = \frac{\partial \bar{f}}{\partial \bar{x}}$, evaluated at the equilibrium E^*, satisfy the condition

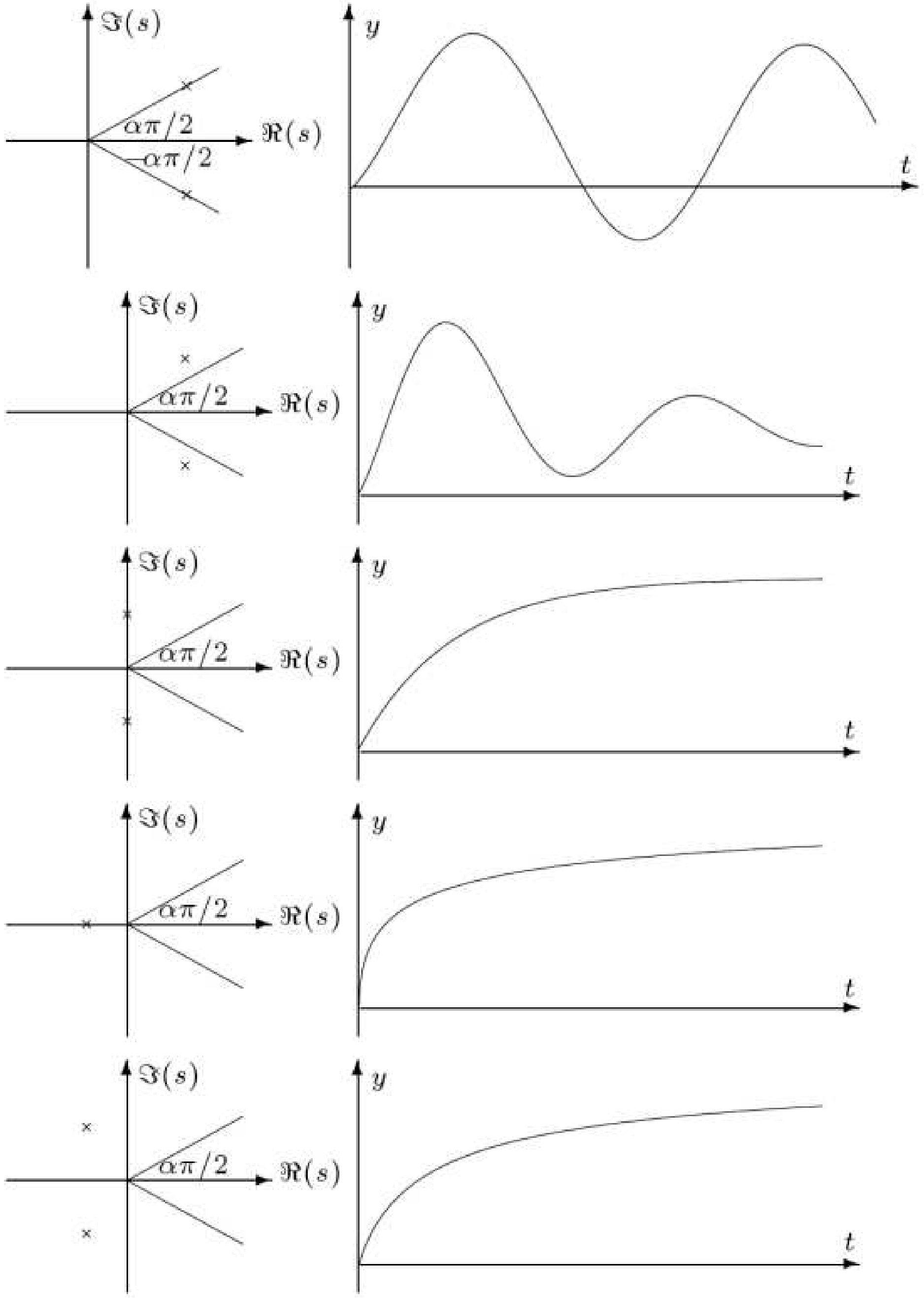

Fig. 2.4: Transient response of commensurate order systems with order α.

$$|arg(eig(\bar{J}))| > \alpha\frac{\pi}{2}. \tag{2.44}$$

2.7 Fractional Order PID Controllers

PID (proportional integral derivative) controller is one of the most popular and attractive controllers for engineers. This industrial popularity comes from the following reasons:

- PID controllers have a simple structure, which makes them easily implemented;
- The performance robustness in these type of controllers is acceptable in a wide range of applications; and
- There are many well established PID tuning methods.

For the same reasons, PID controller is attractive for researchers in the applied fractional calculus field and in the past decade there has been an increasing amount of researches on this topic.

The fractional order PID ($PI^{\alpha}D^{\beta}$) was proposed in 1999 as a generalized form of the PID controller by replacing the integer order integrator and derivative with fractional order integrator, I^{α}, and derivative, D^{β}. The transfer function of the proposed PID is [44]

$$C(s) = \frac{U(s)}{E(s)} = K_p + K_i s^{-\alpha} + K_d s^{\beta} \quad 0 < \alpha, \beta < 1, \tag{2.45}$$

where K_p, K_i, and K_d are proportional, integral, and derivative gains. It is expected that $PI^{\alpha}D^{\beta}$ would enhance the system control performance due to more tuning knobs which are introduced in this controller. As seen in Fig. 2.5, $PI^{\alpha}D^{\beta}$ covers an area in instead of limited number of points which shows a huge degree of freedom in the fractional order PID compared to integer order PID.

Some typical fractional order PID controllers are fractional order PI [47]

$$C(s) = K_p + \frac{K_i}{s^{\alpha}}, \tag{2.46}$$

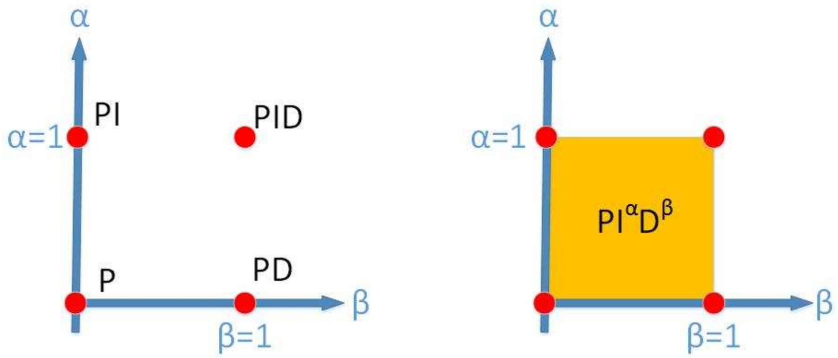

Fig. 2.5: Integer order PID family vs. fractional order PID family in $\alpha - \beta$ plane.

fractional order PD controller [62]

$$C(s) = K_p + K_d s^{\alpha}, \tag{2.47}$$

fractional order [PI] controller [62]

$$C(s) = \left(K_p + \frac{K_i}{s}\right)^{\lambda}. \tag{2.48}$$

As pointed in Chen, in the case of closed-loop control systems using PID controller, there are four situations [63]:

- IO (integer order) plant with IO controller,
- IO plant with FO (fractional order) controller,
- FO plant with IO controller, and
- FO plant with FO controller.

In practical applications, using the fractional order controllers are more common, because the plant model may have already been determined as an integer order form. Among all introduced fractional order controllers, fractional order PI and fractional order [PI] have been applied to industrial applications. In this work, these two types of controllers will be applied to a three-phase grid-connected PV system and the advantages of using these controllers in the grid-connected system will be explored. The implementation of fractional order derivative and integral has been discussed in different literature [64–66].

2.8 Controller Tuning Procedure for First Order Plus Delay System

In the integer order world, first order plus time delay model is widely used to model systems with S-shaped reaction curve. Its generalized form is the model with a single fractional pole replacing integer order pole, which is believed to better characterize the reaction curve.

The general from of a fractional order pole plus delay system is

$$P(s) = \frac{K}{Ts^{\alpha} + 1} e^{-Ls}, \quad \alpha \in (0, 1], \tag{2.49}$$

where $T, L,$ and K are constants. In this section, the goal is to define a process to tune integer order PID, fractional order PI, and fractional order [PI], for the fractional order plant of (2.49). The transfer function of the three controllers are given, respectively, as follows:

$$C_1(s) = K_p + \frac{K_i}{s} + K_d s, \tag{2.50}$$

$$C_2(s) = K_p\Big(1 + \frac{K_i}{s^{\lambda}}\Big), \tag{2.51}$$

$$C_3(s) = \Big(K_p + \frac{K_i}{s}\Big)^{\lambda}, \tag{2.52}$$

where K_p, K_i, K_d, and $\lambda \in (0, 1)$ are positive real number.

There are many different approaches for PID tuning. A tuning method for integer order PID and also fractional order PI and [PI] controllers for time delayed system with integer order pole was proposed in Luo et al. [67]. This tuning method has been extended for time delayed system with fractional order pole in Malek et al. [54]. In this method, it has been assumed that the gain crossover frequency, ω_c, and phase margin, ϕ_m, are given and design constraints for tuning the controller are presented as follows [67]:

- Phase margin constraint

$$Arg[G(j\omega_c)] = Arg[C(j\omega_c)P(j\omega_c)] = \angle C(j\omega_c) + \angle P(j\omega_c) = -\pi + \phi_M, \qquad (2.53)$$

  where $G(j\omega)$ is open-loop transfer function of the system, $C(j\omega)$ is the controller transfer function, and $P(j\omega)$ is the plant transfer function.

- Gain cross-over frequency constraint

$$\mid G(j\omega_c) \mid = \mid C(j\omega_c)P(j\omega_c) \mid_{dB} = \mid C(j\omega_c) \mid_{dB} \mid P(j\omega_c) \mid_{dB} = 0. \qquad (2.54)$$

- Constraint for robustness to loop gain variations

  This constraint demands that the phase is flat around the gain crossover frequency, ω_c. It means that the derivative of open-loop phase around the gain cross-over frequency is zero, i.e.,

$$\frac{d(Arg[G(j\omega)])}{d\omega} \mid_{\omega=\omega_c} = 0. \qquad (2.55)$$

2.9 Tuning of the Controllers

In this section, based on the constraints introduced previously, the tuning process of the PID controller (2.50), fractional PI controller (2.51), and fractional [PI] controller (2.52), for the considered plant with constant time delay and fractional order pole (2.49) will be presented.

2.9.1 Integer Order PID Controller Design

The open-loop transfer function of plant (2.49) and PID controller (2.50) is

$$G_1(s) = C_1(s)P(s) = \Big(K_p + \frac{Ki}{s} + K_d s\Big)\Big(\frac{K}{Ts^{\alpha}+1}e^{-Ls}\Big), \qquad (2.56)$$

where T, α and L are known and K_p, K_i, and K_d should be designed.

The phase of the open-loop system at the gain cross-over frequency is

$$Arg[G_1(j\omega_c)] = \tan^{-1}\Big(\frac{K_d\omega_c^2 - K_i}{\omega_c K_p}\Big) - \tan^{-1}\Big(\frac{B}{A}\Big) - L\omega_c, \tag{2.57}$$

where $A = 1 + T\omega_c^\alpha \cos(\alpha\pi/2)$ and $B = T\omega_c^\alpha \sin(\alpha\pi/2)$. According to the first design constraint (2.53), the phase of considered system with integer order PID controller at the gain cross-over frequency (ω_c) is

$$\tan^{-1}\Big(\frac{K_d\omega_c^2 - K_i}{\omega_c K_p}\Big) - \tan^{-1}\Big(\frac{B}{A}\Big) \mid_{\omega=\omega_c} -L\omega_c = -\pi + \phi_M, \tag{2.58}$$

so

$$\frac{K_d\omega_c^2 - K_i}{\omega_c K_p} = \tan\Big(\tan^{-1}\Big(\frac{B}{A}\Big) + \phi_M + L\omega_c - \pi\Big). \tag{2.59}$$

The open-loop gain at the gain cross-over frequency is

$$\mid G_1(j\omega_c) \mid = \frac{K\sqrt{K_p^2 + (K_d\omega_c - \frac{K_i}{\omega_c})^2}}{\sqrt{A^2+B^2}}. \tag{2.60}$$

According to the second design constraint (2.54),

$$\frac{\sqrt{K_p^2 + (K_d\omega_c - \frac{K_i}{\omega_c})^2}}{\sqrt{A^2+B^2}} = \frac{1}{K}. \tag{2.61}$$

Based on the third constraint (2.55), the robustness to the loop gain variations can be obtained by forcing the phase plot to be flat around the gain cross-over frequency which is achievable if derivative of phase with respect to frequency at the cross-over frequency is equal to zero. Then

$$\frac{\alpha T\omega_c^{\alpha-1}[A\sin(\frac{\alpha\pi}{2}) - B\cos(\frac{\alpha\pi}{2})]}{A^2+B^2} + L - \frac{K_p(K_d\omega_c^2 + K_i)}{(K_p\omega_c)^2 + (K_d\omega_c^2 - K_i)^2} = 0. \tag{2.62}$$

From (2.59), (2.61), and (2.62) the gain of PID controller (K_p, K_i and K_d) can be determined.

$$K_p = \sqrt{\frac{A^2+B^2}{K^2(1+D_1^2)}}, \tag{2.63}$$

where $D_1 = \tan\Big[\tan^{-1}\Big(\frac{B}{A}\Big) + L\omega_c + \phi_m - \pi\Big]$,

$$K_i = \frac{1}{2}\Big[E_1 K_p \omega_c^2 (1+D_1^2) - D_1 K_p \omega_c\Big], \tag{2.64}$$

where $E_1 = \frac{\alpha T \omega_c^{\alpha-1}}{A^2+B^2}\Big(A\sin(\alpha\pi/2) - B\cos(\alpha\pi/2)\Big) + L$, and

$$K_d = \frac{K_i + D_1 K_p \omega_c}{\omega_c}. \tag{2.65}$$

2.9.2 Fractional Order PI Controller Design

The open-loop transfer function of the controlled system with the fractional order PI (FO-PI) controller is

$$G_2(s) = C_2(s)P(s) = K_p\Big(1 + \frac{K_i}{s^\lambda}\Big)\Big(\frac{K}{Ts^\alpha + 1}e^{-Ls}\Big), \tag{2.66}$$

where T, α and L are known and K_p, K_i, and λ should be designed in the controller design process.

The FO-PI controller can be expressed as

$$C_2(s) = K_p\Big(1 + \frac{K_i}{s^\lambda}\Big) = K_p\Big(1 + \frac{K_i}{(j\omega)^\lambda}\Big) = K_p\Big(1 + \frac{K_i\omega^{-\lambda}}{j^\lambda}\Big). \tag{2.67}$$

Since $j = e^{\pi/2}$, then $j^\lambda = e^{\lambda\pi/2} = \cos(\lambda\pi/2) + j\sin(\lambda\pi/2)$, therefore,

$$C_2(s) = K_p\Big(1 + \frac{K_i\omega^{-\lambda}}{\cos(\lambda\pi/2) + j\sin(\lambda\pi/2)}\Big). \tag{2.68}$$

Then open-loop phase at the gain cross-over frequency is

$$Arg[G_2(j\omega_c)] = -\tan^{-1}\Big[\frac{K_i\omega_c^{-\lambda}\sin(\frac{\lambda\pi}{2})}{1 + K_i\omega_c^{-\lambda}\cos(\frac{\lambda\pi}{2})}\Big] - \tan^{-1}\Big(\frac{B}{A}\Big) - L\omega_c, \tag{2.69}$$

where $A = 1 + T\omega_c^\alpha \cos(\alpha\pi/2)$ and $B = T\omega_c^\alpha \sin(\alpha\pi/2)$.

Based on the first design constraint (2.53),

$$\tan^{-1}\Big[\frac{K_i\omega_c^{-\lambda}\sin(\frac{\lambda\pi}{2})}{1+K_i\omega_c^{-\lambda}\cos(\frac{\lambda\pi}{2})}\Big] - \tan^{-1}\Big(\frac{B}{A}\Big) - L\omega_c = -\pi + \phi_M, \tag{2.70}$$

or

$$\frac{K_i\omega_c^{-\lambda}\sin(\frac{\lambda\pi}{2})}{1+K_i\omega_c^{-\lambda}\cos(\frac{\lambda\pi}{2})} = \tan\Big(\tan^{-1}\Big(\frac{B}{A}\Big) + L\omega_c + \phi_M\Big). \tag{2.71}$$

Then, relationship between K_i and λ can be established as

$$K_i = \frac{-D_2}{\omega_c^{-\lambda}\sin(\frac{\lambda\pi}{2}) + \omega_c^{-\lambda}\cos(\frac{\lambda\pi}{2})}, \tag{2.72}$$

where $D_2 = \tan\big[\tan^{-1}(B/A) + \phi_M + L\big]$.

Open-loop gain using FO-PI controller at the cross-over frequency is

$$\mid G_2(j\omega_c) \mid = \frac{K.K_p\sqrt{(1+K_i\omega_c^{-\lambda}\cos(\frac{\lambda\pi}{2}))^2 + (K_i\omega_c^{-\lambda}\sin(\frac{\lambda\pi}{2}))^2}}{\sqrt{A^2+B^2}}. \tag{2.73}$$

According to the second constraint (2.54),

$$\frac{K.K_p\sqrt{(1+K_i\omega^{-\lambda}\cos(\frac{\lambda\pi}{2}))^2 + (K_i\omega^{-\lambda}\sin(\frac{\lambda\pi}{2}))^2}}{\sqrt{A^2+B^2}} = 1, \tag{2.74}$$

or

$$K_p = \sqrt{\frac{A^2+B^2}{K^2(1+K_i\omega_c^{-\lambda}\cos(\frac{\lambda\pi}{2}))^2 + (K_i\omega_c^{-\lambda}\sin(\frac{\lambda\pi}{2}))^2}}. \tag{2.75}$$

According to the third constraint (2.55),

$$\frac{K_i\omega^{\lambda-1}\sin(\frac{\lambda\pi}{2})}{\omega^{2\lambda} + 2K_i\omega^{\lambda}\cos(\frac{\lambda\pi}{2}) + K_i^2} \mid_{\omega=\omega_c} - E_2 = 0, \tag{2.76}$$

where $E_2 = \frac{\alpha T\omega_c^{\alpha-1}}{A^2+B^2}\Big(A\sin(\alpha\pi/2) - B\cos(\alpha\pi/2)\Big) + L$.

Then, an equation for K_i versus λ can be established as follows:

$$K_i = \frac{-F_2 \pm \sqrt{F_2^2 - 4E_2^2\omega_c^{-2\lambda}}}{2E_2\omega_c^{-2\lambda}}, \tag{2.77}$$

where $F_2 = 2E_2\omega_c^{-\lambda}\cos(\lambda\pi/2) - \lambda\omega_c^{-\lambda-1}\sin(\lambda\pi/2)$.

Obviously, based on (2.72), (2.75), and (2.76), λ, K_i, and K_p can be determined by different approaches like $fminsearch$ function in MATLAB or by the graphical method. In the graphical method, (2.72) and (2.76) are plotted on the same axes, and from the intersection point, K_i and λ are obtained and then K_p is determined by (2.75).

2.9.3 Fractional Order [PI] Controller Design

The open-loop transfer function of controlled system with the fractional order [PI] controller is

$$G_3(j\omega) = C_3(s)P(S) = \Big(K_p + \frac{K_i}{s}\Big)^{\lambda}\Big(\frac{K}{Ts^{\alpha}+1}e^{-Ls}\Big). \tag{2.78}$$

Open-loop phase at the gain cross-over frequency is

$$Arg[G_3(j\omega_c)] = -\lambda\tan^{-1}\Big(\frac{K_i}{K_p\omega_c}\Big) - \tan^{-1}\Big(\frac{B}{A}\Big) - L\omega_c. \tag{2.79}$$

According to the design rules, the open-loop phase satisfies the following relationship:

$$-\lambda\tan^{-1}\Big(\frac{K_i}{K_p\omega_c}\Big) - \tan^{-1}\Big(\frac{B}{A}\Big)\,|_{\omega=\omega_c} - L\omega_c = -\pi + \phi_M, \tag{2.80}$$

so,

$$\frac{K_i}{K_p\omega_c} = D_3, \tag{2.81}$$

where $D_3 = \tan[(\pi - \phi_m - \tan^{-1}(B(\omega_c)/A(\omega_c)) - L\omega_c)/\lambda]$.

Open-loop gain at the gain cross-over frequency should satisfy the second constraint (2.54),

$$\frac{K[K_p^2 + (\frac{K_i}{\omega_c})^2]^{\frac{\lambda}{2}}}{\sqrt{A^2+B^2}} = 1. \tag{2.82}$$

Based on the third constraint (2.55), for the robustness to loop gain variations

$$\frac{\lambda K_i K_p}{(K_p\omega_c)^2 + K_i^2} = E_3, \tag{2.83}$$

where $E_3 = \frac{\alpha T \omega_c^{\alpha-1}}{A^2+B^2}\Big(A\sin(\frac{\alpha\pi}{2}) - B\cos(\frac{\alpha\pi}{2})\Big) + L.$

From (2.80), (2.82), and (2.83),

$$K_i = \sqrt{\frac{E_3}{\lambda}\omega^3 D_3 (A^2(\omega_c) + B^2(\omega_c))^{\frac{1}{\lambda}}}, \tag{2.84}$$

$$K_i = \omega_c\sqrt{(A^2(\omega_c) + B^2(\omega_c))^{\frac{1}{\lambda}}[1 - \frac{E_3\omega_c}{\lambda D_3}]}, \tag{2.85}$$

and

$$K_p = \sqrt{\frac{E_3\omega_c(A^2(\omega_c) + B^2(\omega_c))^{\frac{1}{\lambda}}}{\lambda D_3}}. \tag{2.86}$$

K_i and λ can be found graphically from (2.84) and (2.85), and then K_p is calculated by (2.86) or alternatively, *fminsearch* command of MATLAB can be used to find K_p, K_i, and λ of FO[PI] controller.

2.9.4 PI Controller Design

In the special case of integer order PI and first order plant with delay, the PI gains are obtained by

$$K_p = \sqrt{\frac{1 + T^2\omega_c^2}{K^2(1 + D_1^2)}}, \tag{2.87}$$

and

$$K_i = \frac{1}{2}\Big[E_1 K_p \omega_c^2 (1 + D_1^2) - D_1 K_p \omega_c\Big]. \tag{2.88}$$

2.10 Summary

In this chapter, some basic definitions plus a general overview of fractional order calculus have been presented. As mentioned, fractional order systems behave differently from integer order systems, therefore, some critical features like stability definition in linear and nonlinear fractional order systems have been reviewed. Lastly, a class of PID controllers, fractional order PI, have been introduced and the tuning approach for these controllers plus integer order PID and PI has been discussed.

Chapter 3

Three-Phase Grid-Connected Inverters

3.1 Mathematical Model of Three-Phase Grid Connected VSI

Analytical models are essential tools to be used in the dynamic performance, robustness, and stability analysis of different control strategies. To investigate these features on a three-phase grid-connected PV system controlled by fractional order controllers, the mathematical model of the system needs to be derived. The system to be modeled is depicted in Fig. 3.1. As shown in this figure, this system has five following building blocks:

- PV array,
- DC-AC inverter,
- Three-phase decoupling transformations,
- Synchronization, and
- Inverter driver.

In this section, the operation and role of each of these blocks will be described and its mathematical model will be derived.

3.1.1 Photovoltaic Cell and Array Modeling

Typically, a PV cell is a simple P-N junction diode which converts solar irradiation into electricity [68]. Figure 3.2 illustrates a simple equivalent circuit diagram of a PV cell [19]. This model consists of a current source which represents the generated current from PV cell, a diode in parallel with the current source, a shunt resistance, and a series resistance [69]. In this model, the diode current is

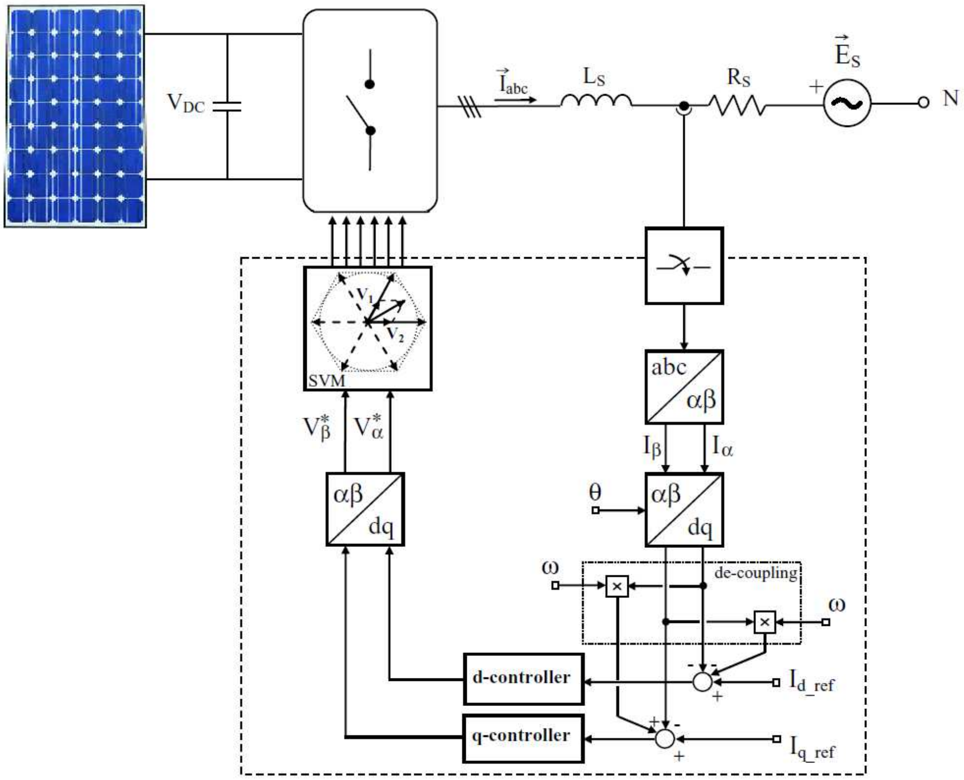

Fig. 3.1: Three-phase synchronous frame current controller scheme.

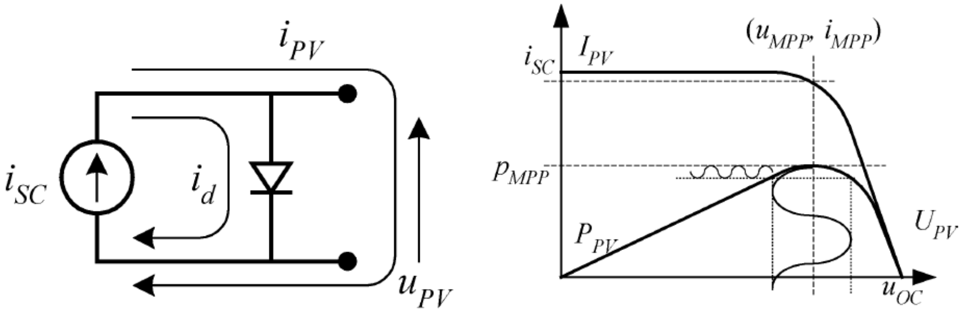

Fig. 3.2: Equivalent circuit of a PV cell and its characteristics.

$$I_D = I_s\big[e^{\alpha(\nu_{pv}+R_s i_{pv})} - 1\big], \tag{3.1}$$

where $\alpha = \frac{q}{AkT_C}$, I_s is saturation current, υ_{pv} and i_{pv} are the voltage and current of the PV cell output. Other constants and their definitions are shown in Table 3.1 [69].

The output current, generated by the PV cell, can be calculated by applying Kirchhoff's law (KCL),

$$i_{pv} = I_L - I_s\big[e^{\alpha(\upsilon_{pv}+R_s i_{pv})} - 1\big] - \frac{\upsilon pv + R_s i_{pv}}{R_{sh}}. \tag{3.2}$$

In (3.2), the current source output, I_L, is related to the solar irradiation and temperature by

$$i_L = \frac{G}{1000}\big[I_{sc} + k_i(T_C - T_{ref})\big], \tag{3.3}$$

where G is the solar irradiation, I_{sc} is the short circuit current, k_i is the short circuit current coefficient, T_C is the cell's operating temperature (in K), and T_{ref} is the reference temperature of the cell. The cell's saturation current, I_s, in (3.2) is related to the operating and reference temperatures as follows:

$$I_s = I_{RS}\Big(\frac{T_C}{T_{ref}}\Big)^3 e^{\frac{qE_g}{Ak}\left(\frac{1}{T_{ref}} - \frac{1}{TC}\right)}, \tag{3.4}$$

where I_{RS} is reverse saturation current in the reference temperature and solar irradiation, and E_g is the bandgap energy of the PV semiconductor [68].

Table 3.1: Parameter values of the considered PV model.

T_C	$298C$	Operation Temperature
I_{sc}	$3.2A$	Short Circuit Current
A	$1-5$	Ideality Factor
k	1.3807×10^{-23}	Boltzman's Constant
q	$1.6022 \times 10^{-19}C$	Electron Charge
R	0.01Ω	Resistance

Since the output voltage and current of one PV cell are very low, a combination of series and parallel cells are connected together in order to deliver higher current and voltage. These cells are encapsulated with a transparent material to protect them from harsh environmental conditions and form a PV module. In order to obtain a higher voltage and current for higher power applications, a number of PV modules need to be connected to form a PV array. If a PV array contains N_s series PV cells and N_p parallel cells, the array output current, i_{pv} will be

$$i_{pv} = N_p I_L - N_p I_s \big[e^{\alpha \left(\frac{v_{pv}}{N_s} + \frac{R_s i_{pv}}{N_p} \right)} - 1 \big] - \frac{N_p}{R_{sh}} \big(\frac{v_{pv}}{N_s} + \frac{R_s i_{pv}}{N_p} \big). \tag{3.5}$$

3.1.2 Modeling of Inverter and its Output Filter

By considering the inductor currents and capacitor voltage ($[i_a, i_b, i_c, v_{dc} = v_{pv}]$) as the state variables of the three-phase grid-connected PV system of Fig. 3.3, the state-space representation of this system will be [68]

$$\begin{cases} \dot{i}_a = -\frac{R}{L} i_a - \frac{1}{L} e_a + \frac{v_{pv}}{3L} \big(2S_a - S_b - S_c \big) \\ \dot{i}_b = -\frac{R}{L} i_b - \frac{1}{L} e_b + \frac{v_{pv}}{3L} \big(-S_a + 2S_b - S_c \big) \\ \dot{i}_c = -\frac{R}{L} i_c - \frac{1}{L} e_c + \frac{v_{pv}}{3L} \big(-S_a - S_b + 2S_c \big), \end{cases} \tag{3.6}$$

where, S_a, S_b, and S_c are the switching signals related to each phase of three-phase VSI, and are defined as

$$S_i (i = a, b, c) = \begin{cases} 1 \quad if \quad S_i^{TOP} : on, \quad S_i^{BOTTOM} : off \\ 0 \quad if \quad S_i^{TOP} : off, \quad S_i^{BOTTOM} : on \end{cases}. \tag{3.7}$$

On the other hand, by applying KCL to the DC link capacitor node, the state-space equation for capacitor voltage is obtained

$$\dot{v}_{pv} = \frac{1}{C} (i_{pv} - i_{dc}). \tag{3.8}$$

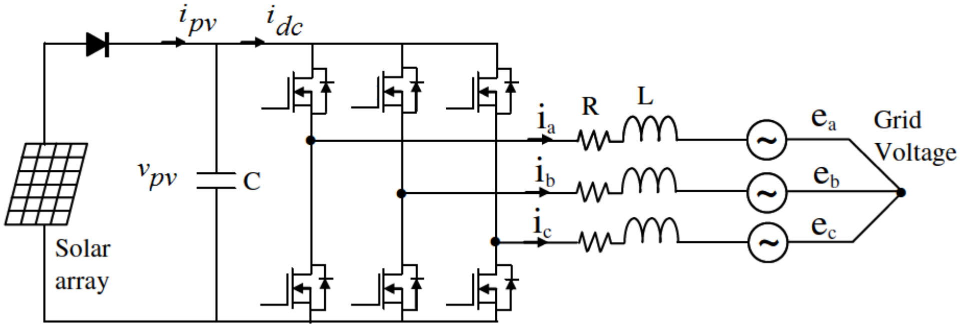

Fig. 3.3: Three-phase grid-connected scheme.

Assuming the switching losses and conduction losses of the inverter to be negligible, the input current of the inverter is equal to the output current,

$$i_{dc} = i_a S_a + i_b S_b + i_c S_c, \tag{3.9}$$

which yields,

$$\dot{v}_{pv} = \frac{1}{C} i_{pv} - \frac{1}{C}(i_a S_a + i_b S_b + i_c S_c). \tag{3.10}$$

Therefore, the state-space representation of a loss-less three-phase grid-connected PV system can be presented by

$$\begin{cases} \dot{i}_a = -\frac{R}{L} i_a - \frac{1}{L} e_a + \frac{v_{pv}}{3L}\big(2S_a - S_b - S_c\big) \\ \dot{i}_b = -\frac{R}{L} i_b - \frac{1}{L} e_b + \frac{v_{pv}}{3L}\big(-S_a + 2S_b - S_c\big) \\ \dot{i}_c = -\frac{R}{L} i_c - \frac{1}{L} e_c + \frac{v_{pv}}{3L}\big(-S_a - S_b + 2S_c\big) \\ \dot{v}_{pv} = \frac{1}{C} i_{pv} - \frac{1}{C}(i_a S_a + i_b S_b + i_c S_c). \end{cases} \tag{3.11}$$

As can be seen in (3.11), this system is a nonlinear time-varying system due to the switching functions (S_a, S_b, and S_c) and diode current (i_{pv}). In the next section, some useful transformations and strategies, which can be employed to ease the control process of this nonlinear time varying system, will be discussed.

3.2 Fundamental Transformations in Three-Phase Systems

To simplify the control design process of a three-phase grid-connected system, two fundamental transformations are used to reduce the dimensions of the mathematical model of the system and decouple the differential equations. These transformations are [26]:

- $\alpha\beta$ transformation, and
- Park transformation (or dq transformation).

3.2.1 $\alpha\beta$ Transformation

$\alpha\beta$ transformation reduces the dimensions of the state-space representation of three-phase systems. For instance, under certain conditions which will be defined later, by applying this transformation, the current loop model for the benchmark three-phase grid-connected system which is describing by three differential equations (one equation per phase) turns to a model with two differential equations. The $\alpha\beta\gamma$ transformation is defined as follows [26]:

$$\begin{bmatrix} x_\alpha \\ x_\beta \\ x_\gamma \end{bmatrix} = \sqrt{\frac{2}{3}} \underbrace{\begin{bmatrix} 1 & -\frac{1}{2} & -\frac{1}{2} \\ 0 & \frac{\sqrt{3}}{2} & -\frac{\sqrt{3}}{2} \\ \frac{1}{\sqrt{2}} & \frac{1}{\sqrt{2}} & \frac{1}{\sqrt{2}} \end{bmatrix}}_{T_{\alpha\beta\gamma}} \begin{bmatrix} x_a \\ x_b \\ x_c \end{bmatrix}, \tag{3.12}$$

where x_a, x_b, and x_c can be output currents, voltages, or powers of a three-phase system (Fig. 3.4).

From the geometrical point of view, in this transformation the three-dimensional Cartesian coordinate with the following three basis vectors,

$$\begin{bmatrix} 1 \\ 0 \\ 0 \end{bmatrix}, \quad \begin{bmatrix} 0 \\ 1 \\ 0 \end{bmatrix}, \quad \begin{bmatrix} 0 \\ 0 \\ 1 \end{bmatrix}, \tag{3.13}$$

changes to another Cartesian coordinate with different base vectors as follows:

$$\begin{bmatrix} 1 \\ -\frac{1}{2} \\ -\frac{1}{2} \end{bmatrix}, \quad \begin{bmatrix} 0 \\ \frac{\sqrt{3}}{2} \\ -\frac{\sqrt{3}}{2} \end{bmatrix}, \quad \begin{bmatrix} \frac{1}{\sqrt{2}} \\ \frac{1}{\sqrt{2}} \\ \frac{1}{\sqrt{2}} \end{bmatrix}, \tag{3.14}$$

where these new basis vectors are orthonormal (which means the inverse of $\alpha\beta\gamma$ transformation matrix is equal to its transpose). Also, this transformation is "power invariant" which means $\langle i_{abc} v_{abc} \rangle = \langle i_{\alpha\beta\gamma} v_{\alpha\beta\gamma} \rangle$ where $\langle . \rangle$ is scalar product of vectors [26].

In the symmetrical three-phase system, where $x_a + x_b + x_c = 0$, and $x_\gamma = 0$, which means the three-phase system can be represented by two vectors, x_α and x_β. On the other word, in the symmetrical three-phase system, γ axis is orthogonal to the $\alpha\beta$ plane and has no projection on this plane. In this case, the $\alpha\beta\gamma$ transformation is called $\alpha\beta$ transformation and is defined as follows [26]:

$$\begin{bmatrix} x_\alpha \\ x_\beta \end{bmatrix} = \sqrt{\frac{2}{3}} \underbrace{\begin{bmatrix} 1 & -\frac{1}{2} & -\frac{1}{2} \\ 0 & \frac{\sqrt{3}}{2} & -\frac{\sqrt{3}}{2} \end{bmatrix}}_{T_{\alpha\beta}} \begin{bmatrix} x_a \\ x_b \\ x_c \end{bmatrix}. \tag{3.15}$$

The inverse of $\alpha\beta$ transformation is

$$\begin{bmatrix} x_a \\ x_b \\ x_c \end{bmatrix} = \sqrt{\frac{2}{3}} \underbrace{\begin{bmatrix} 1 & 0 \\ -\frac{1}{2} & \frac{\sqrt{3}}{2} \\ -\frac{1}{2} & \frac{\sqrt{3}}{2} \end{bmatrix}}_{T_{\alpha\beta}^T} \begin{bmatrix} x_\alpha \\ x_\beta \end{bmatrix}. \tag{3.16}$$

Therefore, by using $\alpha\beta$ transformation, a balanced three-phase system can be mapped into a stationary two-phase system under symmetrical condition.

3.2.2 Park's (dq) Transformation

Park's transformation converts a three-phase, three-dimensional system to a two- dimensional system as $\alpha\beta$ transformation does. The difference between the $\alpha\beta$ transformation and Park's transformation is that in the $\alpha\beta$ transformation, the resulted coordinate is stationary, but in Park's transformation, this coordinate rotates with a fixed frequency.

Park's transformation consists of two rotary axes, d and q, which rotate around the static $\alpha\beta$ axis with a constant angular frequency, ω as shown in Fig. 3.4 [26].

Therefore, in the three-phase systems, the synchronous frame operates by two-stage transformations. In the first step, the three-phase output vector (current or voltage) transforms into the $\alpha\beta$ stationary frame; and in the second step, the Park's transformation provides a rotating frame for the system.

Park's transformation is defined by

$$\begin{bmatrix} x_d \\ x_q \end{bmatrix} = \underbrace{\begin{bmatrix} \cos(\theta) & \sin(\theta) \\ -\sin(\theta) & \cos(\theta) \end{bmatrix}}_{T_{dq}} \begin{bmatrix} x_\alpha \\ x_\beta \end{bmatrix}, \tag{3.17}$$

where $\theta = \omega t$ and ω is the utility grid fundamental frequency in the grid-connected system application. The equivalent complex form of (3.17) is [26]

$$\vec{x_{dq}} = x_d + jx_q = \vec{x_{\alpha\beta}} e^{-j\theta}, \tag{3.18}$$

where $x_{dq} = [x_d, x_q]^T$ and $x_{\alpha\beta} = [x_\alpha, x_\beta]^T$. Then x_d is the real part and x_q is the imaginary part of the Park's transformation. Both transformation matrices, $T_{\alpha\beta}$ and T_{dq}, are invertible, therefore the Park's transformation is invertible.

$$\begin{bmatrix} x_\alpha \\ x_\beta \end{bmatrix} = \underbrace{\begin{bmatrix} \cos(\theta) & -\sin(\theta) \\ \sin(\theta) & \cos(\theta) \end{bmatrix}}_{T_{dq}^T} \begin{bmatrix} x_d \\ x_q \end{bmatrix} \tag{3.19}$$

With the same concept, the equivalent complex form of inverse Park's transformation is $\vec{x}_{\alpha\beta} = \vec{x}_{dq} e^{j\theta}$. Since the result of Park's transformation is two vectors, d and q, this transformation is also called the dq transformation.

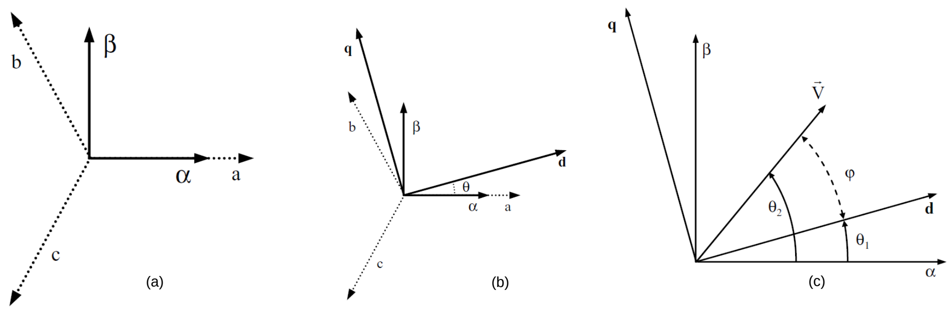

Fig. 3.4: (a) Graphical representation of $\alpha\beta$ transformation, (b) comparison between $\alpha\beta$ and Park's transformation in Cartesian coordinate, and (c) graphical representation of synchronous frame.

3.3 Mathematical Model of a Three-Phase Grid-Connected PV Systsem Using dq Transformation

As discussed before in this dissertation, the synchronous frame has be chosen to be implemented because of its advantages. In order to model the three-phase grid-connected PV system in the synchronous frame, dq transformation is employed. Applying dq transformation to (3.11), results a three-phase system in synchronous frame as follows:

$$\begin{cases} \dot{I}_d = -\frac{R}{L}I_d + \omega I_q - \frac{1}{L}E_d + \frac{\upsilon_{pv}}{L}S_d, \\ \dot{I}_q = -\frac{R}{L}I_q - \omega I_d - \frac{1}{L}E_q + \frac{\upsilon_{pv}}{L}S_q, \\ \dot{\upsilon}_{pv} = \frac{1}{C}i_{pv} - \frac{1}{C}I_dS_d - \frac{1}{C}I_qS_q. \end{cases} \tag{3.20}$$

where E_d and E_q are the direct and quadrature components of the grid voltage, and I_d and I_q are the direct and quadrature components of the output current of the inverter.

This system is a time invariant nonlinear system due to the switching terms, S_d and S_q, and diode current, i_{pv}. In this model, S_d and S_q are control inputs, and the output variables are I_d and $\upsilon_{pv} = \upsilon_{dc}$. It is desirable to have $I_q = 0$.

The active and reactive delivered powers to the grid are [70]

$$\begin{cases} P = \frac{3}{2}\big(E_dI_d + E_qI_q\big), \\ Q = \frac{3}{2}\big(E_dI_q + E_qI_d\big). \end{cases} \tag{3.21}$$

In order to write a set of linear dynamic equations for benchmark three-phase grid-connected PV system, the total inductance of the grid and inverter output filter is added together and modeled as an inductor L with equivalent series resistance (ESR) of R. Also, the grid is considered to be balanced, which means $i_a + i_b + i_c = 0$ and therefore $i_\gamma = 0$. By defining v_d and v_q as follows:

$$v_d = v_{pv} S_d, \quad v_q = v_{pv} S_q, \tag{3.22}$$

and if two nonlinear coupled terms, $L\omega I_q$ and $L\omega I_d$, are compensated by feeding-forward these two terms into the current control loop (as shown in Fig. 3.1), then the current equations of (3.20) can be rewritten as a linear time invariant equations,

$$\begin{cases} \dot{I}_d = -\frac{R}{L} I_d - \frac{1}{L} E_d + \frac{v_d}{L}, \\ \dot{I}_q = -\frac{R}{L} I_q - \frac{1}{L} E_q + \frac{v_q}{L}, \\ \dot{v}_{pv} = \frac{1}{C} i_{pv} - \frac{1}{C} I_d S_d - \frac{1}{C} I_q S_q. \end{cases} \tag{3.23}$$

By decoupling the current and voltage equations, the transfer function for current control loop will be

$$G_{AC}(s) = \frac{v_d - E_d}{I_d} = \frac{v_q - E_q}{I_q} = \frac{1}{sL + R}, \tag{3.24}$$

where v_d and v_q are the direct and quadrature components of voltage, respectively.

DC bus dynamic transfer function can be obtained from the voltage equation of (3.23),

$$G_{DC}(s) = \frac{v_{dc}}{i_{dc}} = \frac{v_{pv}}{i_{pv}} = -\frac{1}{Cs} M_{id}(s), \tag{3.25}$$

where M_{id} is the closed-loop transfer function of current control loop. $G_{DC}(s)$ describes the variations of the inverter switching to the consequent variations of the output current.

3.4 Inverter Driver

Typically, there are several requirements for any inverter driver such as [71]:

- Wide range of linear operations,
- Minimum number of switching to maintain low switching losses in power components,
- Minimum harmonic contents in voltage and current, and
- Operation in over-modulation region including square wave.

There are two general well-known PWM methods to drive the three-phase inverters:

- Carrier-based PWM (CB-PWM), and
- Space Vector Modulation (SVM).

Between these two methods, SVM generates less harmonic distortions in the output current compared to CB-PWM. In addition, SVM increases the efficiency by reducing the inverter losses. Furthermore, SVM offers more flexibility in its digital implementation [72]. For these reasons, SVM will be implemented in the simulations to drive the three-phase inverter.

In the case of two-level three-phase converters, there are two switches in each leg and they cannot be ON or OFF simultaneously because having both ON results in a short circuit and having both OFF results in an open circuit. Therefore, two-level converters provide eight possible switching states consisting of six active and two zero states [71]. According to Fig. 3.5, states are numbered in binary format (0 for OFF and 1 for ON) from 000 to 111 [26]. Each state is represented by a vector in a hexagon and has a dual with the same amplitude but with opposite direction.

$$\begin{aligned} &\vec{V}_1 = -\vec{V}_4 \\ &\vec{V}_2 = -\vec{V}_5 \\ &\vec{V}_3 = -\vec{V}_6 \\ &\vec{V}_0 = \vec{V}_7 \\ &\vec{V}_1 + \vec{V}_3 + \vec{V}_5 = 0 \end{aligned} \tag{3.26}$$

It can be seen in Fig. 3.6, that in one sampling interval, T_s, any output vector, $\vec{V}(t)$ can be implemented by summation of other vectors [26].

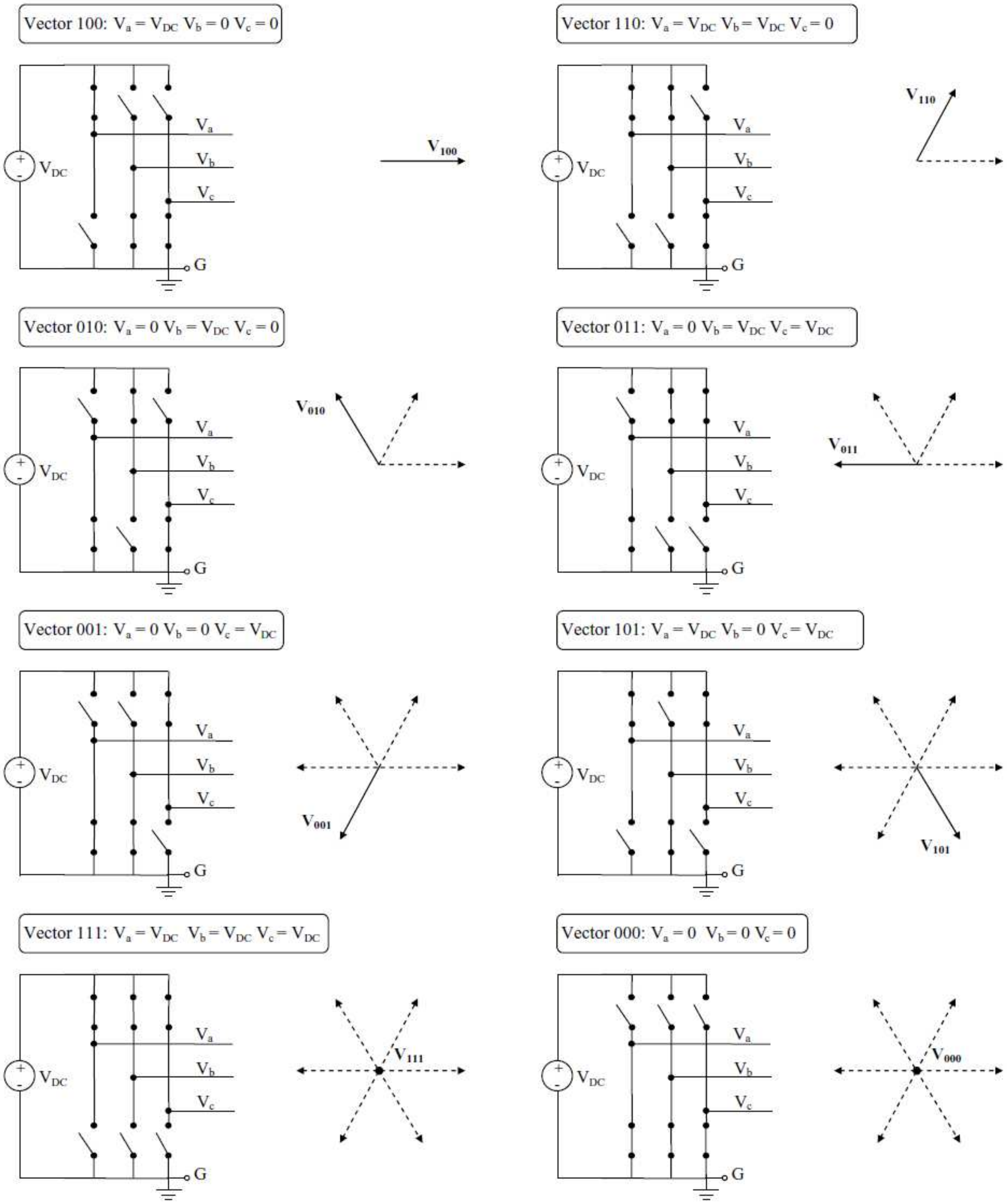

Fig. 3.5: Space vector modulation scheme.

$$\vec{V}(t) = \frac{t_0}{T_s}\vec{V}_0 + \frac{t_1}{T_s}\vec{V}_1 + \cdots + \frac{t_7}{T_s}\vec{V}_7, \tag{3.27}$$

where $t_0, t_1, \cdots, t_7$ are the turn on times for $\vec{V}_0, \vec{V}_1, \cdots, \vec{V}_7$ and $\sum_{k=0}^{7} t_k = T_s$. In Fig. 3.6, $\delta_1 = \frac{t_1}{T_s}$, $\delta_2 = \frac{t_2}{T_s}$ and $\delta_3 = \frac{t_0}{T_s}$.

Therefore, any desired vector is implementable in SVM with infinite possibilities. In order to reduce the ON/OFF time for switches, the output vector is decomposed by ON/OFF sequences of projected vectors on the two nearest state vectors. The length of each projection determines the fraction of the modulation period that will be occupied by each output vector. For instance, in area (I) (the area between V_{100} and V_{110}), in one sampling interval, the output vector $\vec{V}(t)$ can be expressed as

$$\vec{V}(t) = \frac{t_1}{T_s}\vec{V}_1 + \frac{t_2}{T_s}\vec{V}_2 + \frac{t_0}{T_s}\vec{V}_0 + \frac{t_7}{T_s}\vec{V}_7, \tag{3.28}$$

where

$$T_s - t_1 - t_2 = t_0 + t_7 \geq 0. \tag{3.29}$$

If the length of output vector is assumed to be $\vec{V} = mE$, then

$$\frac{m}{\sin(\frac{2\pi}{3})} = \frac{t_1}{T_s}\frac{1}{\sin(\frac{\pi}{3} - \phi)} = \frac{t_2}{T_s}\frac{1}{\sin(\phi)}. \tag{3.30}$$

Therefore,

$$\begin{aligned} \tfrac{t_1}{T_s} &= \tfrac{2m}{\sqrt{3}}\sin(\tfrac{\pi}{3} - \omega t) \\ \tfrac{t_2}{T_s} &= \tfrac{2m}{\sqrt{3}}\sin(\tfrac{\pi}{3}) \\ t_0 + t_7 &= T_s - t_1 - t_2. \end{aligned} \tag{3.31}$$

These equations can be rewritten as [73]

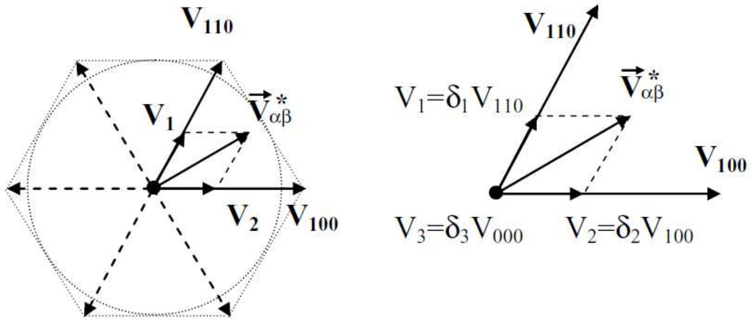

Fig. 3.6: Generating voltage reference vector by SVM.

$$\begin{aligned} \tfrac{t_1}{T_s} &= \tfrac{2m}{\sqrt{3}}\cos(\omega t + \tfrac{\pi}{6}) \\ \tfrac{t_2}{T_s} &= \tfrac{2m}{\sqrt{3}}\cos(\omega t + \tfrac{3\pi}{2}) \\ t_0 + t_7 &= T_s - t_1 - t_2. \end{aligned} \tag{3.32}$$

Decomposition of $\vec{V}$ in different areas is shown in Table 3.2 [73].

ON/OFF time interval for non-zero vectors, $\vec{V}_1, \cdots, \vec{V}_6$ are identical in all space vector PWMs. The difference between SVMs comes from the distribution of t_0 and t_7.

To maintain sinusoidal output line to line voltage, the output voltage vector $\vec{V}$ must be circular. Therefore, this trajectory is considered to be the inscribed circle of the hexagon and the length of the output vector is

$$\vec{V} = mE = \frac{\sqrt{3}}{2}E. \tag{3.33}$$

3.5 Grid Synchronization

In the synchronous frame control method, the amplitude and phase of the grid voltage needs to be known for the control system. These pieces of information are essential for the current and voltage control loops in order to stabilize the system and force it to work at its optimal point where the system will generate and deliver maximum power.

Table 3.2: Space vector modulation timing.

SVM Timing	
Area I ($0 \leq \omega t \leq \frac{pi}{3}$)	$t_1 = \frac{\sqrt{3}}{2} m T_s \cos(\omega t + \frac{\pi}{6})$ $t_2 = \frac{\sqrt{3}}{2} m T_s \cos(\omega t + \frac{3\pi}{2})$ $t_0 + t_7 = T_s - t_1 - t_2$
Area II ($\frac{\pi}{3} \leq \omega t \leq \frac{2pi}{3}$)	$t_2 = \frac{\sqrt{3}}{2} m T_s \cos(\omega t + \frac{11\pi}{6})$ $t_3 = \frac{\sqrt{3}}{2} m T_s \cos(\omega t + \frac{7\pi}{6})$ $t_0 + t_7 = T_s - t_1 - t_2$
Area III ($\frac{2\pi}{3} \leq \omega t \leq \pi$)	$t_3 = \frac{\sqrt{3}}{2} m T_s \cos(\omega t + \frac{3\pi}{2})$ $t_4 = \frac{\sqrt{3}}{2} m T_s \cos(\omega t + \frac{5\pi}{6})$ $t_0 + t_7 = T_s - t_1 - t_2$
Area IV ($\pi \leq \omega t \leq \frac{4\pi}{3}$)	$t_4 = \frac{\sqrt{3}}{2} m T_s \cos(\omega t + \frac{7\pi}{6})$ $t_5 = \frac{\sqrt{3}}{2} m T_s \cos(\omega t + \frac{\pi}{2})$ $t_0 + t_7 = T_s - t_1 - t_2$
Area V ($\frac{4\pi}{3} \leq \omega t \leq \frac{5\pi}{3}$)	$t_5 = \frac{\sqrt{3}}{2} m T_s \cos(\omega t + \frac{6\pi}{6})$ $t_6 = \frac{\sqrt{3}}{2} m T_s \cos(\omega t + \frac{\pi}{6})$ $t_0 + t_7 = T_s - t_1 - t_2$
Area V ($\frac{5\pi}{3} \leq \omega t \leq 2\pi$)	$t_6 = \frac{\sqrt{3}}{2} m T_s \cos(\omega t + \frac{\pi}{2})$ $t_1 = \frac{\sqrt{3}}{2} m T_s \cos(\omega t + \frac{11\pi}{6})$ $t_0 + t_7 = T_s - t_1 - t_2$

To obtain these vital pieces of information, a synchronization method should be employed to synchronize the inverter output and utility grid. There are various methods to extract the phase information from a given signal. In the following some of these approaches will be discussed.

3.5.1 Zero-Crossing Method

In the zero-crossing method, the phase angle of the grid is determined according to the time difference between two zero-crossing points of the grid voltage. Since the zero-crossing points are only updated at every half cycle of the utility voltage frequency, the dynamic performance of this technique is low. Other than zero-crossing delay, an additional filtering has to be applied in order to detect the fundamental frequency, which introduces extra delay to the system. Filtering delay can be improved by using special high order predictive filters without delay, but these filters add more complexity to the system. More details regarding the concept and implementation of this synchronization technique can be found in literature [18, 74].

3.5.2 $\alpha\beta$ and dq Filtering Algorithm

The grid phase angle can be obtained by filtering the grid voltage in stationary ($\alpha\beta$) or synchronous (dq) frames.

Figure 3.7 shows the schematic of these methods of synchronization [74]. As can be seen, the phase angle of the grid is extracted using filtering in either stationary or synchronous frame. In stationary frame, the arc-tangent function is directly applied to the frame but in synchronous frame, the dq signal must be transformed back into the stationary frame before applying the arc-tangent function. The drawback of this method is the use of filtering, which introduces a delay to the system, and therefore the calculated phase angle will lag the real phase angle. More details regarding the concept and implementation of this synchronization technique can be found in literature [18, 74].

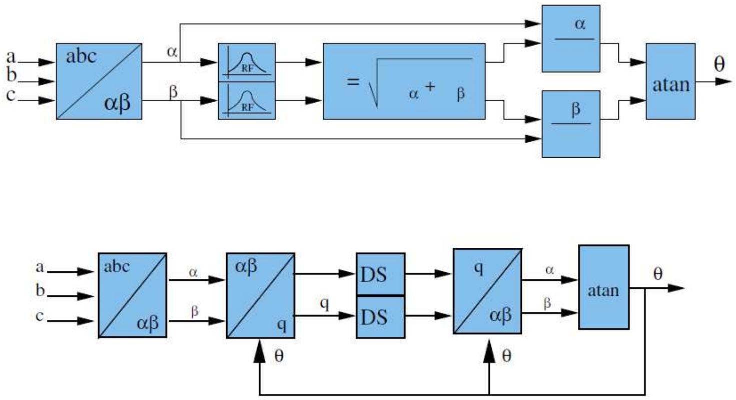

Fig. 3.7: Synchronization method using $\alpha\beta$ and dq frames.

3.5.3 Phase-Locked-Loop (PLL)

The third method of synchronization is the phase-locked-loop technique. A basic PLL circuit often consists of three essential components: a phase detector, a loop filter, and a Voltage Controlled Oscillator (VCO). Using a negative feedback loop, PLL minimizes the phase and frequency errors between the input and output signals. The schematic of PLL is depicted in Fig. 3.8.

This algorithm has better harmonic and disturbance rejection compared to zero-crossing and $\alpha\beta$-dq transformation, but during grid unbalance conditions, this algorithm requires

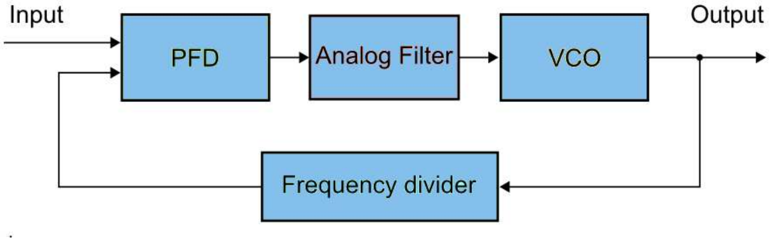

Fig. 3.8: Phase-locked-loop scheme.

further improvements. More details regarding the concept and implementation of this synchronization technique can be found in literature [74].

Because of its advantages and wide practical usage, PLL will be employed in the simulation of control system.

3.6 Summary

As mentioned earlier, a three-phase grid-connected PV system includes PV array, DC-AC inverter, and an output filter. Mathematical model of these components and some other essential sub-components like grid synchronization method and inverter driver have been introduced in this chapter. In addition, in order to simplify the control design process, some well-known transformations for three-phase systems which can reduce the dimensions of the system under a certain condition have been introduced.

Chapter 4

Maximum Power Point Tracking

4.1 Introduction

The current-voltage behavior of solar panels nonlinearly depends on the solar irradiation intensity and environmental temperature. As shown in Fig. 4.1, an increase in sun irradiation level and decrease in ambient temperature result in a higher output current and voltage [69,75]. Consequently, the environmental condition variations change the maximum output power of solar panels.

There have been various models proposed for PV cells, and among all of these models one of the simplest (which characterizes the I-V behavior of a PV cell), uses a diode in parallel with a current source [69]. Mathematical equations for this model have been discussed in Chapter 3. A model of a PV cell and its electrical characteristic is depicted in Fig. 3.2.

As mentioned before, in the grid-connected PV system, the DC link capacitor is charged by solar array, and then power is switched out from the capacitor using the power converter (inverter) and the extracted power is injected to the utility grid. To ensure that solar arrays deliver maximum available power to the converter (inverter), an interface device between converter (inverter) and PV panels needs to be employed to control the flow of power.

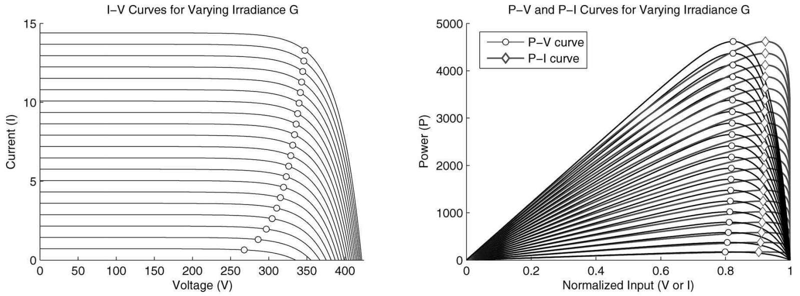

Fig. 4.1: Nonlinear behavior of voltage-current and power-current of PV panels for various sun irradiations.

Among various MPPT algorithms, convergence speed is one of the most important features which improves the efficiency and also increases the stability of the system [76–83]. Brunton et al. have pointed out [69]: "As irradiance decreases rapidly, the I-V curve shrinks and the MPV and MPI decrease. If the MPPT algorithm does not track fast enough, the control current or voltage will fall off the I-V curve."

Consequently, any improvement in the rise time of MPPT improves the reliability of the system, increases the power extraction and results higher efficiency of the whole system.

4.2 Maximum Power Point Tracking Techniques

The peak power point tracking techniques vary in many aspects, such as: simplicity, convergence speed, digital or analog implementation, sensors required, cost, range of effectiveness, etc. The MPPT implementation topology greatly depends on the end-users' knowledge. In analog world, short current (SC), open voltage (OV), and temperature methods (temperature gradient (TG) and temperature parametric equation (TP)) are good options for MPPT, otherwise with digital circuits that require the use of micro-controllers, perturbation and observation (P&O), IC (incremental conductance), and temperature methods are easy to implement [84]. Figure 4.2 and Table 4.1 present the comparison among different MPPT methods considering the costs of sensors, micro-controller, and the additional power components. In this table, *A* means absence, *L* low, *M* medium, and *H* is high [84].

Currently, the most popular and the workhorse MPPT algorithm is perturb and observe (P&O), because of its balance between performance and simplicity. However, this method suffers from the lack of speed and adaptability which are necessary for tracking the fast transient under varying environmental conditions [69].

4.2.1 Perturb and Observe Method

As mentioned before, currently, the most popular MPPT method in the PV systems is perturb and observe. In this method, a small perturbation is injected to the system and if the output power increases, a perturbation with the same direction will be injected to

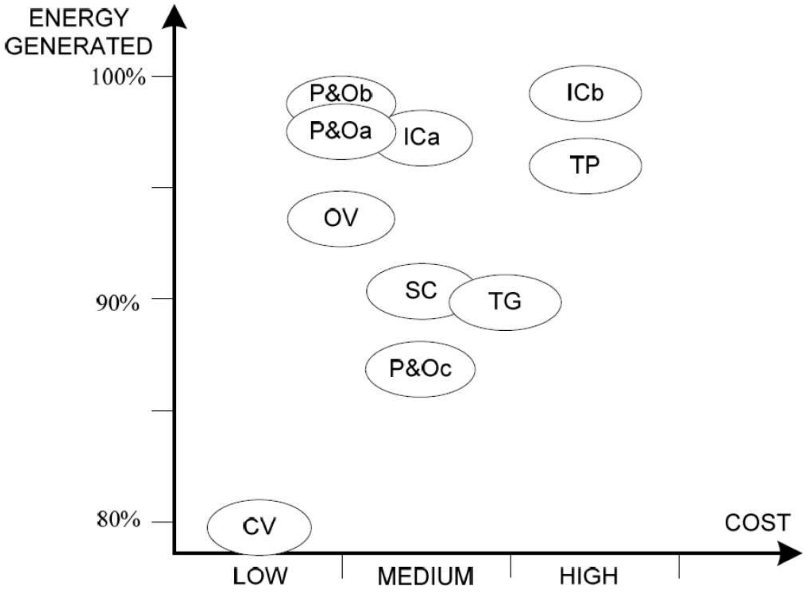

Fig. 4.2: Comparison of the MPPT methods.

Table 4.1: Comparison of MPPT algorithms.

MPPT Algorithm	Additional Components	Sensors	Micro-Controller	Total
CV	A	L	A/L	L
SC	H	M	A/L	M
OV	H	L/M	A/L	L/M
P&Oa	A	M	L	L/M
P&Ob	A	M	L	L/M
P&Oc	A	M	M	M
IC	A	M	M	M
TG	A	M/H	M	M/H
TP	A	H	M/H	H

the system and if the output power decreases, the next injected perturbation will be in the opposite direction. The scheme of P&O method is presented in Fig. 4.3.

The P&O algorithm requires few mathematical calculations which makes the implementation of this algorithm fairly simple. For this reason, P&O method is heavily used in renewable energy systems. However, the P&O algorithm is not able to distinguish the difference between the system perturbations (e.g. voltage regulation variations or environmental condition variations) and injected perturbation from P&O, and therefore it may make a wrong adjustment as the result, especially in the presence of rapid system variations.

Moreover, in the steady state operation, the power oscillates around the maximum power point, therefore the system can potentially jump to undesirable or even unstable modes. This phenomena is another disadvantage of P&O method.

Recently, a new adaptive control scheme, called extremum seeking control, has been developed [85]. In the next section, this method will be discussed and will be developed by using fractional order operators.

4.2.2 Extremum Seeking Control

A new robust MPPT algorithm is the method of extremum seeking control (ESC), which not only carries all P&O's benefits like simplicity and performance but also ameliorates its weaknesses [69].

Figures 4.4 and 4.5 present the experimental results of PV system controls by P&O and ESC MPPTs [69]. The power, current, and voltage are plotted versus time for ESC and P&O algorithms as well as the actual maximum power.

The P&O and ESC methods oscillate closely around the real maximum power voltage, as seen in the power versus time plot. Obviously, the ESC method rises to the MPP orders of magnitude more rapidly than the P&O. As mentioned before, increasing the convergence speed is an important feature for any MPPT algorithm. ESC MPPT has some advantages from hardware implementation point of view. Brunton et al. have mentioned [69]: "The ripple-based ES algorithm has good MPPT performance over a range of inverter capacitor

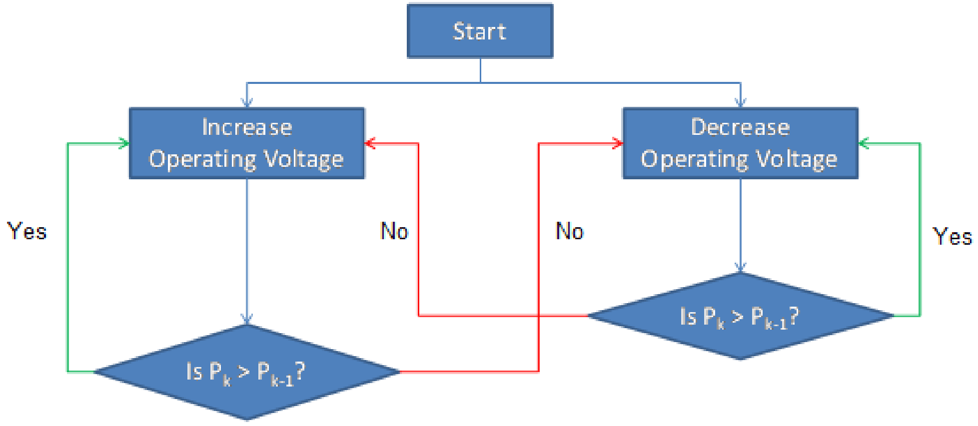

Fig. 4.3: Scheme of Perturb and Observe maximum power point tracker.

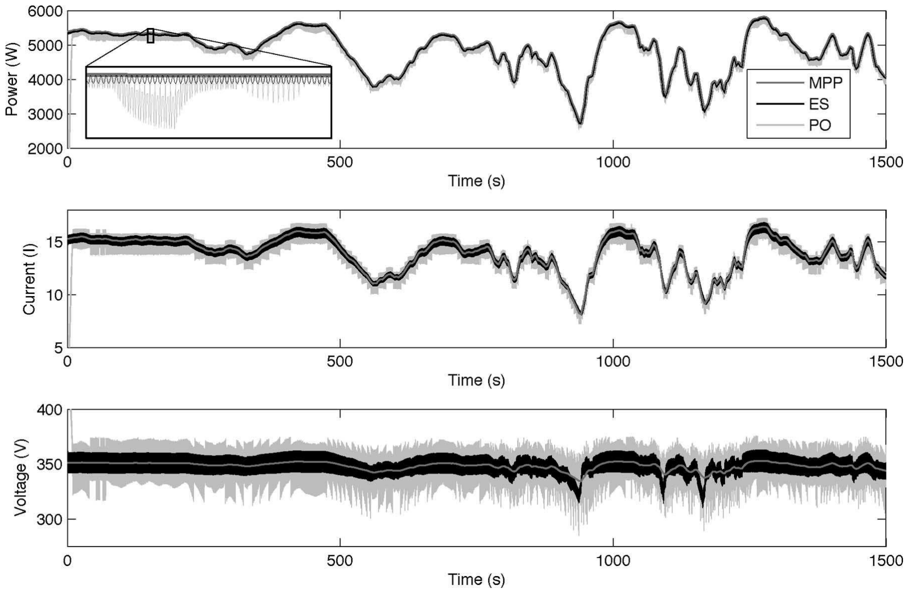

Fig. 4.4: Comparison of current controlled P&O and ESC MPPT controller.

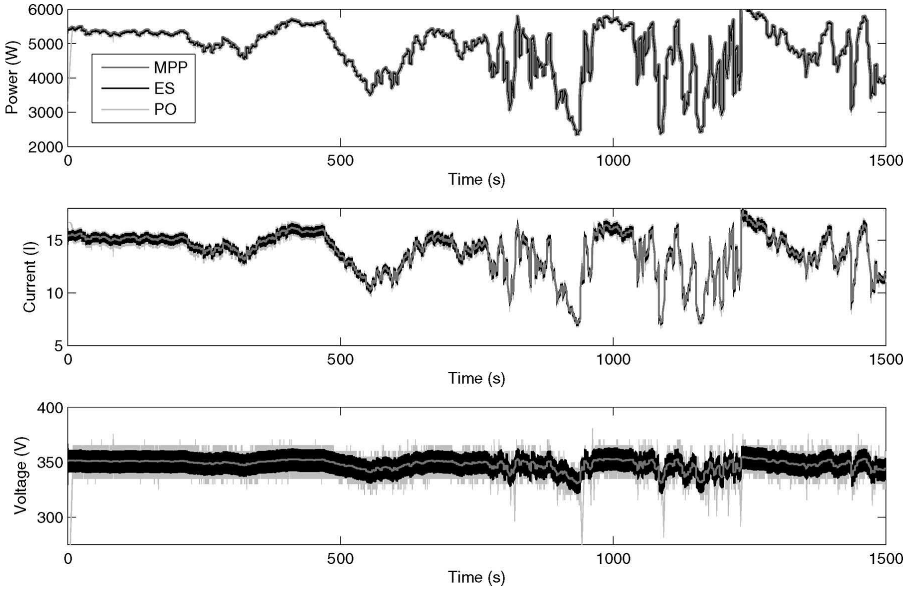

Fig. 4.5: Comparison of voltage controlled P&O and ESC MPPT controller.

sizes. Typically, the choice of capacitor is expensive because it must be well characterized and large enough to maintain a small ripple. However, because the ES control signal exploits the natural inverter ripple, a smaller capacitor allows the tracking of rapid irradiance changes. Additionally, the ES algorithm may be built using analog components and wrapped around an existing array inverter system with a voltage-control input. This may influence inverter manufacturers to provide a voltage-control input."

ESC method has been successfully applied to biochemical reactors [86, 87], ABS control in automotive brakes [88], variable timing engine operation [89], electro-mechanical valves [90], axial compressors [91], mobile robots [92], mobile sensor networks [93, 94], optical fiber amplifiers [95], and so on. A good survey of the literature on this topic prior to 1980 can be found in Sternby work [96] and a more recent overview can be found in Ariyur and Krstic work [97]. Astrom and Wittenmark rated extremum seeking as one of the most promising adaptive control methods [98].

Since extremum seeking control has better features and performance compared to P&O which is the best known MPPT algorithm, in the following, the improvement of better than the best MPPT algorithm, which is ESC, has been investigated.

4.3 How Extremum Seeking Algorithm Works

As shown in Fig. 4.6, ESC employs a slow periodic perturbation signal, $\sin(\omega t)$, which is added to the estimated signal, $\hat{\theta}$ [85]. If the perturbation signal is slow enough, then the plant appears as a static map, $y = f(\theta)$, and its dynamics do not interfere with the peak seeking scheme. If $\hat{\theta}$ is on either side of θ^*, which is the optimal point, the perturbation $a\sin(\omega t)$ will create a periodic response of y which is either in phase or out of phase with $a\sin(\omega t)$. The high-pass filter eliminates the "DC component" of y. Thus, $a\sin(\omega t)$ and high-pass filter will be approximately two sinusoidal which are in phase if $\hat{\theta} < \theta^*$ or out of phase if $\hat{\theta} > \theta^*$.

The integrator $\hat{\theta} = (\gamma/s)\chi$ approximates the gradient update law which tunes $\hat{\theta}$ [85].

The general schematic of ESC is depicted in Fig. 4.6. In Fig. 4.7, output of ESC algorithm has been illustrated when the operating point is moving from left side of optimal point to the right side of optimal point on power vs. voltage curve. In this figure, $x_1 + x_0\sin(\omega_0 t)$ is modulated input signal when the operating point is in the left side of peak power point, $x_2+x_0\sin(\omega_0 t)$ is modulated signal when the operating point is in the maximum power point and $x_3 + x_0\sin(\omega_0 t)$ is modulated output signal when the operating point is in the right side of peak power point.

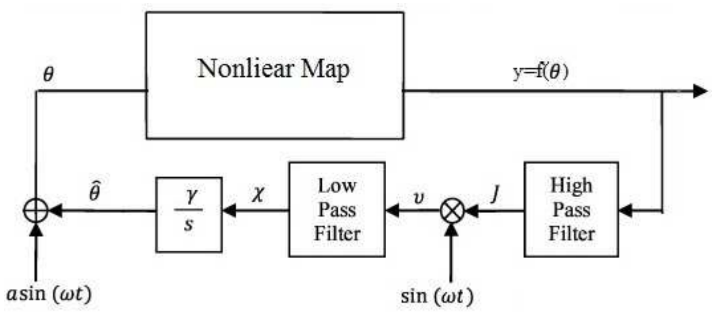

Fig. 4.6: Extremum seeking algorithm scheme.

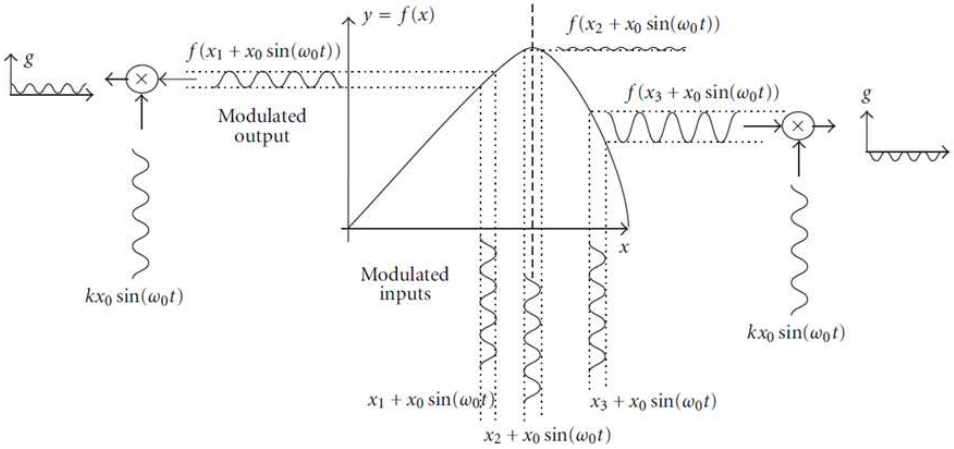

Fig. 4.7: Extremum seeking algorithm operation.

System of Fig. 4.6 can be mathematically described as follows:

$$\begin{cases} y = f(\hat{\theta} + a\sin(\omega t)) \\ \dot{\hat{\theta}} = -\gamma\chi \\ \chi = \upsilon * \mathcal{L}^{-1}\{G_{LPF}(s)\} \\ \upsilon = \left[y * \mathcal{L}^{-1}\{G_{HPF}(s)\}\right]\sin(\omega t) \end{cases}, \tag{4.1}$$

where $*$ is the convolution operator and $\mathcal{L}^{-1}$ is the inverse Laplace transform. The transfer functions for G_{HPF} and G_{LPF} in the regular SISO ESC scheme are $s/(s+\omega_h)$ and $\omega_l/(s+\omega_l)$, respectively [97]. This model will be used for stability analysis.

In the following sections, after introducing BICO filter, the advantages of using this filter in the ESC algorithm, from the stability and robustness point of view, will be discussed.

4.4 Bode's Ideal Cut-off (BICO) Filter

In this section, the filter which was strongly favored by Bode, as pointed out by Hartley and Lorenzo [99], named Bode's Ideal Cutoff Characteristic (BICO) filter is introduced. The general transfer function of a low-pass BICO filter is

$$G_{LP-BICO}(s) = \frac{k}{\left(\frac{s}{\omega_c} + \sqrt{1 + \left(\frac{s}{\omega_c}\right)^2}\right)^r}, \quad r \in \mathbb{R}^+. \tag{4.2}$$

Its corresponding time response in a special case ($\omega_c = 1 rad/s$) was found by Oberherringer and Baddi [58]. The time response in the general form for (4.2) is

$$g_{BICO_{LP}}(t) = k\frac{rJ_r(\omega_c t)}{\omega_c t}, \tag{4.3}$$

where J_r is the r-th order Bessel function.

By replacing s by $\frac{1}{s}$, the high-pass BICO filter is obtained. Figure 4.8 compares the frequency responses of high-pass BICO filter and regular first order high-pass filter ($\frac{s}{s+\omega_c}$) with the same cutoff frequency of $\omega_c = 10 rad/s$.

As can be seen in this figure, BICO filter has a sharp edge in its cutoff frequency. This great feature causes almost no attenuation for frequencies higher than ω_c and a large attenuation in the lower frequencies. Therefore, the behavior of this filter is close to an "Ideal" filter. This sharp edge feature presents in the low-pass BICO filter as well as shown in Fig. 4.9.

By combining high-pass and low-pass BICO filters, the band-pass BICO filter with sharp edges in both sides can be obtained.

4.4.1 Stability Analysis of Extremum Seeking Control Scheme

The stability analysis of ESC algorithm has been investigated in literature [85,100–102]. In all of these literature, traditional extremum seeking control with regular first order filters has been considered.

According to the previous discussion, the nonlinear map in the ESC scheme is considered to be concave and has only one extremum point. Since, in the PV system application, MPPT is employed to extract maximum amount of power from the PV panels, therefore,

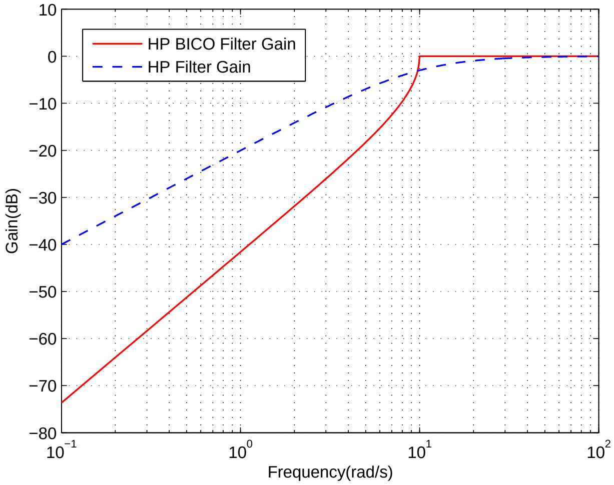

Fig. 4.8: Comparison of high-pass BICO and first order high-pass filters.

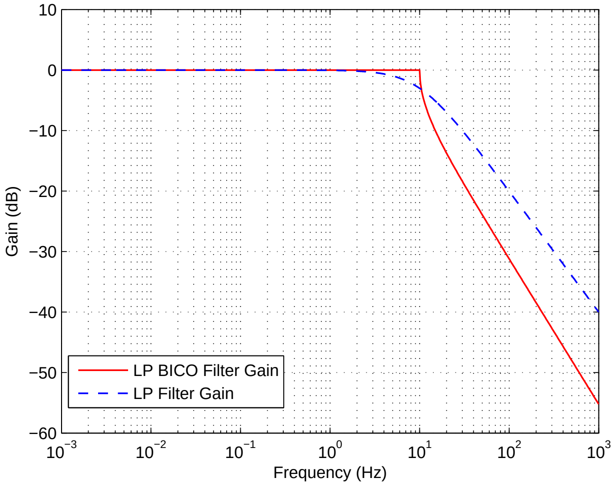

Fig. 4.9: Comparison of low-pass BICO and first order low-pass filters.

extremum point in this case is maximum point (θ^*) which means $\frac{\partial f(\theta^*)}{\partial \theta} = 0$ and, $\frac{\partial^2 f(\theta^*)}{\partial \theta^2} < 0$. According to Fig. 4.6, in the ESC algorithm, the output of nonlinear map is

$$y = f(\hat{\theta} + a\sin(\omega t)), \tag{4.4}$$

where a and ω are the amplitude and angular frequency of perturbation signal. Since the perturbation signal is assumed to be small, the Taylor expansion of (4.4) can be written as

$$y = f(\hat{\theta}) + \frac{df(\hat{\theta})}{d\hat{\theta}} a\sin(\omega t) + H.O.T., \tag{4.5}$$

where $\hat{\theta}$ is the approximation of θ^* and $H.O.T.$ stands for higher order terms. By passing y through a first order high-pass filter, the output signal will be

$$J \simeq \mathcal{L}^{-1}\{\frac{s}{s+\omega_h}\} * f(\hat{\theta}) + \mathcal{L}^{-1}\{\frac{s}{s+\omega_h}\} * \big\{\frac{df(\hat{\theta})}{d\hat{\theta}} a\sin(\omega t)\big\}. \tag{4.6}$$

First order high-pass filter acts as a derivative operator in series with a low-pass filter $(s.\frac{1}{s+\omega_h})$. By applying the derivative operator of the high-pass filter into (4.6),

$$J \simeq \mathcal{L}^{-1}\{\frac{1}{s+\omega_h}\} * \frac{df(\hat{\theta})}{dt} + \mathcal{L}^{-1}\{\frac{1}{s+\omega_h}\} * \big\{\frac{df(\hat{\theta})}{d\hat{\theta}dt} a\sin(\omega t)\big\}. \tag{4.7}$$

Multiplying the modulation signal, $\sin(\omega t)$, to the outcome of high-pass filter gives

$$v(t) \simeq \Big[\frac{df(\hat{\theta})}{dt} sin(\omega t) + \frac{df(\hat{\theta})}{2d\hat{\theta}dt} a + \frac{df(\hat{\theta})}{2d\hat{\theta}dt} a\sin(\omega t)\cos(\omega t)\Big] * \mathcal{L}^{-1}\{\frac{1}{s+\omega_h}\}. \tag{4.8}$$

Passing the modulated signal through the low-pass filter $(\frac{\omega_l}{s+\omega_l})$ results,

$$\chi(t) \simeq \Big[\frac{df(\hat{\theta})}{dt} sin(\omega t) + \frac{df(\hat{\theta})}{2d\hat{\theta}dt} a + \frac{df(\hat{\theta})}{2d\hat{\theta}dt} a\omega\sin(\omega t)\cos(\omega t)\Big] * \mathcal{L}^{-1}\{\frac{1}{s+\omega_h}\} * \mathcal{L}^{-1}\{\frac{\omega_l}{s+\omega_l}\}. \tag{4.9}$$

Under the assumptions that the amplitude of the sinusoidal perturbation is small and the harmonic of high-pass filter is attenuated by low-pass filter, output of low-pass filter is proportional to the gradient of the nonlinear map with respect to its input and time,

$$\chi \simeq \left[\frac{a}{2}\frac{df(\hat{\theta})}{d\hat{\theta}dt}\right] * \mathcal{L}^{-1}\{\frac{\omega_l}{s+\omega_l}\}. \tag{4.10}$$

The output estimated signal will be

$$\hat{\theta} \simeq \left[\frac{a}{2}\frac{df(\hat{\theta})}{d\hat{\theta}dt}\right] * \mathcal{L}^{-1}\{\frac{\omega_l}{s+\omega_l}\} * \mathcal{L}^{-1}\{\frac{\gamma}{s}\}, \tag{4.11}$$

which is equal to

$$\hat{\theta} \simeq \left[\frac{a\gamma}{2}\frac{df(\hat{\theta})}{d\hat{\theta}}\right] * \mathcal{L}^{-1}\{\frac{\omega_l}{s+\omega_l}\}. \tag{4.12}$$

Therefore in the neighborhood of the extremum point, the amplitude of output signal, $\hat{\theta}$, is small, since the gradient is small. It can be seen that the amplitude of estimated signal depends on γ and a.

4.4.2 Analysis of Averaged ESC Scheme

The averaging method is typically used to analyze the periodic steady state solutions of weakly nonlinear systems. Since the amplitude of perturbation in the ESC scheme is small, this system can be evaluated by its averaged model. The averaged form of a signal $x(t)$ is

$$\overline{x(t)} = \frac{1}{T}\int_0^T x(t)dt, \tag{4.13}$$

where $T = \frac{2\pi}{\omega}$. Therefore, the averaged model of an ESC scheme is

$$\begin{cases} \overline{\hat{\theta}} = \theta \\ \overline{y} = \overline{f(\hat{\theta})} = f(\overline{\hat{\theta}}) = f(\theta) \\ \overline{\upsilon} = \frac{a}{2}\frac{df(\overline{\theta})}{d\overline{\theta}dt} \\ \overline{\hat{\theta}} = \frac{\gamma a}{2}\frac{df(\hat{\theta})}{d\hat{\theta}} * \mathcal{L}^{-1}\{G_{LPF}(s)\} \end{cases} . \tag{4.14}$$

On the other hand, in the neighborhood of the extremum point, $y(t)$ can be approximated as

$$y \simeq f(\theta^*) + \frac{df(\theta)}{d\theta}\, |_{\theta=\theta^*}\, (\theta - \theta^*) + \frac{1}{2}\frac{d^2 f(\theta)}{d\theta}\, |_{\theta=\theta^*}\, (\theta - \theta^*)^2. \tag{4.15}$$

If the error signal between the averaged point and the extremum point is defined by $\tilde{\theta} = \overline{\theta} - \theta^*$ and since $\frac{df(\theta)}{d\theta}\, |_{\theta=\theta^*}= 0$, thus,

$$\tilde{y} \simeq \frac{1}{2}\frac{d^2 f(\theta)}{d\theta^2}\, |_{\theta=\theta^*}\, \tilde{\theta}^2. \tag{4.16}$$

By defining $\frac{1}{2}\frac{d^2 f(\theta)}{d\theta^2}\, |_{\theta=\theta^*}= K$, the local value of the nonlinear map gradient will be $\frac{df(\theta)}{d\theta}\, |_{\theta=\theta^*}= 2K\theta$. Therefore, $\frac{df(\theta)}{d\tilde{\theta}} = 2K\tilde{\theta}$. Substituting this relationship in (4.14) gives

$$\overline{\hat{\theta}} = (\gamma a K\tilde{\theta}) * \mathcal{L}^{-1}\{G_{LPF}(s)\}. \tag{4.17}$$

Without loss of generality and by assuming that $\frac{dK}{dt}$ is the output of a high-pass filter, $G_{HPF}(s)$, with a cut-off frequency higher than the cut-off frequency of a low-pass filter, $G_{LPF}(s)$, when its input signal is K, then the output of ESC scheme can be rewritten as

$$\overline{\hat{\theta}} = \big(\gamma a \theta^* K\big)\mathcal{L}^{-1}\{G_{HPF}(s)\} * \mathcal{L}^{-1}\{G_{LPF}(s)\} * \mathcal{L}^{-1}\{\frac{1}{s}\}. \tag{4.18}$$

This system can be considered as a feedback system as shown in Fig. 4.10. The loop gain of this system depends on the demodulation gain, a, the integral gain, γ, and the curvature of nonlinear map, K. This result completely matches with the results obtained from other stability analysis methods [85, 100–102].

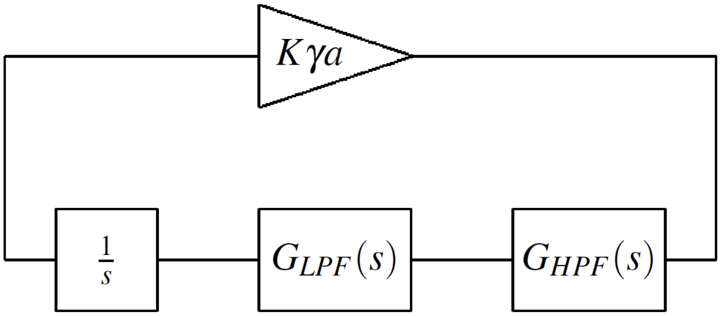

Fig. 4.10: Averaged BICO ESC scheme.

4.4.3 Stability Analysis of BICO ESC and Regular ESC

In order to compare the qualitative behavior of the averaged models of BICO MPPT and regular SISO ESC, different stability analysis method can be chosen.

Before starting stability analysis, it is important to point out that the curvature constant, K, is an uncertain parameter which depends on different factors like the PV panel manufacturer and weather conditions. The range of variation for curvature constant is $K \in [-0.5, -5]$ [102].

According to Fig. 4.10, the characteristic polynomial of averaged ESC system is $1 + aK\gamma G_{LPF}(s)G_{HPF}(s)$. To analyze the behavior of this system, root locus analysis method is employed. Since there is no command in MATLAB to plot BICO root-locus, this equation has been solved for different values of $a\gamma$ and the roots have been plotted in Fig. 4.11.

To compare the behavior of a regular SISO ESC with BICO ESC, the root-locus of characteristic polynomial of ESC has been plotted with the same method instead of using the "rlocus" command.

Figure 4.11 shows the comparison between the root-locus of averaged ESC using BICO and regular first-order filters. In these plots, the constant gain is assumed to be $a\gamma = 1$ and cut-off frequency in both BICO and first-order filters is assumed to be $\omega_c = 10 rad/s$. Clearly, by using first-order filter in the averaged ESC scheme, for some values of K, system has complex poles which cause an oscillatory behavior in the response of the system. On the other hand, by using BICO filter, roots of the characteristic polynomial are always real for any K. Consequently, using a BICO filter allows higher values of gain which means system can work not only in the wider range of environmental conditions but also it can work with different PV manufacturers.

Besides the location of the poles, as can be seen in the figure, for the same value of K, BICO ESC has farther poles with respect to the origin compared to the regular ESC. Therefore, the bandwidth of the BICO ESC is higher than the regular ESC with similar coefficients. Higher bandwidth means faster response for the BICO ESC.

Since the bandwidth of BICO is close to the bandwidth of the ideal filter, BICO ESC becomes the fastest achievable MPPT algorithm.

4.4.4 BICO ESC Simulations Results

Figures 4.12 and 4.13 show the maximum power point of a PV panel with the defined parameters in Table 3.1. As seen in these figures, environmental conditions and especially variations in sun irradiation will change the nonlinear P-V curve of PV panels. Shadows, cloudy or dusty weather, and temperature variations cause moving of the optimal operating point in PV panels.

When temperature increases, the maximum output power of PV panels decreases and vice versa. In Fig. 4.12 the variations of the optimal operating point by environmental temperature variations from 20^oC to 30^oC is illustrated. As Fig. 4.13 presents, sun irradiation variations causes a wide range of changed in the maximum output power.

To compare the proposed MPPT method, which is called BICO MPPT, with the ESC MPPT, the working conditions of both algorithms have been considered to be similar. For all simulations, the ambient temperature is 25^oC and the irradiation is assumed to be $1000W/m^2$. The cut-off frequency of high-pass filter is $\omega_h = 100rad/s$ and for low-pass filter this frequency is $\omega_l = 50rad/s$. Under these conditions, from Fig. 4.12, the maximum amount of power which can be extracted from a simulated PV panel is 48 Watts and this peak power happens around 17 Volts. To implement the BICO MPPT, the discrete approximation of this filter in MathWorks Inc's website has been used.

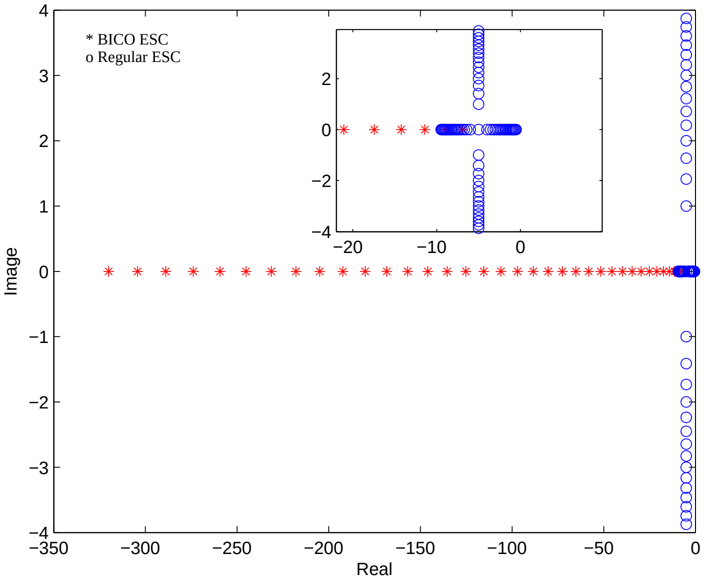

Fig. 4.11: Root-locus of the averaged BICO ESC and the averaged regular SISO ESC.

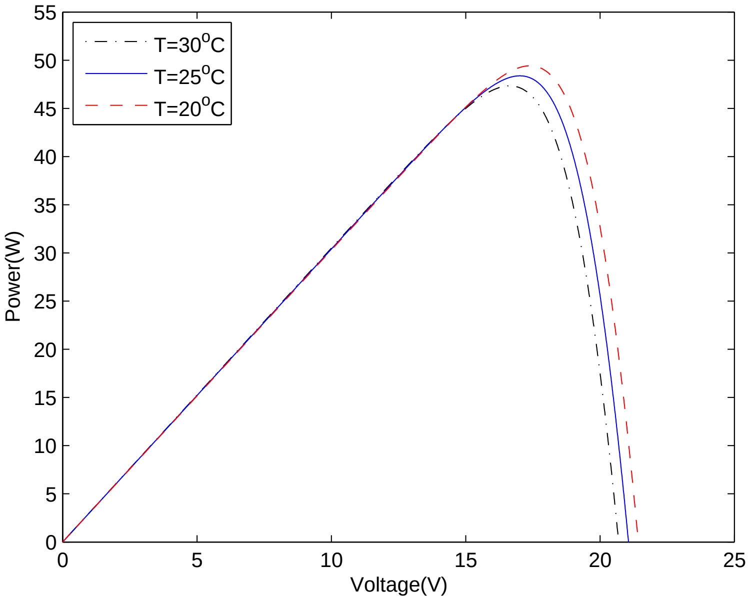

Fig. 4.12: P-V chart of considered PV model for different temperature (irradiation = 1000 W/m^2).

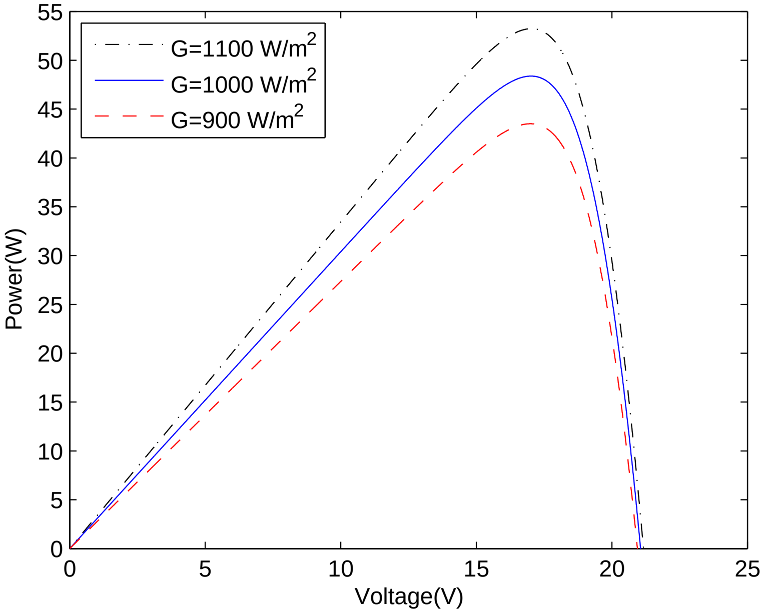

Fig. 4.13: P-V chart of considered PV model for different sun irradiation (temperature = 25^oC).

Figure 4.14 shows the outputs of peak power seeking algorithms resulted from two different MPPT methods and Fig. 4.15 represents the maximum voltage tracking in BICO ESC and regular ESC algorithms. As expected and proved before, the BICO ESC converges to the maximum power point two times faster than the regular ESC algorithm. Faster convergence speed is due to the higher bandwidth of the averaged BICO system compared to the regular ESC.

Figures 4.16 and 4.17 show the performance of the proposed MPPT compared to the regular SISO ESC in the presence of white noise. As can be seen in these figures, in the presence of a white noise (Noise power= 0.04), which is considered as the variations in the nonlinear map behavior, K, BICO MPPT performs better than the ESC MPPT from noise rejection and tracking point of view.

Another parameter which is considered in this simulations is the robustness of these two algorithms against the system gain variations. Figure 4.18 illustrates the performance of BICO and regular ESC MPPT to the gain variations. Clearly, the BICO MPPT can tolerate higher gain variations without any oscillation but by increasing the gain of the integrator in the regular ESC MPPT, it starts oscillating.

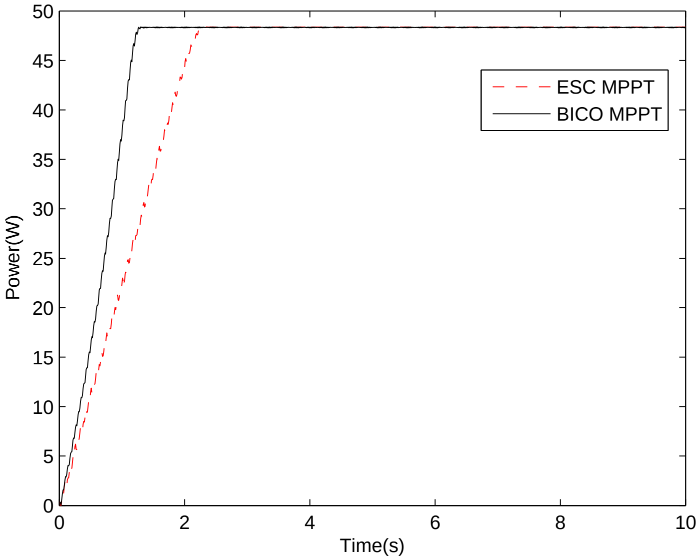

Fig. 4.14: Comparison of power tracking by BICO MPPT and ESC MPPT.

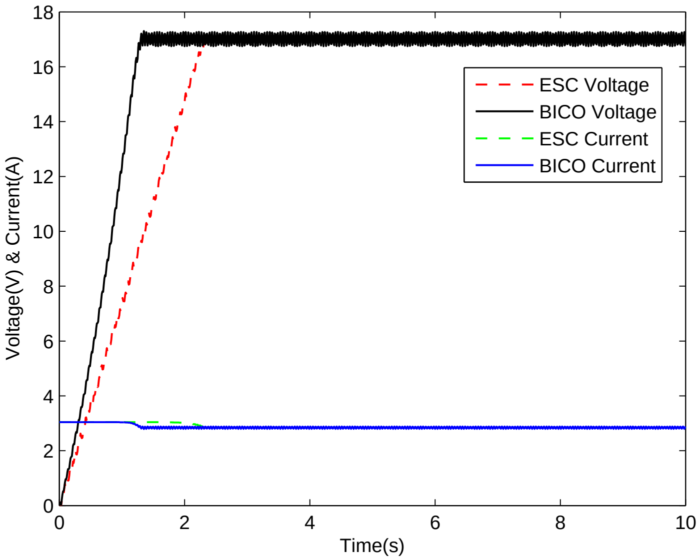

Fig. 4.15: Comparison of voltage and current tracking by BICO MPPT and ESC MPPT.

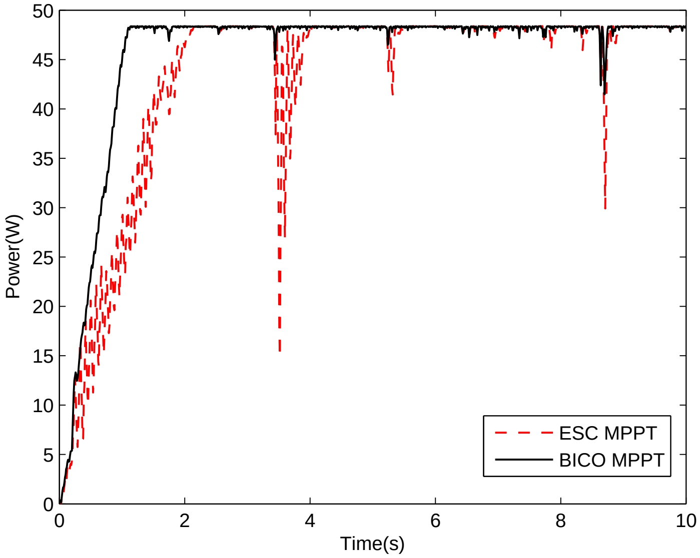

Fig. 4.16: Performance of BICO MPPT and ESC MPPT in the presence of a white noise with PSD= $0.04W/Hz$.

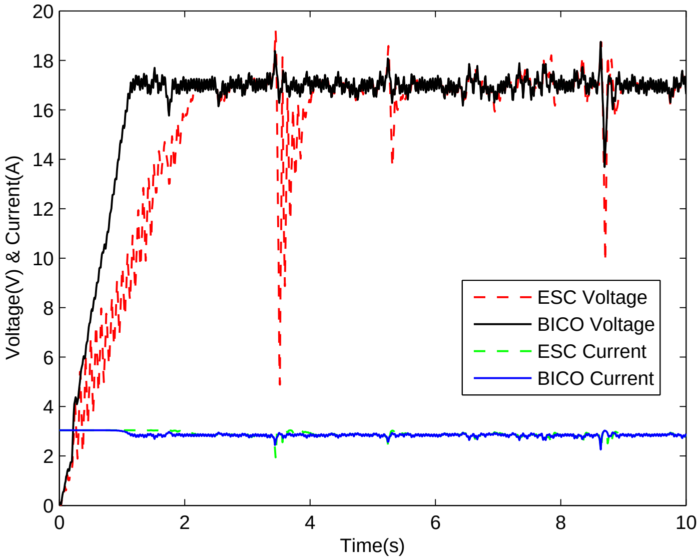

Fig. 4.17: Voltage and current tracking of BICO MPPT and ESC MPPT in the presence of a white noise with PSD= $0.04W/Hz$.

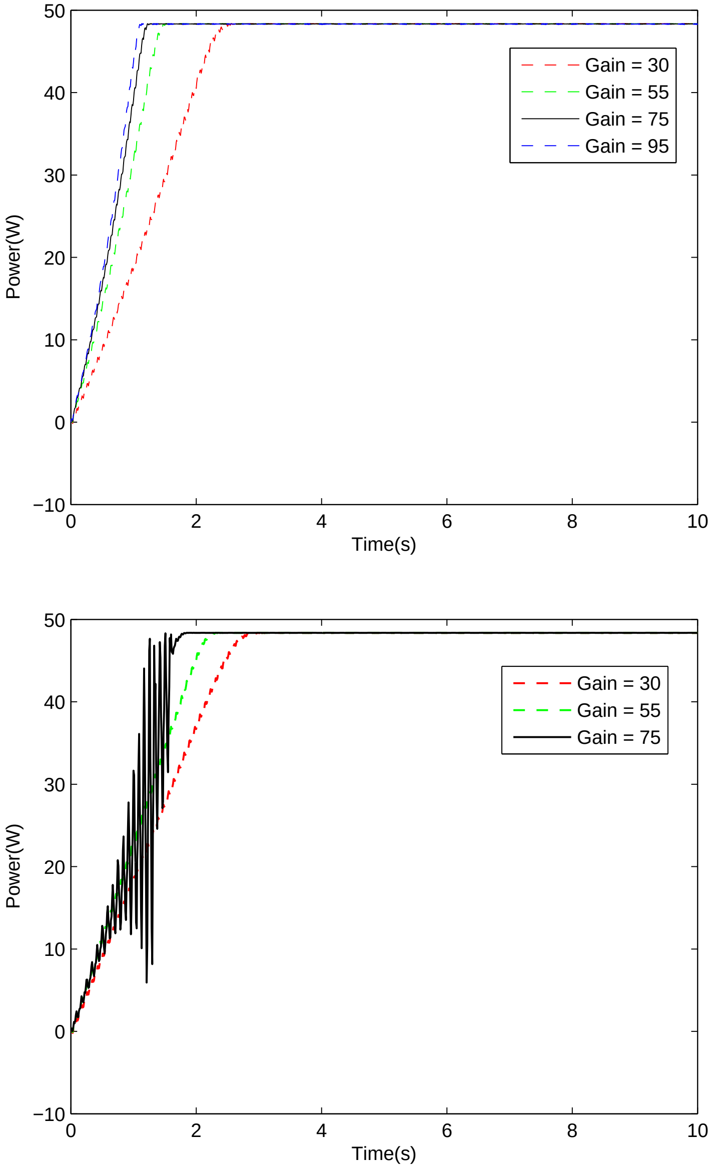

Fig. 4.18: Performance of BICO ESC and regular ESC to the loop-gain variation.

ESC MPPT response can be improved by using fractional order integrator instead of the integer order integrator in the ESC scheme. In the next section, the ESC scheme with a fractional order integrator will be investigated.

4.5 Fractional Order Extremum Seeking Control

As mentioned before, ESC is an online adaptive optimization algorithm which drives the process to its optimal operating point where the defined cost function is minimized or maximized. This controller consists of three main components:

- The cost function which in this work is the output power of PV system,
- The gradient estimator to approximate the variation direction, and
- The optimizer which minimize (maximize) the cost function.

In the integer order perturbation based ESC of Fig. 4.19, the averaged linearized model relating the optimized point θ^* and the error signal $\tilde{\theta}$ is [103]

$$\frac{\tilde{\theta}}{\theta^*} = \frac{1}{1 + L(s)}, \tag{4.19}$$

where $\tilde{\theta} = \theta - \theta^*$ and

$$L(s) = \frac{\gamma a^2}{2s}\Big(e^{j\phi}\frac{s + j\omega}{s + j\omega + \omega_h} + e^{-j\phi}\frac{s - j\omega}{s - j\omega + \omega_h}\Big). \tag{4.20}$$

As Krstic stated [103]: "If the average model is asymptotically stable, $1/\omega$ is sufficiently small and the initial conditions are small in an appropriate sense, then the theorem would claim the existence of an exponentially stable periodic solution which is at a distance that continuously depends on $1/\omega$, a, and γ."

If the phase delay of the perturbation signal is assumed to be $\phi = 0$, then (4.19) is asymptotically stable for all $\gamma > 0$. In the case of SISO ESC (Fig. 4.19), by assuming $\phi = 0$, the averaged linearized model relating θ^* and $\tilde{\theta}$ is [103]

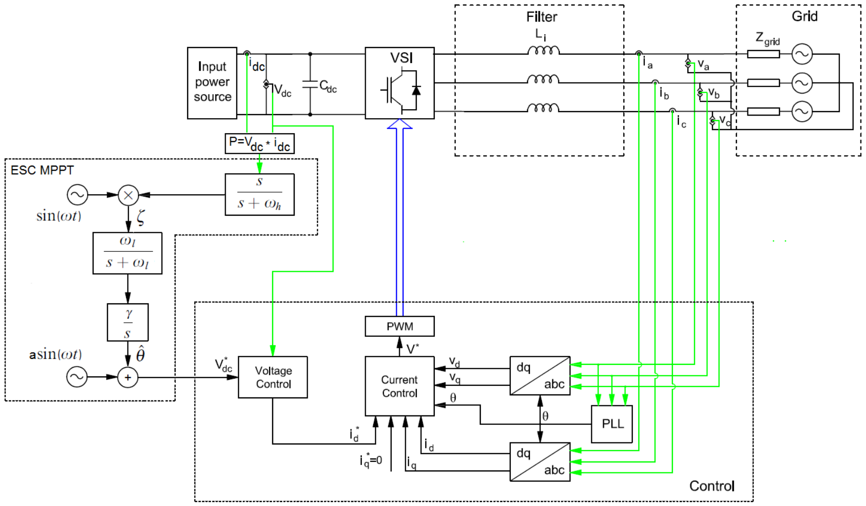

Fig. 4.19: Integer order extremum seeking control scheme in a three-phase grid-connected PV system.

$$\frac{\tilde{\theta}(s)}{\theta^*(s)} = \frac{s(s^2 + 2\omega_h s + \omega_h^2 + \omega^2)}{s^3 + (2\omega_h + ka^2)s^2 + (\omega_h^2 + \omega^2 + ka^2\omega_h)s + ka^2\omega^2}. \tag{4.21}$$

By replacing integer order filters with fractional order filters in the gradient estimator and optimizer of ESC, fractional order extremum seeking control (FO-ESC) will be created. Figure 4.20 illustrates a three-phase grid-connected PV system using new proposed FO-ESC.

In order to calculate a similar relationship between the optimal point and error signal for FO-ESC as shown for IO-ESC in (4.21), following lemmas should be proved in the fractional order systems:

Lemma 1: (Modulation property for fractional order systems) If all poles of a fractional order system, $H(s^q)$, are stable, then for any real φ,

$$H(s^q)[\sin(\omega t - \varphi)] = Im\{H\big((j\omega)^q\big)e^{j(\omega t - \varphi)}\} + \epsilon^{-t}. \tag{4.22}$$

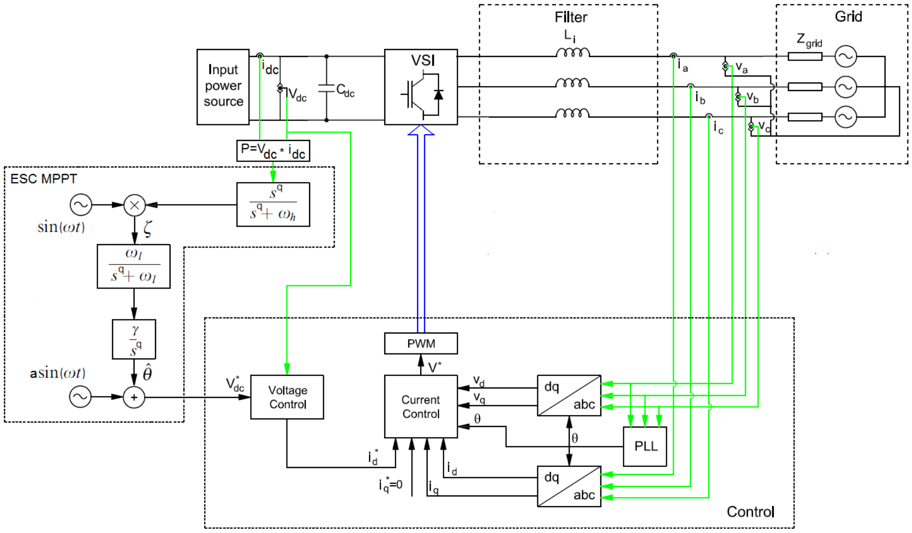

Fig. 4.20: Fractional order extremum seeking control scheme in a three-phase grid-connected PV system.

Note 1: $A(s)[u(t)]$ means a time domain signal obtained as the output of $A(s)$ driven by $u(t)$.

Note 2: Generally $H(s^q)$ can be any LTI fractional order system and this notation does not mean that the system must be commensurate order.

Proof:

$$\begin{aligned} H(s^q)[\sin(\omega t-\varphi)] &= H(s^q)[Im\{e^{j(\omega t-\varphi)}\}] \\ &= \frac{1}{2j}H(s^q)[e^{-j(\omega t-\varphi)} - e^{j(\omega t-\varphi)}] \\ &= \frac{1}{2j}\mathcal{L}^{-1}\{H(s^q)\frac{1}{s-j\omega}e^{-j\varphi} - H(s^q)\frac{1}{s+j\omega}e^{j\varphi}\}. \end{aligned} \tag{4.23}$$

By defining $H(s^q) = \frac{Z(s^q)}{P(s^q)}$ and using partial fraction decomposition, (4.23) will be expanded as follows:

$$\begin{aligned}&\frac{1}{2j}\mathcal{L}^{-1}\{H(s^q)\frac{1}{s-j\omega}e^{-j\varphi}-H(s^q)\frac{1}{s+j\omega}e^{j\varphi}\}\\&\qquad=\frac{1}{2j}\mathcal{L}^{-1}\Big\{H((j\omega)^q)\frac{1}{s-j\omega}e^{-j\varphi}-H((j\omega)^q)\frac{1}{s+j\omega}e^{j\varphi}+\frac{Z_1(s^q)}{P_1(s^q)}+...+\frac{Z_n(s^q)}{P_n(s^q)}\Big\},\end{aligned}\tag{4.24}$$

where

$$Z_i(s)_{i=1,\dots,n}=Res\Big(P_i(s)H(s^q)\frac{(j\omega+s)e^{-j\varphi}+(j\omega-s)e^{j\varphi}}{s^2+\omega^2},p_i\Big),\tag{4.25}$$

where Res stands for residue, $P_i(s)$'s are the factors of $P(s^q)$ and p_i's are the poles of $H(s^q)$. Since $H(s^q)$ is assumed to be stable, then $\frac{Z_1(s^q)}{P_1(s^q)}+...+\frac{Z_n(s^q)}{P_n(s^q)}$ will be decayed exponentially (ϵ^{-t}) which means these terms does not affect the steady state response of the system. In other words,

$$\begin{aligned}&H(s^q)[\sin(\omega t-\varphi)]\\&\qquad=\frac{1}{2j}\mathcal{L}^{-1}\Big\{H((j\omega)^q)\frac{1}{s-j\omega}e^{-j\varphi}-H((j\omega)^q)\frac{1}{s+j\omega}e^{j\varphi}\Big\}+\epsilon^{-t}\\&\qquad=Im\{H\big((j\omega)^q\big)e^{j(\omega t-\varphi)}\}+\epsilon^{-t}.\diamond\end{aligned}\tag{4.26}$$

Lemma 2: If fractional order systems, $G(s^\beta)$ and $H(s^\alpha)$ are stable, then for any real φ and a uniformly bounded $u(t)$,

$$G(s^\beta)[H(s^\alpha)[\sin(\omega t-\varphi)]u(t)]=Im\Big\{H((j\omega)^\alpha)e^{j(\omega t-\varphi)}H((j\omega)^\alpha)G(s^\beta+j\omega)[u(t)]\Big\}+\epsilon^{-t}.\tag{4.27}$$

Proof: From Lemma 1,

$$\begin{aligned} G(s^{\beta})[H(s^{\alpha})[\sin(\omega t-\varphi)]u(t)] &= G(s^{\beta})[Im\{H((j\omega)^{\alpha})e^{j(\omega t-\varphi)}\}[u(t)+\epsilon^{-t}] \\ &= Im\{e^{-j\varphi}\mathcal{L}^{-1}\{G(s^{\beta})H((j\omega)^{\alpha})U(s-j\omega)\}\}+\epsilon^{-t}. \end{aligned} \tag{4.28}$$

If $G(s^{\beta}) \xrightarrow{\mathcal{L}^{-1}} g(t)$ and $U(s) \xrightarrow{\mathcal{L}^{-1}} u(t)$, then,

$$\begin{aligned} \mathcal{L}^{-1}\{G(s^{\beta})U(s-j\omega)\} &= g(t)\star u(t)e^{j\omega t} \\ &= \int_{-\infty}^{+\infty} g(\tau)u(t-\tau)e^{j\omega(t-tau)}d\tau \\ &= e^{j\omega t}\int_{-\infty}^{+\infty} g(\tau)e^{-j\omega\tau}u(t-\tau)d\tau \\ &= e^{j\omega t}\mathcal{L}^{-1}\{G(s^{\beta}+j\omega)U(s)\}. \end{aligned} \tag{4.29}$$

Therefore, (4.28) can be rewritten as

$$\begin{aligned} &Im\{e^{-j\varphi}\mathcal{L}^{-1}\{G(s^{\beta})H((j\omega)^{\alpha})U(s-j\omega)\}\}+\epsilon^{-t} \\ &\qquad= Im\Big\{e^{j(\omega t-\varphi)}H((j\omega)^{\alpha})\mathcal{L}^{-1}\{G(s^{\beta}+j\omega)U(s)\}\Big\}+\epsilon^{-t} \\ &\qquad= Im\Big\{e^{j(\omega t-\varphi)}H((j\omega)^{\alpha})G(s^{\beta}+j\omega)[u(t)]\Big\}+\epsilon^{-t}.\diamond \end{aligned} \tag{4.30}$$

Also it can be easily verified that for fractional order systems $A(.)$ and $B(.,.)$ the following is true:

$$\begin{aligned} &Im\{e^{j(\omega t-\varphi)}A(s^{q})\}Im\{e^{j(\omega\tau-\phi)}B(s^{q},(j\omega)^{q}))[z(t)]\} \\ &= \frac{1}{2}Re\{e^{j(\varphi-\phi)}A((-j\omega)^{q})B(s^{q},(j\omega)^{q})[z(t)]\}-\frac{1}{2}Re\{e^{j(2\omega\tau-\varphi-\phi)}A((-j\omega)^{q})B(s^{q},(j\omega)^{q})[z(t)]\}. \end{aligned} \tag{4.31}$$

Therefore, as shown in Fig. 4.20, by replacing the integer order filters with fractional order ones, the mathematical FO-ESC model will be

$$\begin{cases} y(t) = f^* + (\theta(t) - \theta^*(t)) \\ \theta(t) = a\sin(\omega t) - \frac{k}{s^q}[\zeta(t)] \\ \zeta(t) = a\sin(\omega t - \varphi)\frac{s^q}{s^q+\omega_h}[y(t)] \end{cases} . \tag{4.32}$$

Without loss of generality and to simplify the analysis, the low-pass filter in the FO-ESC structure has been neglected. By defining $\tilde{\theta} = \theta^* - \theta + a\sin(\omega t)$ (to simplify the notation, the input time argument is eliminated),

$$\begin{aligned} \tilde{\theta} &= \theta^* + \frac{k}{s^q}[a\sin(\omega t - \varphi)\frac{s^q}{s^q+\omega_h}[y]] \\ &= \theta^* + \frac{k}{s^q}[a\sin(\omega t - \varphi)\frac{s^q}{s^q+\omega_h}[f^* + (\theta - \theta^*)^2]] \\ &= \theta^* + \frac{k}{s^q}[a\sin(\omega t - \varphi)\frac{s^q}{s^q+\omega_h}[f^*] + a\sin(\omega t - \varphi)\frac{s^q}{s^q+\omega_h}[\tilde{\theta}^2] \\ &+ a\sin(\omega t - \varphi)\frac{s^q}{s^q+\omega_h}[a^2\sin^2(\omega t)] - 2a\sin(\omega t - \varphi)\frac{s^q}{s^q+\omega_h}[a\tilde{\theta}\sin(\omega t)]]. \end{aligned} \tag{4.33}$$

Then,

$$\begin{aligned} &\tilde{\theta} + \frac{2ka^2}{s^q}[\sin(\omega t - \varphi)\frac{s^q}{s^q+\omega_h}[a\tilde{\theta}\sin(\omega t)]] \\ &= \theta^* + \frac{k}{s^q}[a\sin(\omega t - \varphi)\frac{s^q}{s^q+\omega_h}[f^*] + a\sin(\omega t - \varphi)\frac{s^q}{s^q+\omega_h}[\tilde{\theta}^2] \\ &+ a\sin(\omega t - \varphi)\frac{s^q}{s^q+\omega_h}[a^2\sin^2(\omega t)]]. \end{aligned} \tag{4.34}$$

By applying Lemma 1 and Lemma 2 and following the length calculations, the averaged linearized model relating the optimized point θ^* and the error signal $\tilde{\theta}$ in the FO-ESC will be derived,

$$\frac{\tilde{\theta}}{\theta^*} = \frac{1}{1 + L(s)}, \tag{4.35}$$

where $L(s)$ will be

$$L(s) = \frac{\gamma a^2}{s^q} \frac{s^{2q} + \omega_h s^q + \omega^2}{s^{2q} + 2\omega_h s^q + \omega^2 + \omega_h^2}. \tag{4.36}$$

If s^q is replaced by $\lambda = s^q$, the averaged linearized model is obtained by

$$\frac{\tilde{\theta}(\lambda)}{\theta^*(\lambda)} = \frac{\lambda(\lambda^2 + 2\omega_h \lambda + \omega_h^2 + \omega^2)}{\lambda^3 + (2\omega_h + ka^2)\lambda^2 + (\omega_h^2 + \omega^2 + ka^2\omega_h)\lambda + ka^2\omega^2}. \tag{4.37}$$

Root-locus method will be employed to compare the stability and behavior of linearized averaged model of IO-ESC and FO-ESC. The root-locus of (4.21) and (4.37) for $\omega_h = 0.1 rad/s, \gamma = 10, \omega = 2\pi rad/s, a = 1$ and $q = 0.2$ is depicted in Fig. 4.21. As shown in this figure, the averaged model of IO-ESC has a pair of poles close to the imaginary axis which will be damped lightly and consequently, this algorithm will have a longer settling time. However, in the averaged model of FO-ESC there is no pole close to the stability boundaries as shown in Fig. 2.4, and consequently, the system will have a monotonically decreasing response as discussed in Chapter 2.

Since replacing fractional order filters in the ESC algorithm add more values to this algorithm from stability and robustness point of view, in the following section the stability of FO-ESC will be investigated in details.

4.6 Stability of Fractional Order ESC

Mathematical model for the proposed fractional order ESC, shown in Fig. 4.22, can be written as

$$\begin{cases} x^{(q)} = f(x, u(x, \theta)) \\ y = h(x) \end{cases}. \tag{4.38}$$

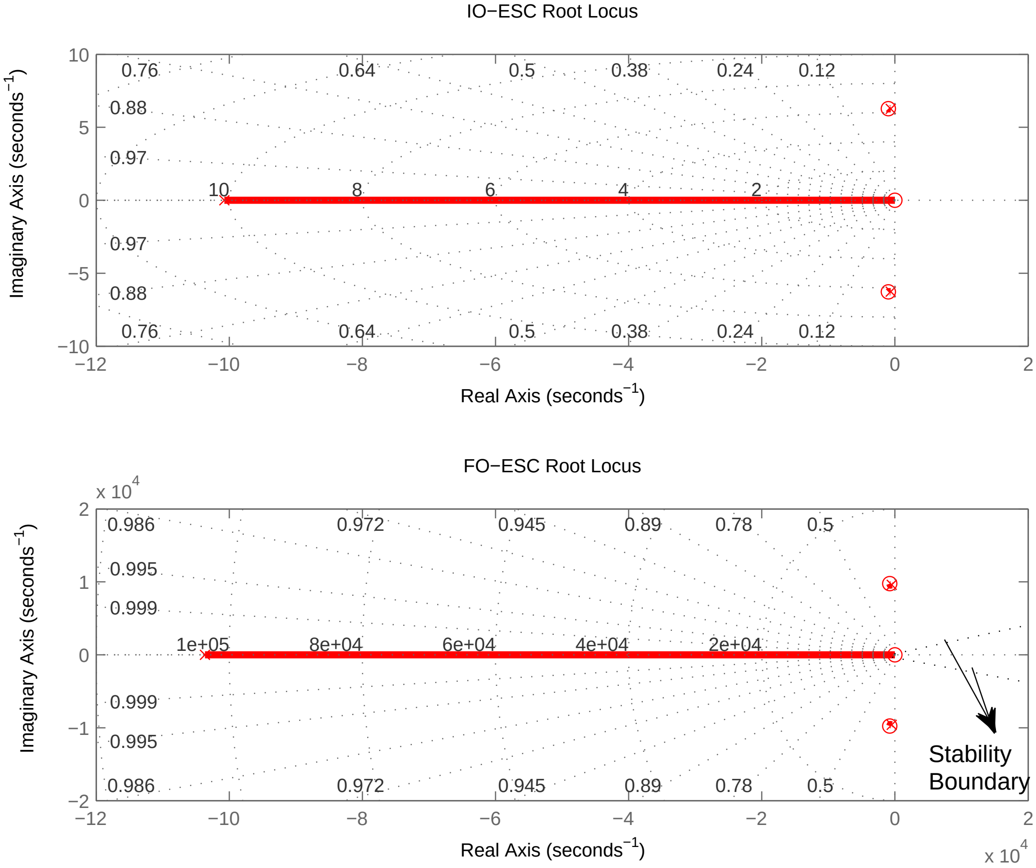

Fig. 4.21: Root-locus of averaged model IO-ESC and averaged model FO-ESC.

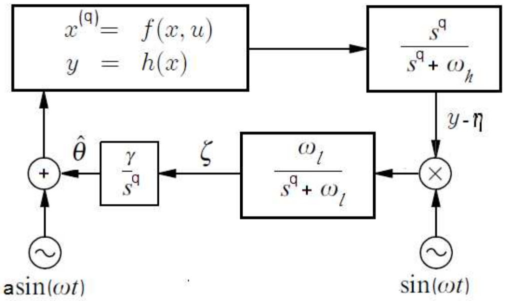

Fig. 4.22: General scheme of FO-ESC.

The mapping function, $x^{(q)} = f(x, u(x, \theta))$, is assumed to be a smooth function of θ and should have an extremum point. Assume that there is a control law, $u(x, \theta)$, which asymptotically stabilizes (4.38) at $x = l(\theta)$ which is the equilibrium of the system. The key role of ESC is to drive θ to the optimal points θ^*, such that $y = h(x) = h \circ l(\theta)$ is at its extremum value.

Before going into more details of stability analysis, let us get back to the first order FO-ESC scheme and substitute the general form of ESC equations in (4.38) with SISO FO-ESC. The mathematical model for this system will be

$$\begin{cases} \frac{d^q}{dt^q} x = f(x, u(x, \theta)) \\ \frac{d^q}{dt^q} \hat{\theta} = k\zeta \\ \frac{d^q}{dt^q} \zeta = -\omega_l \zeta + \omega_l (y - \eta) a \sin(\omega t) \\ \frac{d^q}{dt^q} \eta = -\omega_h \eta + \omega_h y, \end{cases} \tag{4.39}$$

where $\frac{d^q}{dt^q}$ is fractional order Caputo derivative and $q \in (0, 1]$. As mentioned before, the equilibrium of this system is assumed to be $x = l(\theta)$ which at this point, $\frac{d^q}{dt^q} x = 0$ and also $f(x, u(x, \theta)) = 0$. Since $\theta = \hat{\theta} + a \sin(\omega t)$, the equilibrium of the system can be defined as $x = l(\hat{\theta} + a \sin(\omega t))$.

By changing the system coordinates to $\tilde{\theta} = \hat{\theta} - \theta^*$ and $\tilde{\eta} = \eta - h \circ l(\theta^*)$, and changing the time scale to $\tau = \omega t$, (4.39) can be rewritten as

$$\begin{cases} \frac{d^q}{d\tau^q} \tilde{\theta} = \delta \bar{k} \zeta \\ \frac{d^q}{d\tau^q} \tilde{\zeta} = \delta\big(- \bar{\omega}_L \zeta + \bar{\omega}_L (h(x) - h \circ l(\theta^*) - \tilde{\eta}) a \sin(\tau)\big) \\ \frac{d^q}{d\tau^q} \tilde{\eta} = \delta\big(- \bar{\omega}_H \tilde{\eta} + \bar{\omega}_H (h(x) - h \circ l(\theta^*))\big), \end{cases} \tag{4.40}$$

where $k = \omega K = \omega \delta \bar{k}$, $\omega_h = \omega \omega_H = \omega \delta \bar{\omega}_H$, and $\omega_l = \omega \omega_L = \omega \delta \bar{\omega}_L$.

By substituting the equilibrium of the system, $x = l(\hat{\theta} + a \sin(\omega t))$, into (4.40), the “reduced FO-ESC system” will be obtained,

$$\begin{cases} \frac{d^q}{d\tau^q}\tilde{\theta}_r = \delta\bar{k}\zeta_r \\ \frac{d^q}{d\tau^q}\tilde{\zeta}_r = \delta\big(-\bar{\omega}_L\zeta_r + \bar{\omega}_L(\nu(\tilde{\theta}_r + a\sin(\tau)) - \tilde{\eta}_r)a\sin(\tau)\big) \\ \frac{d^q}{d\tau^q}\tilde{\eta}_r = \delta\big(-\bar{\omega}_H\tilde{\eta}_r + \bar{\omega}_H\nu(\tilde{\theta}_r + a\sin(\tau))\big), \end{cases} \tag{4.41}$$

where $(.)_r$ stands for reduced system, and $\nu(\tilde{\theta}_r + a\sin(\tau)) = h \circ l(\theta^* + \tilde{\theta}_r + a\sin(\tau)) - h \circ l(\theta^*)$. When $h \circ l(\theta^* + \tilde{\theta}_r + a\sin(\tau)) = h \circ l(\theta^*)$, system is working at its extremum point which means $\tilde{\theta}_r + a\sin(\tau) = 0$, and by assuming this point as the peak point of $f(x, u)$,

$$\begin{cases} \nu(0) = 0 \\ \nu'(0) = (h \circ l)'(\theta^*) = 0 \\ \nu''(0) = (h \circ l)''(\theta^*) < 0 \end{cases} \cdot \tag{4.42}$$

Writing the Taylor expansion for $\nu(\tilde{\theta}_r + a\sin(\tau))$ around the extremum point and by knowing that $\nu(0) = \nu'(0) = 0$ in the neighborhood of this point,

$$\nu(\tilde{\theta}_r + a\sin(\tau)) = \frac{\nu''(0)}{2!}(\tilde{\theta}_r + a\sin(\tau))^2 + \frac{\nu'''(0)}{3!}(\tilde{\theta}_r + a\sin(\tau))^3 + H.O.T, \tag{4.43}$$

where $H.O.T$ is negligible since $\tilde{\theta}_r + a\sin(\tau)$ is small.

To simplify the stability analysis of FO-ESC, (4.41) can be approximated by its averaged model. The averaged model of (4.41) will be

$$\begin{cases} \frac{d^q}{d\tau^q}\tilde{\theta}^a_r = \delta\bar{k}\zeta^a_r \\ \frac{d^q}{d\tau^q}\tilde{\zeta}^a_r = \delta\big(-\bar{\omega}_L\zeta^a_r + \frac{a\bar{\omega}_L}{2\pi}\int_0^{2\pi}\nu(\tilde{\theta}^a_r + a\sin(\sigma))\sin(\sigma)d\sigma\big) \\ \frac{d^q}{d\tau^q}\tilde{\eta}^a_r = \delta\big(-\bar{\omega}_H\tilde{\eta}^a_r + \frac{\bar{\omega}_H}{2\pi}\int_0^{2\pi}\nu(\tilde{\theta}^a_r + a\sin(\sigma))d\sigma\big) \end{cases} \cdot \tag{4.44}$$

Assume $(\theta_r^{\tilde{a},e}, \zeta_r^{a,e}, \tilde{\eta}_r^{a,e})$ is the equilibrium point of the averaged system, then at this point system has no dynamics and $\frac{d^q}{dt^q}\tilde{\theta}_r^a = 0$, $\frac{d^q}{dt^q}\tilde{\zeta}_r^a = 0$ and $\frac{d^q}{dt^q}\tilde{\eta}_r^a = 0$ gives,

$$\begin{cases} \zeta_r^{a,e} = 0 \\ \zeta_r^{a,e} = \frac{1}{2\pi}\int_0^{2\pi} \nu(\tilde{\theta}_r^{a,e} + a\sin(\sigma))\sin(\sigma)d\sigma \\ \eta_r^{a,e} = \frac{1}{2\pi}\int_0^{2\pi} \nu(\tilde{\theta}_r^{a,e} + a\sin(\sigma))d\sigma \end{cases} \cdot \tag{4.45}$$

Since $\zeta_r^{a,e} = 0$,

$$\frac{1}{2\pi}\int_0^{2\pi} \nu(\tilde{\theta}_r^{a,e} + a\sin(\sigma))\sin(\sigma)d\sigma = 0. \tag{4.46}$$

One nominee for $\theta_r^{\tilde{a},e}$ can be a linear polynomial in the form of $\theta_r^{\tilde{a},e} = \sum_{i=1}^{2} b_i a^i + O(a^3)$. By substituting $\theta_r^{\tilde{a},e}$ into (4.43) and substitute the result in (4.46) and equating the like powers of a, $\nu''(0)b_1 = 0$ and $\nu''(0)b_2 + \frac{1}{8}\nu'''(0) = 0$, which means,

$$\begin{aligned} \theta_r^{\tilde{a},e} &= -\frac{\nu'''(0)}{8\nu''(0)}a^2 + O(a^3) \\ \eta_r^{\tilde{a},e} &= \frac{\nu''(0)}{4}a^2 + O(a^3). \end{aligned} \tag{4.47}$$

Therefore, the equilibrium of averaged system, (4.44), is

$$\begin{cases} \theta_r^{a,e} = -\frac{\nu'''(0)}{8\nu''(0)} + O(a^3) \\ \zeta_r^{a,e} = 0 \\ \eta_r^{a,e} = \frac{a^2\nu''(0)}{4} + O(a^3). \end{cases} \tag{4.48}$$

To linearized this system, the Jacobean of (4.44) around the equilibrium point, (4.48), is obtained,

$$J_r^a = \delta \begin{bmatrix} 0 & \bar{k} & 0 \\ \frac{a\bar{\omega}_L}{2\pi}\int_0^{2\pi} \nu'(\hat{\theta}_r^{a,e} + a\sin(\sigma))\sin(\sigma)d\sigma & -\bar{\omega}_L & 0 \\ \frac{\bar{\omega}_H}{2\pi}\int_0^{2\pi} \nu'(\hat{\theta}_r^{a,e} + a\sin(\sigma))d\sigma & 0 & -\bar{\omega}_H \end{bmatrix}. \tag{4.49}$$

The eigenvalues of J_r^a are the roots of the characteristic polynomial, $det(\lambda_i I - J_r^a) = 0$,

$$det(\lambda_i I - J_r^a) = (\lambda + \delta\bar{\omega}_H)\Big(\lambda^2 + \delta\bar{\omega}_L\lambda - \frac{a\delta^2\bar{\omega}_L\bar{k}}{2\pi}\int_0^{2\pi} \nu'(\theta_r^{\tilde{a},r} + a\sin(\sigma))\sin(\sigma)d\sigma\Big). \tag{4.50}$$

To calculate the second term of (4.50), the Taylor expansion of ν is substituted and the integral has been calculated,

$$\int_0^{2\pi} \nu'(\theta_r^{\tilde{a},r} + a\sin(\sigma))\sin(\sigma)d\sigma = \pi\nu''(0)a + O(a^2). \tag{4.51}$$

Consequently, characteristic polynomial of linearized averaged model of FO-ESC is

$$det(\lambda_i I - J_r^a) = (\lambda + \delta\bar{\omega}_H)\Big(\lambda^2 + \delta\bar{\omega}_L\lambda - \frac{a^2\delta^2\bar{\omega}_L\bar{k}}{2}\nu''(0) + O(\delta^2 a^3)\Big), \tag{4.52}$$

and the eigenvalues are $\lambda_1 = -\delta\bar{\omega}_H$ and,

$$\lambda_{2,3} = \frac{-\delta\bar{\omega}_L \pm \sqrt{\delta^2\bar{\omega}_L^2 + 2\delta^2\bar{\omega}_L\bar{k}\nu''(0)a^2 - O(a^3\delta^2)}}{2}. \tag{4.53}$$

The eigenvalues of J_r^a are stable for sufficiently small a, therefore the linearized averaged model FO-ESC is stable under this condition.

Another important conclusion can be drawn from this linearization. Since in the design of ESC algorithm, usually $\bar{\omega}_L$ is picked to be small [103], and as can be seen in (4.53), the real parts of eigenvalues are directly related to $\bar{\omega}_L$, therefore the eigenvalues of the ESC system can be close to the imaginary axis if $q = 1$ which means the integer order ESC can potentially have slowly damped poles in its system. However, these eigenvalues are not close to the stability boundary of fractional order system ($\arg(\lambda) > \frac{q\pi}{2}$) and consequently, they can be damped faster than their equivalent integer order system.

4.6.1 Simulation Results

In this section, the performance of IO-ESC and FO-ESC are compared using Simulink. In the simulations, the output of ESC block is used as a reference voltage for the next stage converter (inverter). Generally, converter (inverter) dynamics are faster than ESC dynamics and therefore the converter (inverter) seems as a static gain to ESC, $\nu = V_{inv}(1-d)$, as shown in Fig. 4.23.

In the following simulations the performance of proposed FO-ESC and IO-ESC are compared under sun irradiation variations. Temperature is assumed to be constant at $T = 25^oC$.

In the first set of simulations, sun irradiation profile varies according to Fig. 4.24. Based on this profile, PV array has an irradiation of $1000W/m^2$ for $4s$ and then the irradiation ramps down to $400W/m^2$ in $2s$ and stays there for $3s$ and lastly jumps up to $1000W/m^2$ and stays there for $1s$. This profile shows the step-like and ramp-like response of FO-ESC and IO-ESC.

Also to have a fair comparison between FO-ESC and IO-ESC, all other parameters, like perturbation frequency, $f = 100rad/s$, cut-off frequency of high-pass filter, $\omega_h = 500rad/s$, and gain of integrator, $k = 150$, are considered to be the same for both FO-ESC and IO-ESC schemes. Under these conditions, the behavior of these schemes have been illustrated in Fig. 4.25. Simulation results show that FO-ESC converges to the peak point faster than the IO-ESC. Also as seen in Fig. 4.25 and Fig. 4.26, the perturbation amplitude on the IO-ESC signal is higher than the perturbation amplitude on FO-ESC as expected.

To do further investigation regarding the role of the order of fractional order integrator in the FO-ESC scheme, the step response of FO-ESC with different integrator order had been depicted in Fig. 4.27. In this simulation, the order of integrator varies in the range of 0.88 to 0.97 and as can be seen in the simulation results, as long as the system is in the

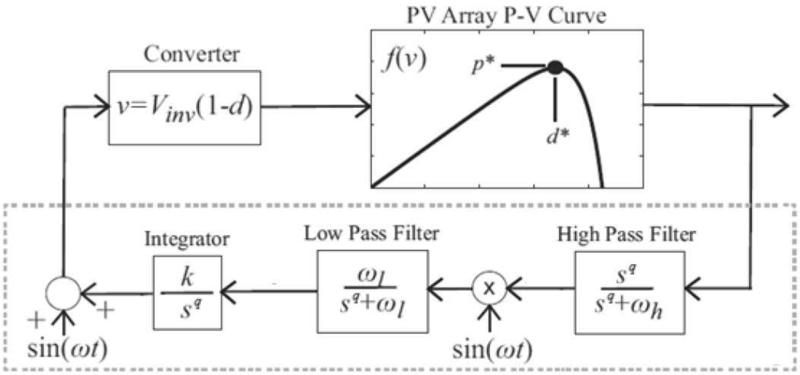

Fig. 4.23: FO-ESC scheme series with converter.

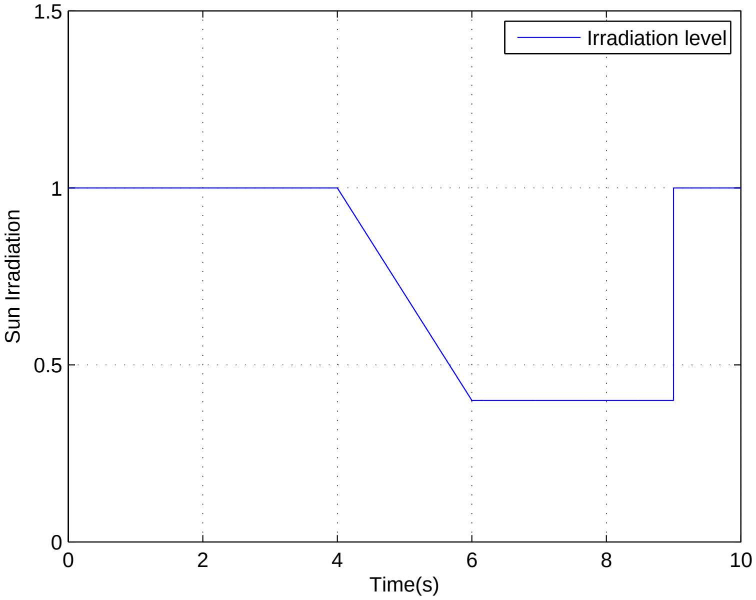

Fig. 4.24: Sun irradiation pattern.

stable region, by decreasing the order of FO-ESC, the system converges faster to the peak point.

4.6.2 Grid-Connected Simulations

In this section, a grid-connected PV system has been considered and three MPPT algorithms include IO-ESC, IC and FO-ESC are applied to this system. This simulation has been done using Simulink/MATLAB as shown in Fig. 4.28.

Figures 4.29 and 4.30 present the simulation results of three MPPT algorithms. As seen in these figures, FO-ESC outperforms the other two algorithms. FO-ESC not only converges faster than the other two schemes but also tracks the maximum power point smoothly.

In addition, the three-phase inverter output is shown in Fig. 4.31. Total harmonic distortion (THD) of injected current to the grid has been compared in Table 4.2.

As seen in this table, IO-ESC increases the convergence speed compare to IC but creates more harmonic distortion in the output current. On the other hand, FO-ESC not only reduces the THD of injected current and peak voltage of DC-link capacitor but also increases the convergence speed compared to IC and IO-ESC.

4.6.3 Experimental Results

For experimental results, a fractional horsepower dynamometer is used to model the PV panel. The dynamometer includes a DC motor and a hysteresis brake. The DC motor in dynamometer can be approximated by

$$G_m(s) = \frac{1.52}{1.01s + 1}. \tag{4.54}$$

As the brake has nonlinear behavior, the PV can be adopted as a model for the hysteresis brake. In other words, the hysteresis brake acts as a PV array. The proposed scheme can be seen in Fig. 4.32. As can be seen in Fig. 4.33, the Magtrol hysteresis brake used in the dynamometer produces torque strictly through an air gap, without the use of magnetic

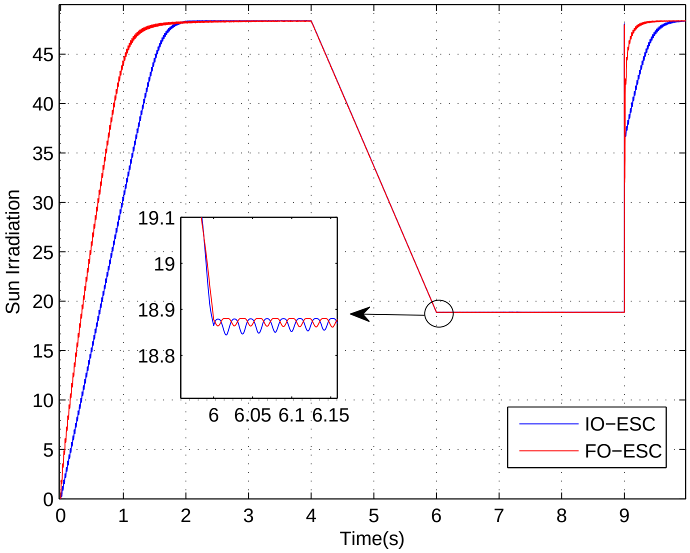

Fig. 4.25: Comparison of FO-ESC and IO-ESC in the time domain.

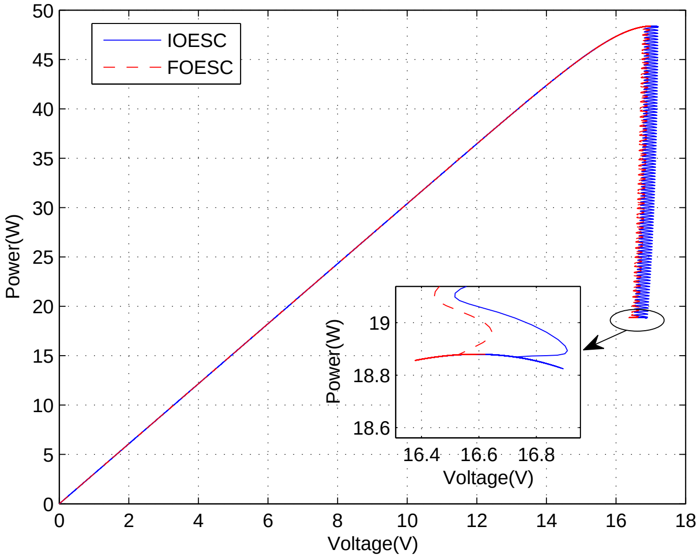

Fig. 4.26: Comparison of P-V chart of FO-ESC and IO-ESC.

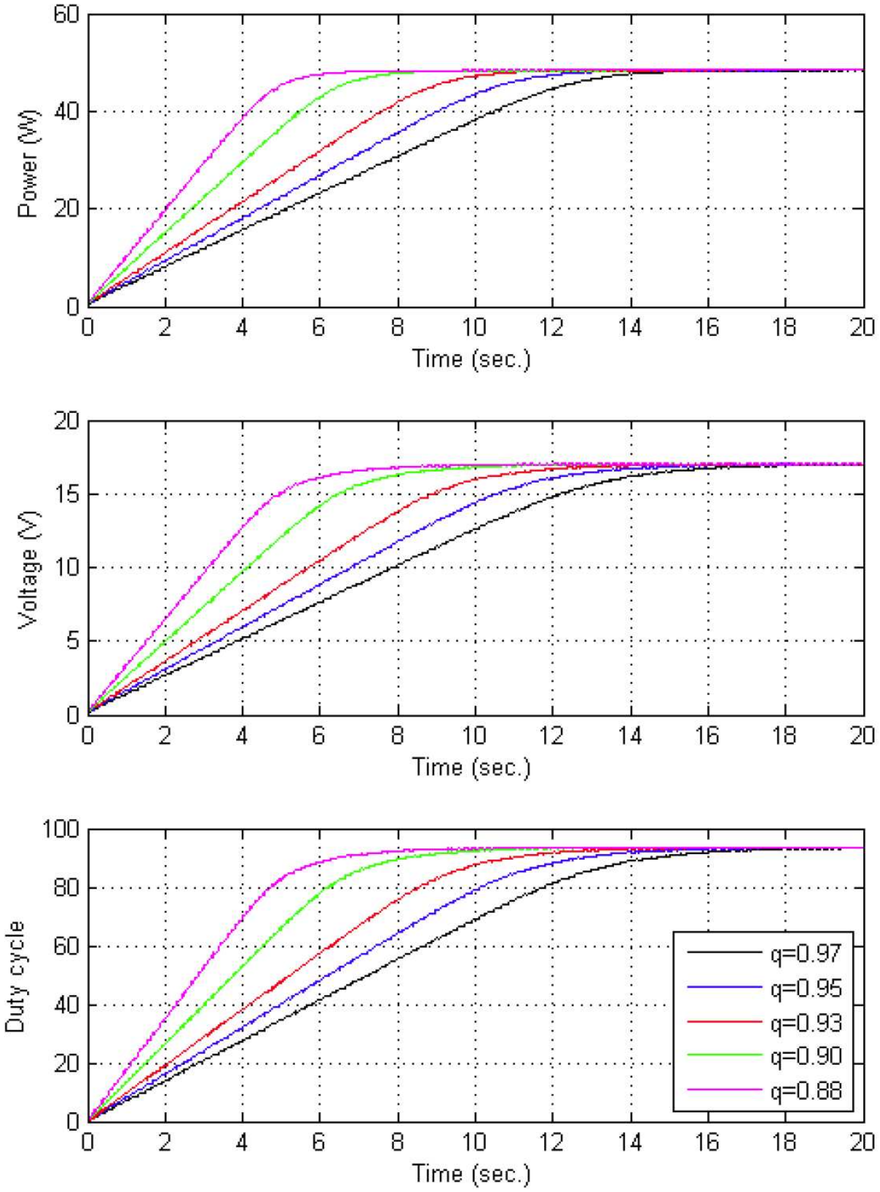

Fig. 4.27: Comparison of FO-ESC scheme with different fractionality order in integrator.

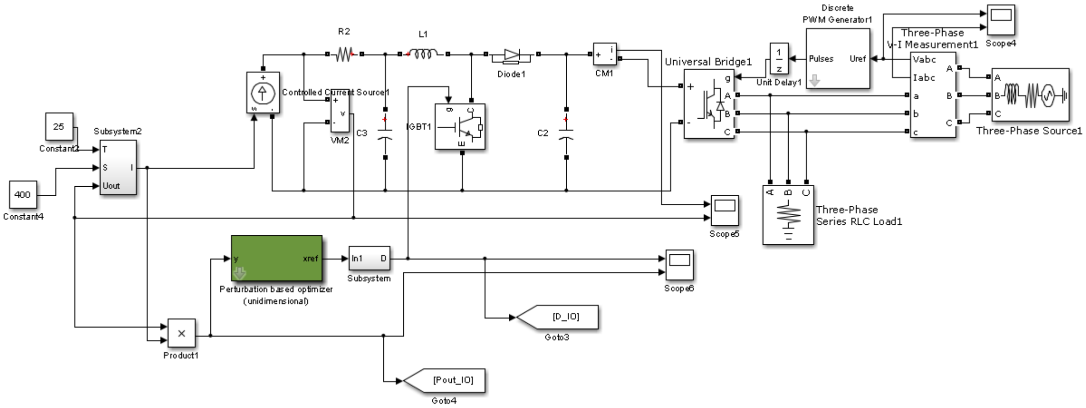

Fig. 4.28: Simulation of grid-connected PV system with MPPT.

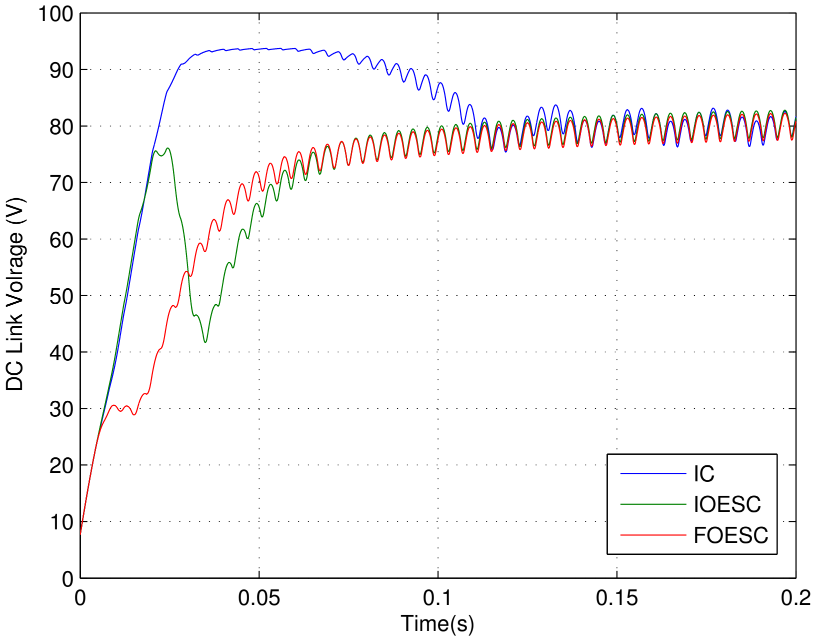

Fig. 4.29: DC link voltage in the grid-connected PV system using IC, IO-ESC, and FO-ESC MPPTs.

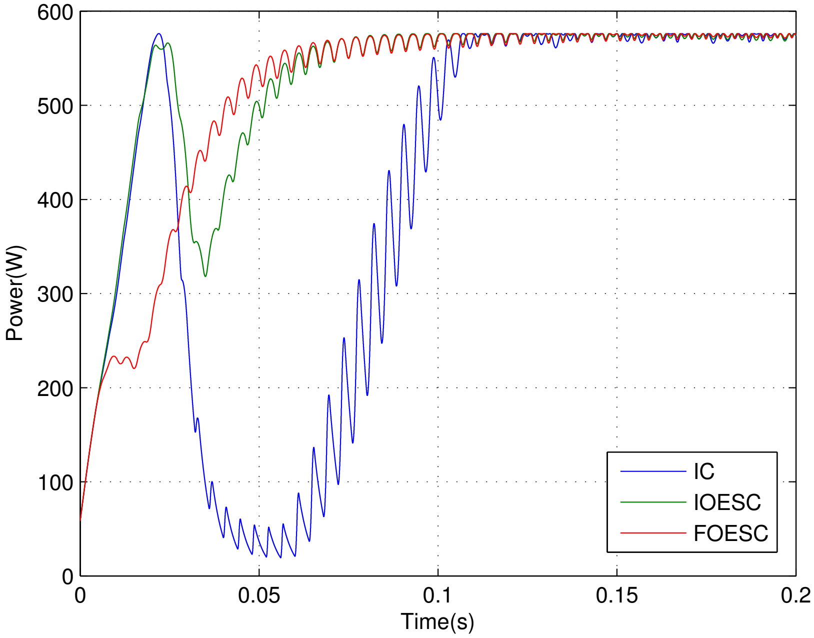

Fig. 4.30: Output power in the grid-connected PV system using IC, IO-ESC, and FO-ESC MPPTs.

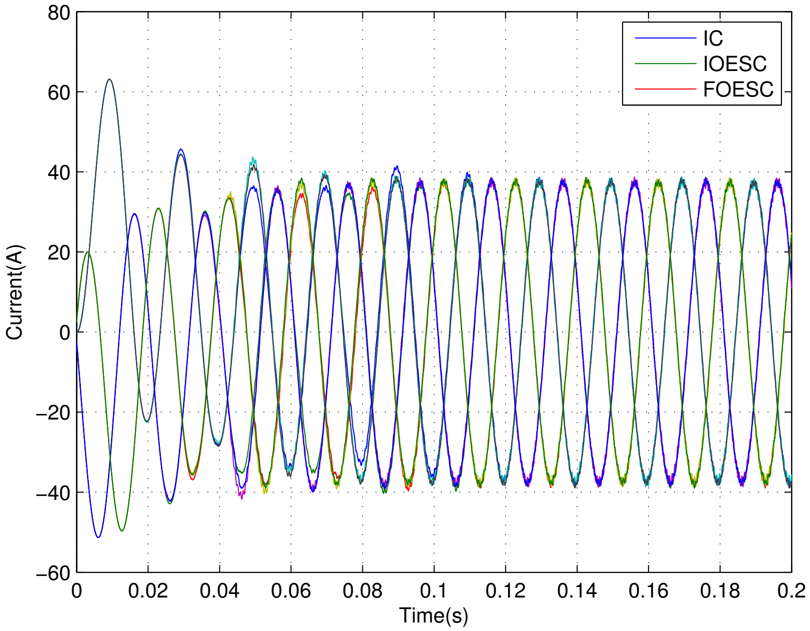

Fig. 4.31: Output current in the grid-connected PV system using IC, IO-ESC, and FO-ESC MPPTs.

Table 4.2: Total harmonic distortion of injected current to the grid.

IC	IO-ESC	FO-ESC
1.8%	3.3%	1.8%

particles or friction components. This method of breaking provides far superior characteristics (smoother torque, longer life, superior repeatability, higher degree of controllability, and less maintenance and down time). The brake and the motor are each driven by an advanced motion controls brush type PWM servo amplifier Model 50A8. These controllers receive analog signals from data acquisition hardware. The PWM controllers use these signals to set the voltage output to the motor or the brake. The controller then supplies all the current needed to maintain the set voltage level [104].

The extremum seeking control scheme is tested using MATLAB/Simulink environment, which uses the WinCon application from Quanser, to communicate with the Quanser MultiQ3 data acquisition card. WinCon is a Windows-based application that runs Simulink models in real-time on PCs. This brings rapid prototyping and hardware-in-the-loop simulation capabilities to Simulink models. The MATLAB Real-Time Workshop generates C code from the Simulink model, which results in a Windows executable file that is run by WinCon independently of Simulink. WinCon architecture ensures that the real-time process is afforded the highest CPU priority and is not preempted by any competing tasks other than the core OS functions. The Simulink model used for the experiments is shown in Fig. 4.34. This figure shows the hardware-in-the-loop real time simulation model for integer order and fractional order extremum seeking scheme, respectively. Simulink automatically generates codes for Windows target to drive the dynamometer and brake via D/A blocks.

The experiments have been done to support the numerical simulation results. As can be seen in the experimental results, these results are consistent with the numerical results that have been achieved in simulations. From Fig. 4.35, it can be noticed that the convergence speed of FO-ESC is better than the IO-ESC which admits the results achieved from numerical simulation. In addition Fig. 4.35 illustrates that the reduction in the order

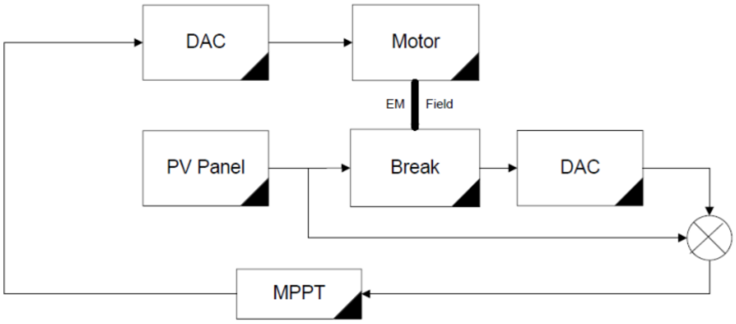

Fig. 4.32: Modeling PV behavior using fractional horsepower dynamometer.

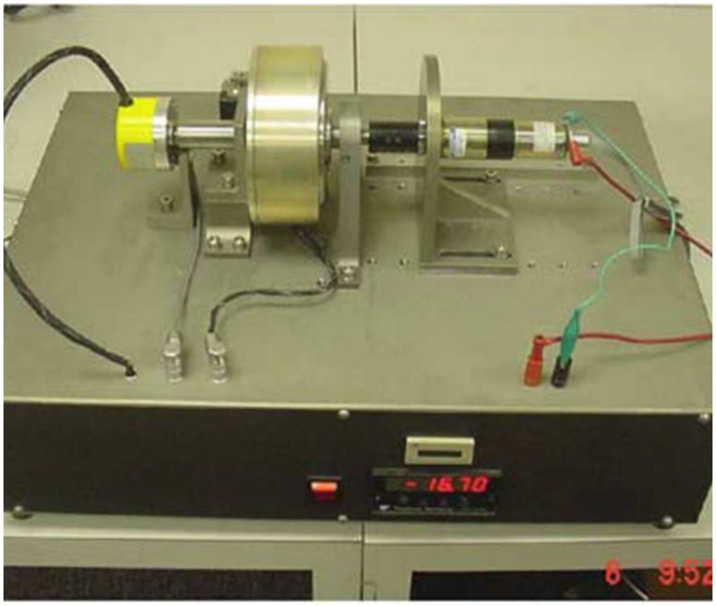

Fig. 4.33: The fractional horsepower dynamometer developed at CSOIS.

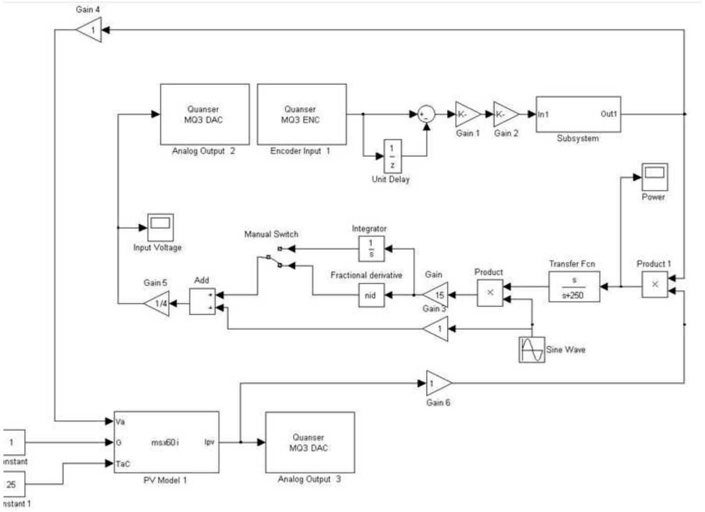

Fig. 4.34: Simulink model used in the FO-ESC real-time experiments using RTW windows target.

of fractional order integrator can improve the convergence speed of FO-ESC.

4.6.4 Summary

In this chapter, the importance of maximum power point trackers in the PV systems has been discussed. The structure of ESC MPPT, as the outperformed MPPT among all other MPPT algorithms was presented. By introducing Bode's ideal cut-off filter (BICO), this filter is applied to the structure of ESC and the advantages of using this filter were analyzed. This topic was followed by introducing FO-ESC and comparing its performance with IO-ESC in the grid-connected systems. lastly, the stability conditions of FO-ESC were presented.

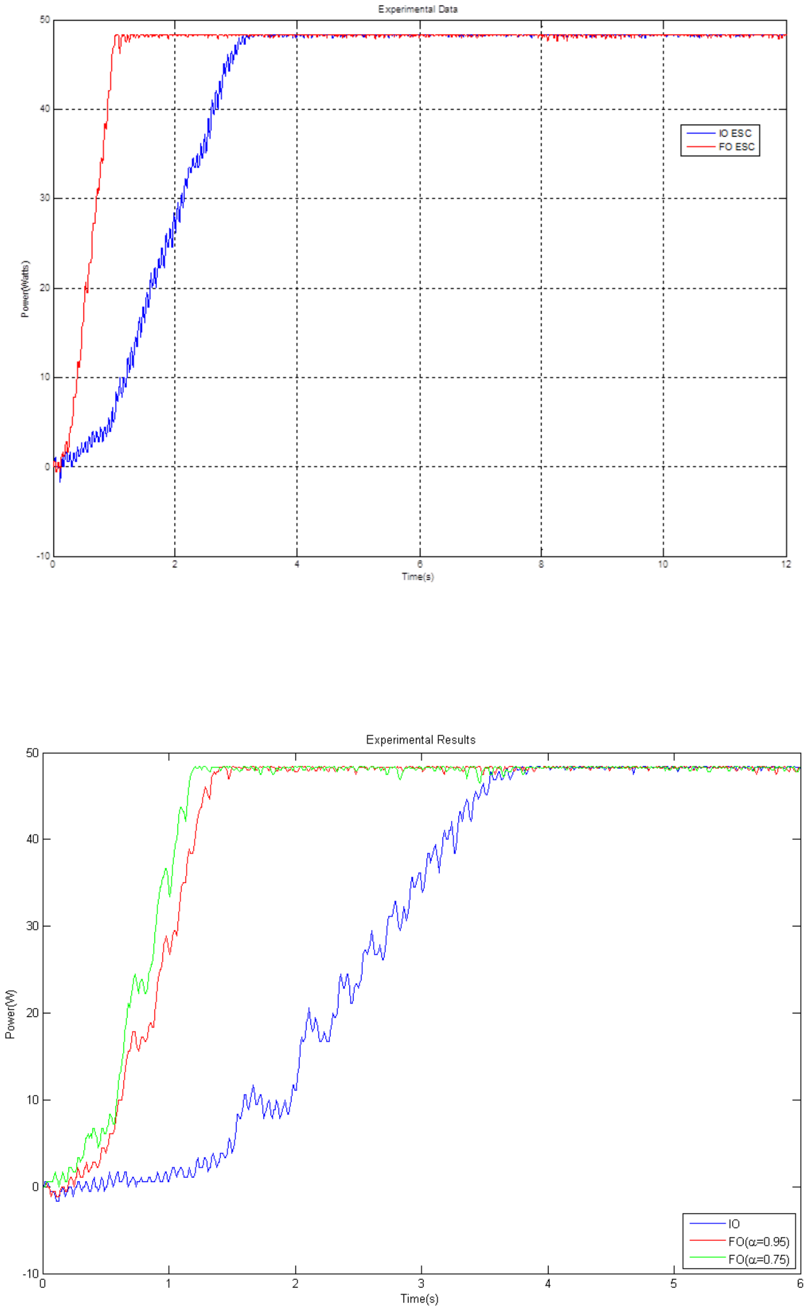

Fig. 4.35: Convergence of PV output power to peak point by applying different integration orders in IO-ESC and FO-ESC.

Chapter 5

Voltage and Current Control of Three-Phase Grid-Connected Inverter Using Fractional Order Controllers

5.1 Introduction

The control methodology in the grid-connected inverter is a classical control problem, which contains an inner current control loop and an outer voltage control loop. In this control strategy, voltage loop maintains a constant voltage on the DC link capacitor and provides the reference for the inner current control loop. Also, a grid synchronization method (in this work PLL) is used in order to synchronize the control system with the phase angle of the grid.

The system which will be investigated in this work is a single-stage three-phase grid-connected PV system as shown in Fig. 5.1.

There has been some debates in literature regarding the performance and pros and cons of different control strategies such as model predictive, hysteresis, synchronous, or stationary frame PI, etc. However, as discussed in the first chapter, synchronous frame PI is still commonly used in many applications because of its relative simplicity, creating less distortion in the output current, constant frequency, etc.

Synchronous frame PI controller operates by transforming the three-phase AC current, $[i_a, i_b, i_c]$, in the stationary frame into the DC components, $[I_d, I_q]$, in the synchronous rotating frame. This will allow the associated PI steady state error in the AC applications to be eliminated and also provides independent control of injected active and reactive power into the grid [105].

In the synchronous frame, the d and q components of inverter output current are regulated using two PI regulators, and the third PI controller maintains the DC link capacitor

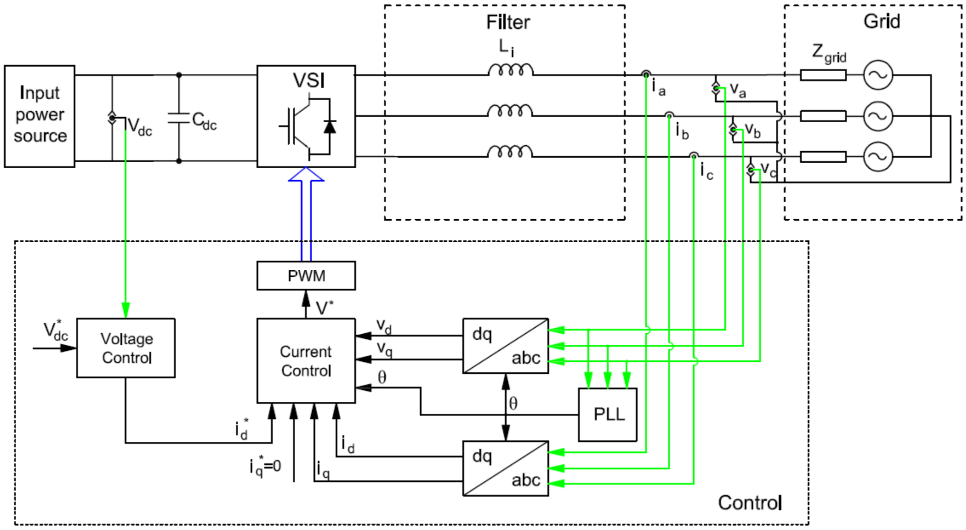

Fig. 5.1: Control scheme of a three-phase grid-connected VSI.

voltage in the voltage control loop. In fact, voltage control loop provides a set-point for inner current control loop. The time constant of voltage control loop is designed to be significantly longer than the time constant of inner current control loops, to decouple the design processes of voltage and current control loops. Figure 5.2 illustrates the control strategy of synchronous frame.

5.2 Mathematical Model of Three-Phase Grid-Connected PV System

As discussed in Chapter 3, in most cases, VSI switching frequency is significantly higher than the control loop bandwidth and will have negligible impact on the inverter control loop dynamics. Therefore, the inverter can be modeled as a constant gain with no dynamics. However, other components of the system (e.g. DC link capacitor and filter) have significant influence on the control loop response and must be considered in the modeling of the system.

5.2.1 Modeling of Current Control Loop

The current controller is the inner control loop of the three-phase grid-connected PV

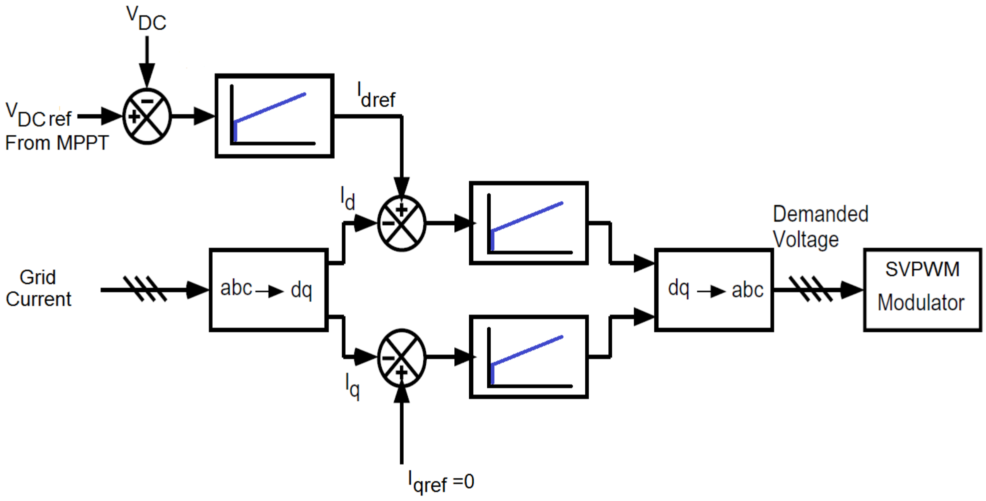

Fig. 5.2: Control strategy of synchronous frame.

system. As mentioned before, in the system there are two current controllers for direct, I_d, and quadrature, I_q, components of inverter output current.

The current control loop for both direct and quadrature current components can be modeled as shown in Fig. 5.3.

Different blocks in this model can be defined as follows:

- G_{DCAC} represents the time delay caused by the inverter to do the time averaging over one switching period. As mentioned before, since the switching frequency of the inverter is significantly higher than the control loop bandwidth, the dynamics of the

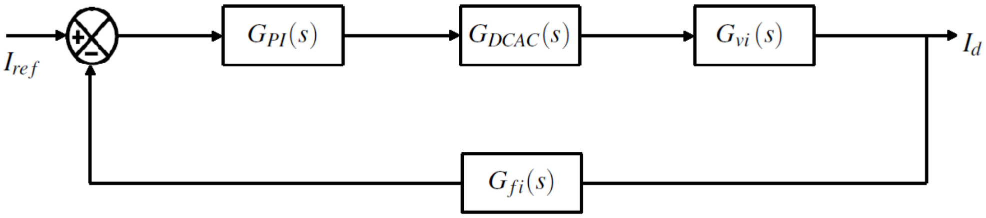

Fig. 5.3: Current control loop schematic.

inverter are negligible and G_{DCAC} can be considered as a constant gain.

- G_{fi} is the measurement noise filter transfer function. Typically, in order to reduce the measurement noises, a first order filter is employed.
- G_{PI} represents the controller transfer function.
- G_{vi} represents the transfer function of the inverter output filter and describes how the inverter output current reacts to the variations of inverter voltage.

As discussed before, the d and q axes of the currents are not independent, therefore, these two current components need to be decoupled to simplify the model.

The transfer function of inverter and its output filter has been derived in Chapter 4,

$$G_{vi}(s) = \frac{1}{Ls + R}. \tag{5.1}$$

By adding all the filtering delays in the current control loop of Fig. 5.3, the control loop can be simplified as shown in Fig. 5.4. In this new schematic, $G_{sum}(s) = G_{DCAC}(s)G_{fi}(s)$.

Typically, the sum of these delays is approximately larger than the sampling time, T_s, and therefore the design procedure can be done in continuous domain.

Therefore, the continuous open-loop transfer function of the current control loop becomes

$$G_P(s) = G_{sum}G_{iivi} = \frac{Ke^{-T_d s}}{Ls + R}. \tag{5.2}$$

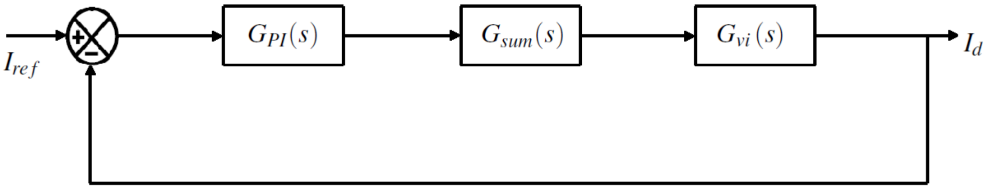

Fig. 5.4: Simplified current control loop schematic.

5.2.2 Modeling of Voltage Control Loop

Voltage controller is the outer control loop of the grid-connected PV system. As mentioned before, this controller creates the reference for the d axis of the current control loop. This control loop can be modeled as shown in Fig. 5.5.

In this model:

- G_{fv} represents the measurement noise filter,
- G_{PI} represents the controller transfer function,
- M_{id} represents the controlled current-loop transfer function,
- G_{DC} represents the transfer function between the direct component of current and the DC link voltage.

Applying fractional order controllers to the current control loop, makes the M_{id} to be fractional order transfer function. To simplify the tuning of voltage regulators, M_{id} can be approximated with a reduced order fractional order pole or first order pole plus delay.

Reduced Order Closed-Loop FO-PI Current Controller Transfer Function

In the case of FO-PI, ($k_p(1 + k_i/s^{\alpha})$), the closed-loop transfer function for the current control loop will be

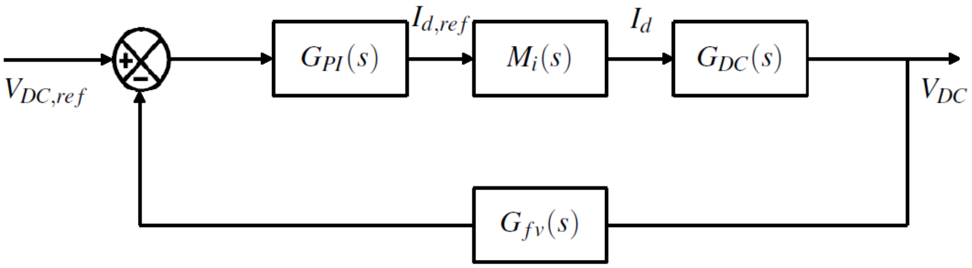

Fig. 5.5: Voltage control loop schematic.

$$M_{id} = \frac{K(k_p s^\alpha + k_p k_i)}{Ls^{\alpha+1} + (R + k_p k_i)s^\alpha + K k_p k_i}, \tag{5.3}$$

or

$$M_{id} = \frac{\frac{1}{k_i}s^\alpha + 1}{\frac{L}{Kk_pk_i}s^{\alpha+1} + \frac{R+k_pk_i}{Kk_pk_i}s^\alpha + 1}. \tag{5.4}$$

Since in the high frequencies $s^\alpha/ki >> 1$ and $Ls^{\alpha+1}/Kk_pk_i+(R+k_pk_i)s^\alpha/Kk_pk_i >> 1$, then M_{id} can be rewritten as

$$M_{id} = \frac{Kk_p}{Ls + R + Kk_p}. \tag{5.5}$$

The Bode plots of reduced order and original transfer function which have been depicted in Fig. 5.6 shows the similarity between the frequency response of these two systems.

Reduced Order Closed-Loop FO-[PI] Current Controller Transfer Function

In the case of FO-[PI], $((k_p + k_i/s)^\alpha)$, the closed-loop transfer function for the current control loop is

$$M_{id} = \frac{K(k_p s + k_i)^\alpha}{Ls^{\alpha+1} + Rs^\alpha + K(k_p s + k_i)^\alpha}. \tag{5.6}$$

As will be shown later, in the tuned FO-[PI], $k_i >> k_p$, therefore the zero of M_{id} is close to the imaginary axis and can not be neglected. M_{id} can be rewritten as

$$M_{id} = \frac{K(\frac{k_p}{k_i}s + 1)^\alpha}{\frac{L}{k_i^\alpha}s^{\alpha+1} + \frac{R}{k_i^\alpha}s^\alpha + K(\frac{k_p}{k_i}s + 1)^\alpha}. \tag{5.7}$$

Since in higher frequencies, $\frac{k_p}{k_i}s >> 1$, then $\frac{k_p}{k_i}s + 1 \simeq \frac{k_p}{k_i}s$ and therefore,

$$M_{id} = \frac{Kk_p^\alpha}{Ls + R + Kk_p^\alpha}. \tag{5.8}$$

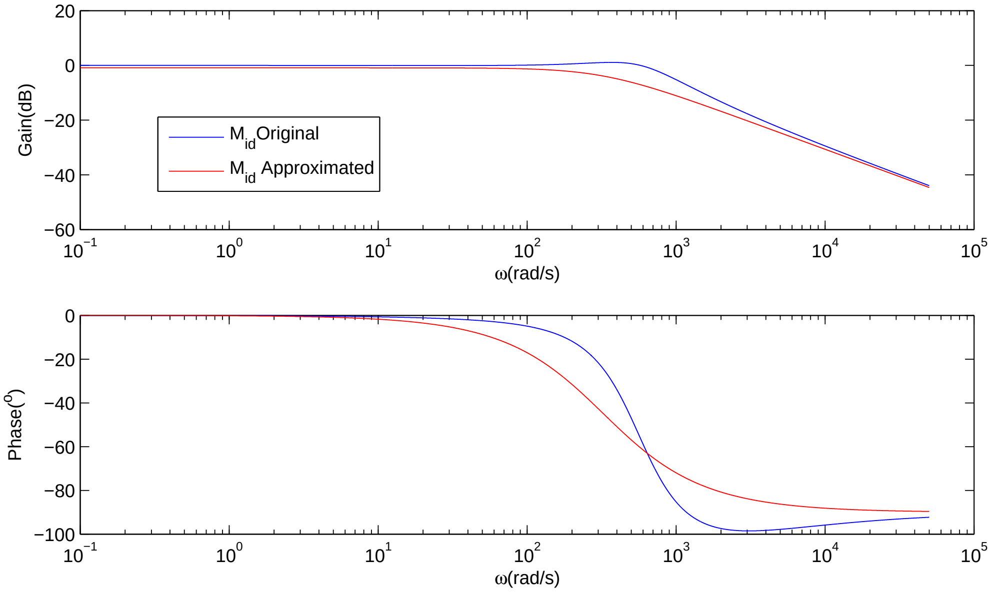

Fig. 5.6: Comparison between frequency responses of reduced order and original closed-loop voltage control transfer function using FO-PI.

The Bode plots of reduced order and original transfer function which have been depicted in Fig. 5.7 show the similarity between the frequency responses of these two systems.

Reduced Order Closed-Loop IO-PI Current Controller Transfer Function

IO-PI current controller can be considered as a special case of FO-[PI] with $\alpha = 1$, then

$$M_{id} = \frac{Kk_p}{Ls + R + Kk_p}. \tag{5.9}$$

Reduced Order Voltage Loop Transfer Function

After calculating the transfer function of controlled current loop, the transfer function for voltage control loop, which is the ratio between I_d and v_{dc} will be

$$G_{DC} = -\frac{K_{dc}}{Cs} M_{id}, \tag{5.10}$$

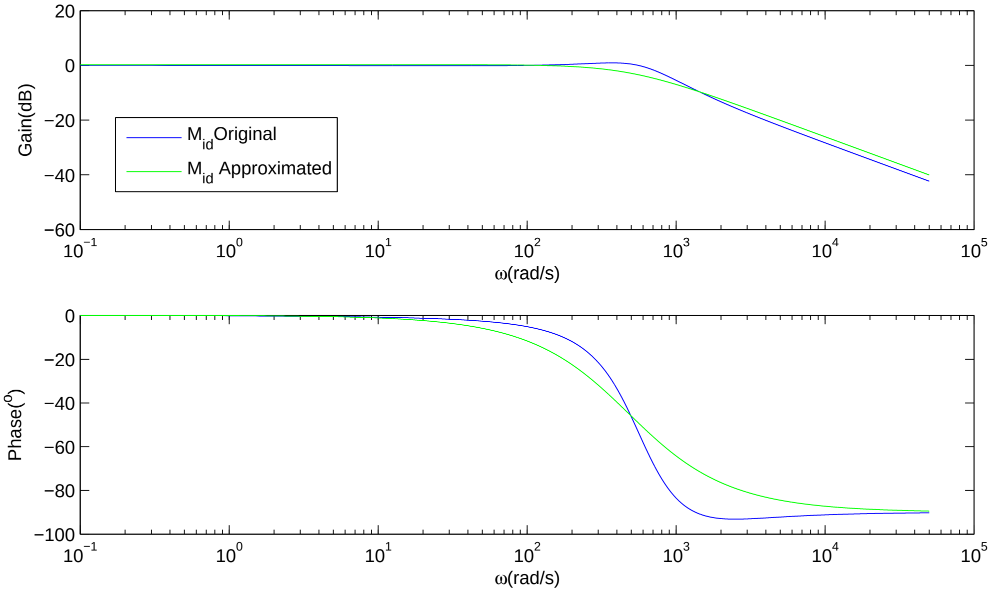

Fig. 5.7: Comparison between frequency responses of reduced order and original closed-loop voltage control transfer function using FO-[PI].

where K_{dc} is a constant that represents the ratio between direct component of injected current to the DC current. This ratio can be obtained by considering the relationship between the input and output power of the system which is

$$\upsilon_{dc} I_{dc} = \frac{3}{2} V_d I_d, \tag{5.11}$$

and

$$\upsilon_{ab} = \frac{\sqrt{3}}{2\sqrt{2}} \upsilon_{dc} m, \tag{5.12}$$

where m is the modulation index and υ_{ab} is the voltage between two phases. The direct component of phase voltage, υ_{ab}, is obtained by

$$\upsilon_d = \frac{\sqrt{2}}{\sqrt{3}} \upsilon_{ab} = \frac{1}{2} \upsilon_{dc} m. \tag{5.13}$$

Therefore, K_{dc} can be calculated by combining (5.11) and (5.13),

$$K_{dc} = \frac{I_{dc}}{I_d} = \frac{3}{2}\frac{\upsilon_d}{\upsilon_{dc}} = \frac{3}{4}m. \tag{5.14}$$

Since SVM has been employed to drive the inverter, $0 \leq m \leq \frac{2}{\sqrt{3}}$. In the case of using SVPWM, $m = \frac{\sqrt{3}}{2}$ and therefore, the general form of continuous open loop transfer function of the voltage control loop will be

$$G_P(s) = \frac{K_{dc}e^{-T_d s}}{Cs(Ts+1)}. \tag{5.15}$$

5.2.3 Complete Control Scheme of the Three-Phase Grid-Connected PV System

An overview of the total control scheme of a three-phase grid-connected PV system is shown in Fig. 5.8. As can be seen in this figure, the voltage and current of the grid and inverter is decoupled using $\alpha\beta$ and then transferred to a synchronous frame using a dq transformation. The direct and quadrature components of current and voltage are delivered to the current and voltage controllers. Outputs of these controllers are converted back to the *abc* coordination and applied to the SVM driver to create the command for the inverter.

5.3 Simulations Results

Simulations of the benchmarked three-phase grid-connected PV system are done in PLECS/Simulink, which is a power electronic toolbox based on MATLAB platform. The general scheme of the simulation is presented in Fig. 5.9. As can be seen in this figure, the voltage set-point for voltage control loop is made through a MPPT. The direct current component, I_d, is made by outer voltage control loop and the quadrature current component, I_q, is forced to be zero to minimize the injected reactive power to the grid. The SVM has been implemented to drive the three-phase VSI switches. The sub-blocks of the control and power electronics schemes of the grid-connected system are presented in Fig. 5.10 and Fig. 5.11, respectively.

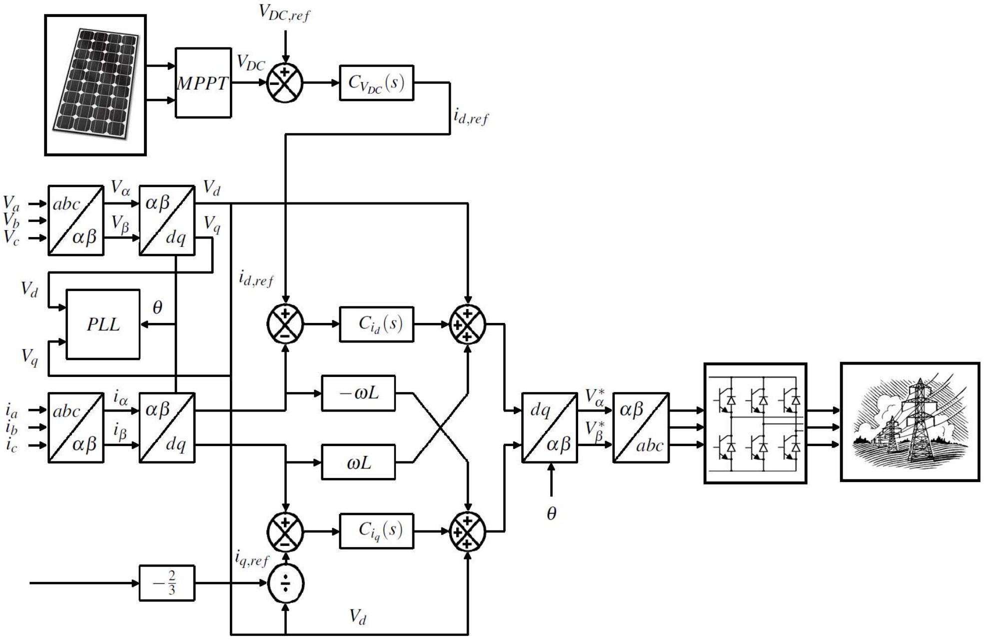

Fig. 5.8: Voltage and current control loops schematic.

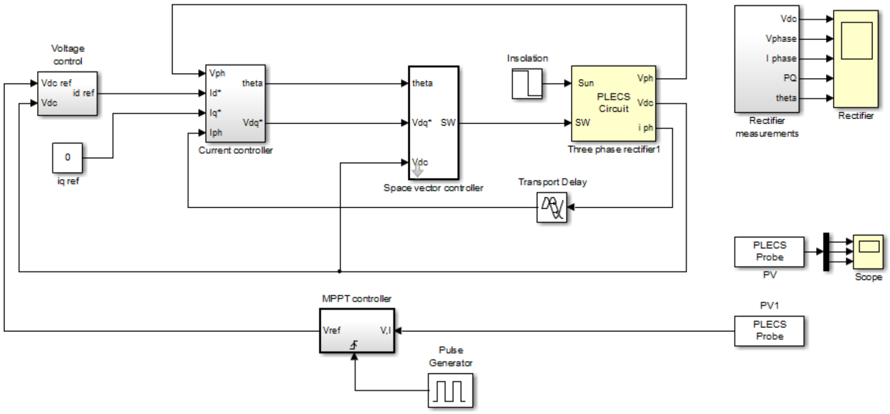

Fig. 5.9: Simulation of voltage and current control loops in MATLAB/Simulink.

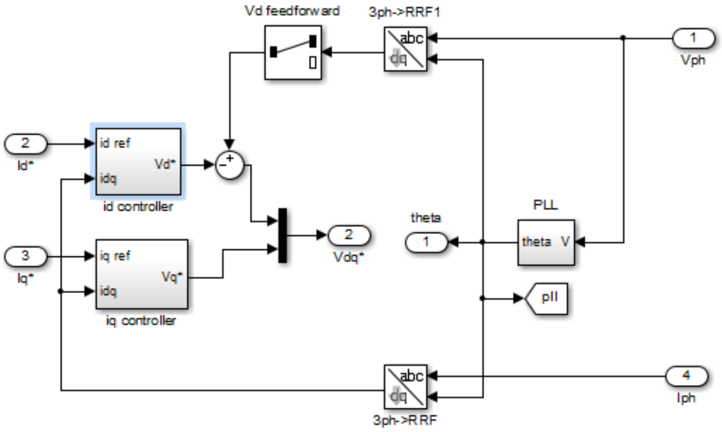

Fig. 5.10: Simulation of current control loop in MATLAB/Simulink.

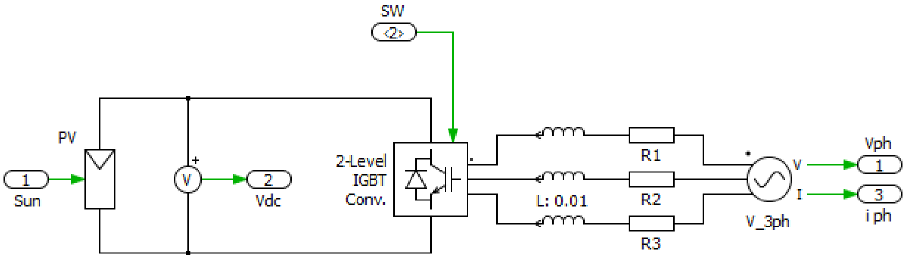

Fig. 5.11: Simulation of a two-level three-phase grid-connected PV system.

5.3.1 Design Criteria

To design the current and voltage controllers in the frequency domain, the cross-over frequency and phase margin need to be defined initially. The optimal cross-over frequency and phase margin to control a grid-connected PV system have been determined in Liu et al. work [106]. According to this research, for the current control loop in a grid-connected PV system application, the optimal range of natural frequency is $\omega_n \in [160, 990] rad/s$. Under this condition, the stability of this system is guaranteed. This optimal range for the voltage control loop is $\omega_n \in [20, 120] rad/s$.

To maintain 5% overshoot in the time response of the system, the damping ratio is considered to be $\zeta = 0.707$. Since the relationship between ζ, ω_n and ω_c is

$$\frac{\omega_c}{\omega_n} = \sqrt{-2\zeta^2 + \sqrt{1 + 4\zeta^4}}, \tag{5.16}$$

then cross-over frequency of the current control loop and voltage control loop will be in the range of $[100, 640] rad/s$ and $[10, 80] rad/s$, respectively.

In the following, the cross-over frequency of the current control loop is chosen to be $\omega_c = 600 rad/s$ and this value for the voltage control loop is desired to be $\omega_c = 15 rad/s$. According to Fig. 5.12, to have a damping ratio of $\zeta = 0.707$, the phase margin needs to be $\Phi M = \frac{\pi}{3}$.

5.3.2 System Design

Power-Electronics Design of the Three-Phase Grid-Connected PV System

In the following simulations, the PV array consists of 35 parallel cells and four parallel strings, each with ten BP365 modules from "BPAlternativenergy Inc." [107]. This PV array defines the nominal input power of the single-stage inverter, whose value is $9kW$, with $600V$ input DC voltage and $15A$ input current. The switching frequency of the inverter is $10kHz$. The grid RMS phase voltage is $325V$ and its frequency is $60Hz$.

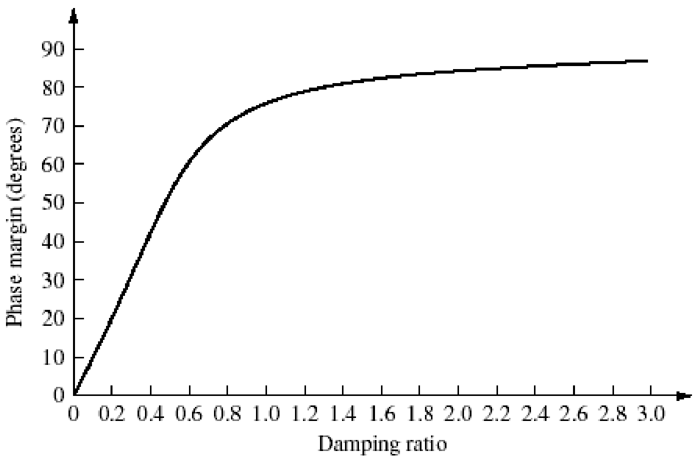

Fig. 5.12: Phase margin vs. damping ratio of a second order system.

Four criteria play an essential role in the choice of DC link capacitor [35],

$$C_{DC} > \frac{T_r \Delta P_{max}}{2V_o \Delta V_o}, \tag{5.17}$$

where T_r is the introduced delays by filtering of the DC voltage and current control loop, ΔP_{max} is the maximum variation of the power on DC bus, ΔV_o is the acceptable voltage tolerance on DC bus. Obviously, there is a trade-off between the time response of the system and tolerable DC bus voltage and power variations. Usually, the higher the capacitance of DC link capacitor, the better the system. However, C is limited by cost, size, and safety considerations.

Grid line inductors are determined by [6]

$$L = \frac{\sqrt{2}V_g}{4f_{sw}\Delta I_L}, \tag{5.18}$$

where ΔI_L is the acceptable ripple current, V_g is the voltage of the grid, and f_{sw} is the switching frequency of the inverter.

According to (5.17) and (5.18), the inductance of the output filter and DC link capacitor are designed to be $10mH$ and $1mF$, respectively. The sampling time is $10kHz$. Considering a high sampling period as well as a low cut-off frequencies on control loops, the phase lag in the system is very small and can be disregarded.

Tuning of Controllers

According to the power electronics design values, the normalized open-loop transfer function of the current control loop is

$$G_P(s) = \frac{1}{0.01s + 1} e^{1e-4s}. \tag{5.19}$$

The Equivalent Series Resistance (ESR) of the output filter is assumed to be 1Ω.

To obtain a fair comparison between integer order and fractional order controllers, the same tuning approach, which has been discussed in Chapter 2, is applied to all the controllers. As discussed before, since the derived tuning equations for FO-PI and FO-[PI] are a set of nonlinear equations which cannot be solved analytically, the graphical method is employed to find the solution(s).

To tune the FO-PI controller for the current loop, equations (2.72) and (2.76) are depicted in the same plot, as seen in Fig. 5.13. The intersection point between these two plots determines the order and integrator gain of the FO-PI. By substituting these two values to (2.75), the proportional gain of FO-PI is determined.

The gains of FO-[PI] can be determined by plotting equations (2.80) and (2.83) as shown in Fig. 5.14. The integrator gain and order of the controller are obtained from the intersection(s) of these plots. Then, by substituting these two values to (2.82), the proportional gain of FO-[PI] is determined.

Following this method, the tuned gains for FO-PI are $k_p = 3.10$, $k_i = 132$ and $\lambda = 0.72$. By applying the same approach to FO-[PI], these gains are obtained; $k_p = 11$, $k_i = 13650$ and $\lambda = 0.56$. The proportional and integral gains of the IO-PI are obtained by (2.87) and (2.88) and these values are $k_p = 4.63$ and $k_i = 2020$.

Consequently, the tuned current controllers for the benchmarked three-phase grid-connected PV system are

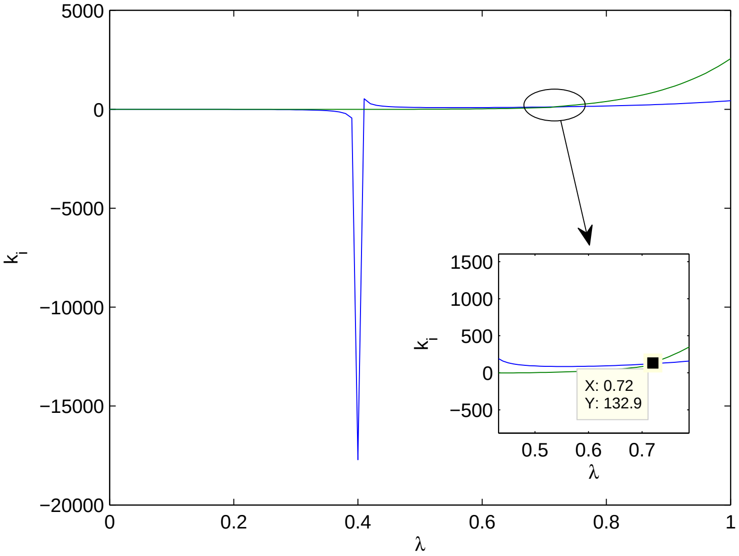

Fig. 5.13: Graphical method of finding k_i and λ for FO-PI.

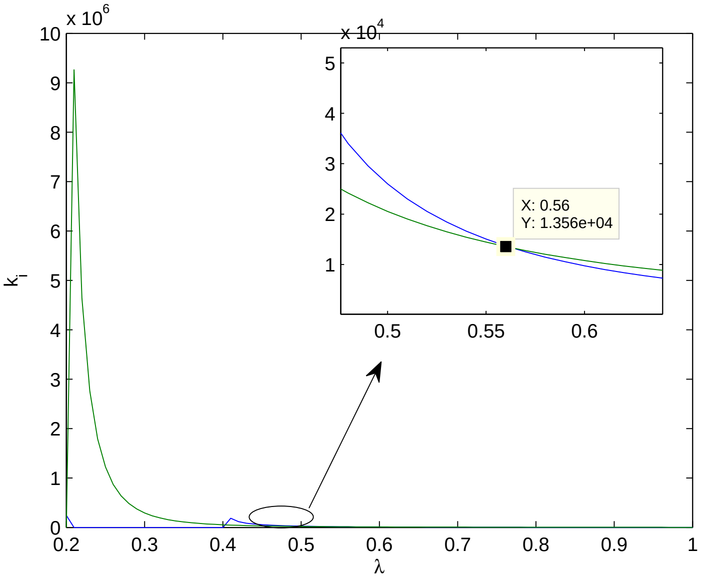

Fig. 5.14: Graphical method of finding k_i and λ for FO-[PI].

$$\begin{aligned} C_{IOPI} &= 4.63 + \tfrac{2020}{s} \\ C_{FOPI} &= 3.10\Big(1 + \tfrac{132}{s^{0.72}}\Big) \\ C_{FO[PI]} &= \Big(11 + \tfrac{13650}{s}\Big)^{0.56}. \end{aligned} \tag{5.20}$$

To implement the FO-PI and FO-[PI] controllers, "ninteger" toolbox and "impulse response invariant discretization" methods will be used [108, 109].

The truncation order of estimated integer order transfer function will be defined to be five in both cases. It has been observed that increasing the order of truncation did not improve the simulation results and decreasing this order reduces the accuracy of the results. The Bode plots of these three controllers have been depicted in Fig. 5.15.

As seen in Fig. 5.15, IO-PI, FO-PI, and FO-[PI] satisfy the design criteria for cross-over frequency and phase margin. The fractional order controllers have a flat phase around cross-over frequency, which means these controllers have more robustness against gain variations. In other words, a small amount of gain variation shifts the cross-over frequency to higher or lower frequencies, which will change the phase margin of the controlled plant by IO-PI. But under gain variation condition, the phase margin remains constant for FO-PI and FO-[PI] since their phase plots are flat around the cross-over frequency.

This feature is an important feature for a controller in the grid-connected PV systems because, in addition to the deviation of nominal designed values in the passive components (which is caused by ambient temperature or aging), the DC bus voltage, inverter gain, grid voltage and frequency, etc. fluctuate in the system continuously. All of these deviations in the system parameters vary the dynamics of the system. Hence, having a robust controller which can tolerate these type of uncertainties is highly desirable in this application.

The time response of these three controllers have been illustrated in Fig. 5.16. As shown in this figure, the overshoots of step responses in the designed FO-[PI] and FO-PI controllers are smaller than IO-PI.

In Fig. 5.17, the step responses of the designed IO-PI, FO-PI, and FO-[PI] under

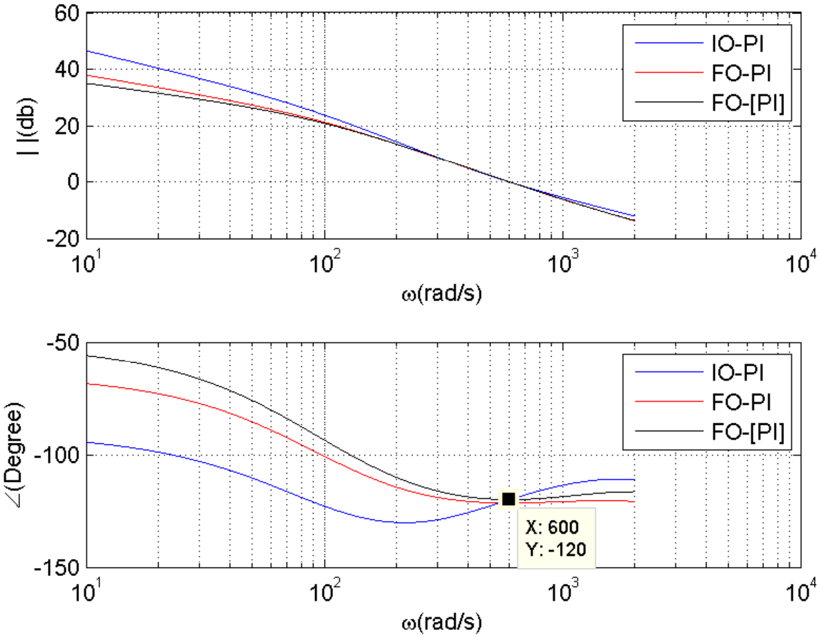

Fig. 5.15: Bode plot of controlled system using IO-PI and FO-PI.

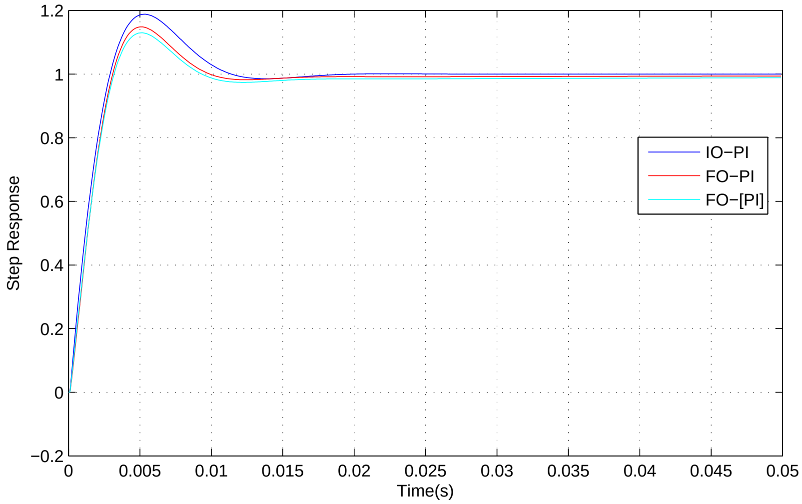

Fig. 5.16: Time response comparison among three controllers.

±20% open-loop gain variations are depicted. The amplitude of the input step has been normalized.

The percentage of overshoot deviations under gain variations are reported in Table 5.1. Clearly, the system has less overshoot deviations under loop gain variations when fractional order controllers are applied.

5.3.3 Tuning of Voltage Controller

The open-loop transfer function for voltage control loop is

$$G_P(s) = \frac{1}{0.001s} e^{1e-4s} M_{id}, \tag{5.21}$$

where the reduced order M_{id} for FO-PI is

$$M_{id} = \frac{1}{0.003s + 1.33}, \tag{5.22}$$

for FO-[PI], the reduced order M_{id} is

$$M_{id} = \frac{3.8}{0.01s + 4.8}, \tag{5.23}$$

and eventually, the reduced order M_{id} for IO-PI is

$$M_{id} = \frac{4}{0.01s + 5}. \tag{5.24}$$

In all three cases, M_{id} has a pole which is far from imaginary axis and then the voltage control loop can be approximated by

$$G_P(s) = \frac{1}{0.001s} e^{1e-4s}. \tag{5.25}$$

By applying the proposed tuning method, the tuned gains of IO-PI for the voltage control loop are $k_p = 0.2$, $k_i = 10$.

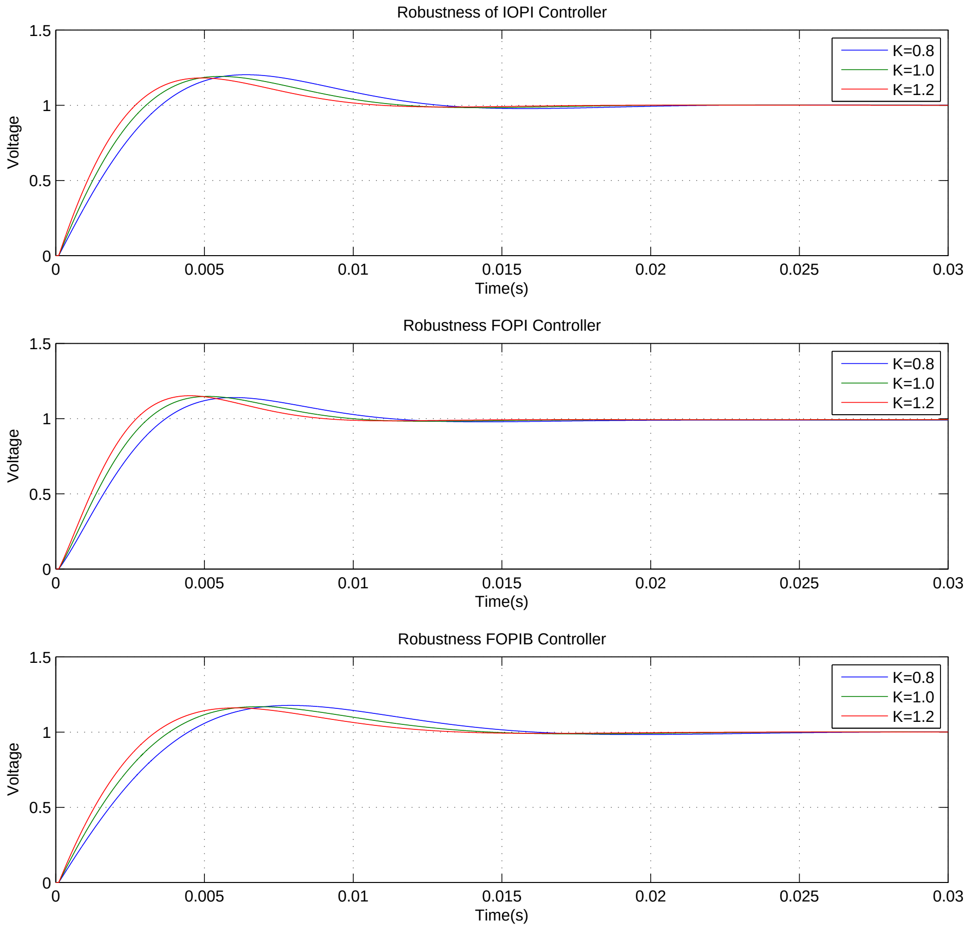

Robustness of IOPI Controller

Robustness FOPI Controller

Robustness FOPIB Controller

Fig. 5.17: Robustness comparison among all three controllers.

Table 5.1: Overshoot variation in presence of open-loop gain variations.

Controller	Variations in Overshoot
IO-PI	1.82%
FO-PI	1.42%
FO-[PI]	1.03%

In the case of FO-PI, according to Fig. 5.18, the intersection point of two plots determines the order and integrator gain of FO-PI. By substituting these two values in (2.75), the proportional gain is obtained. As seen in Fig. 5.18, the optimal order of integrator is 1 and the integrator gain of FO-PI is equal to 9.09 which is close to the integrator gain of IO-PI.

The same approach has been applied for the tuning of FO-[PI], and according to Fig. 5.19, k_i and λ of FO-[PI] are obtained. By substituting these two values into (2.82), the k_p is determined. As seen in Fig. 5.19, for FO-[PI], $\lambda = 1$, $k_i = 10$, and $k_p = 0.2$ which are equal to the integrator and proportional gains of IO-PI and FO-PI. This means that all three controllers have the same gains and orders for voltage control loop under required design criteria. The designed controller for the voltage loop control will be

$$C(s) = 0.2 + \frac{10}{s}. \tag{5.26}$$

The Bode plot of the voltage control loop has been illustrated in Fig. 5.20.

5.3.4 Simulation of Three-Phase Grid-Connected PV System

To evaluate the performance of the benchmarked three-phase grid-connected PV system using IOPI, FOPI, and FO[PI] controllers, in the first step, the behavior of this system under step-like and ramp-like sun irradiation variations will be investigated. For this set of simulations, sun irradiation varies as follow: $G = 0.5$ for $t \in (0, 0.05)$, and it will be, $G = 0$ for $t \in (0.05, 0.1)$, and then $G = 1$ for $t \in (0.1, 0.15)$, then G decreases from 1.0 to

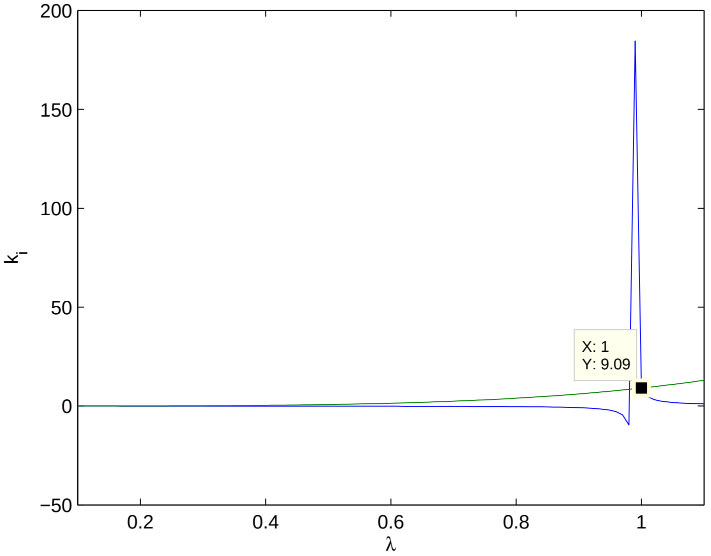

Fig. 5.18: Graphical method of finding k_i and λ for FO-PI.

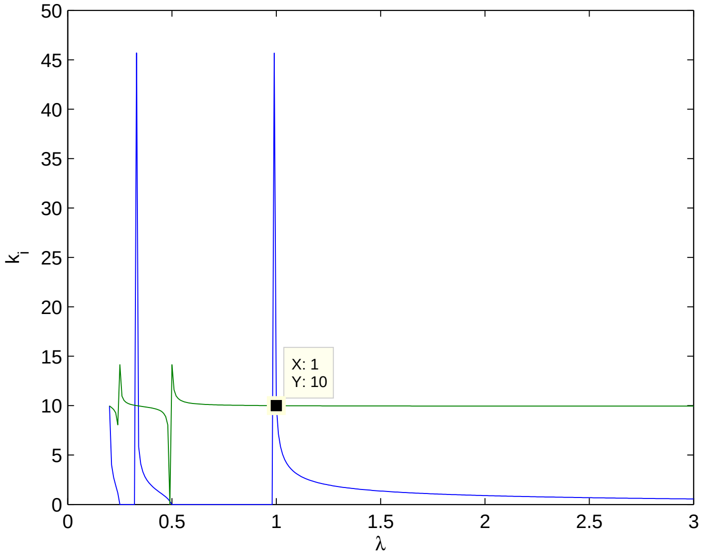

Fig. 5.19: Graphical method of finding k_i and λ for FO-[PI].

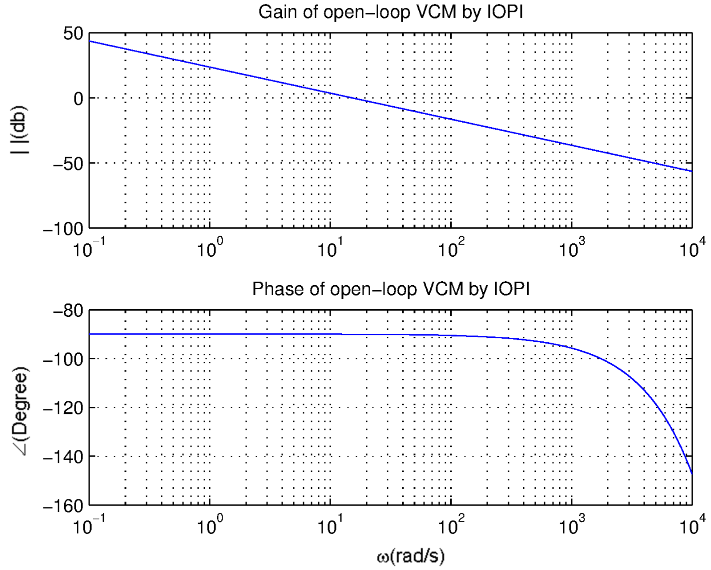

Fig. 5.20: Bode plot of voltage controlled system.

0.6 within the time period of $t \in (0.15, 0.17)$, and $G = 0.6$ for $t \in (0.17, 0.2)$ according to Fig. 5.21.

Figure 5.22 illustrates the DC link voltage of the system during sun irradiation fluctuations. Although the voltage controller is similar for all three current controllers, but since current control loop have different regulators which cause different dynamics, the DC link voltage acts differently. Obviously, in the case of using fractional order controllers, DC bus faces less overshoot compared to IO-PI regulator.

Figure 5.23 shows that fractional order controllers and IO-PI controller have the same responses for the ramp-like sun irradiation variations, but in the case of step-like fluctuations in the sun irradiation, FO-PI and FO-[PI] extract more power from PV array.

Figure 5.24 illustrates the active and reactive injected power to the grid. As mentioned before, current controllers try to increase the efficiency by maximizing the active power and forcing the reactive power to be zero. However, fractional order controllers have better time response features in the power control scheme. As can be seen in Fig. 5.24, the amount of reactive power delivered to the grid is higher when the system is controlled by IO-PI

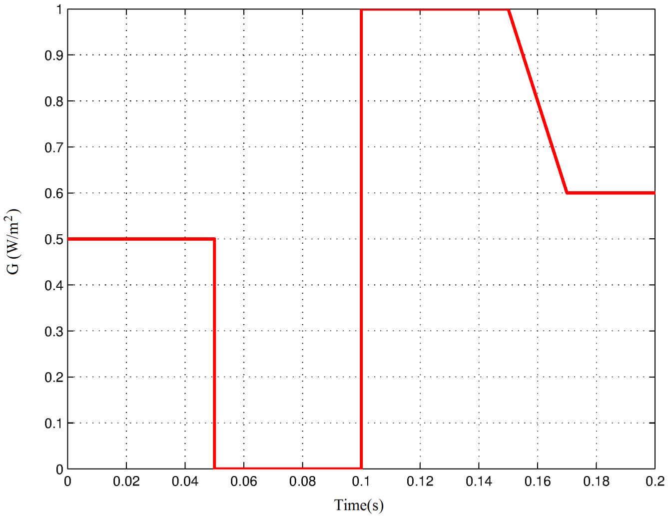

Fig. 5.21: Sun irradiation profile.

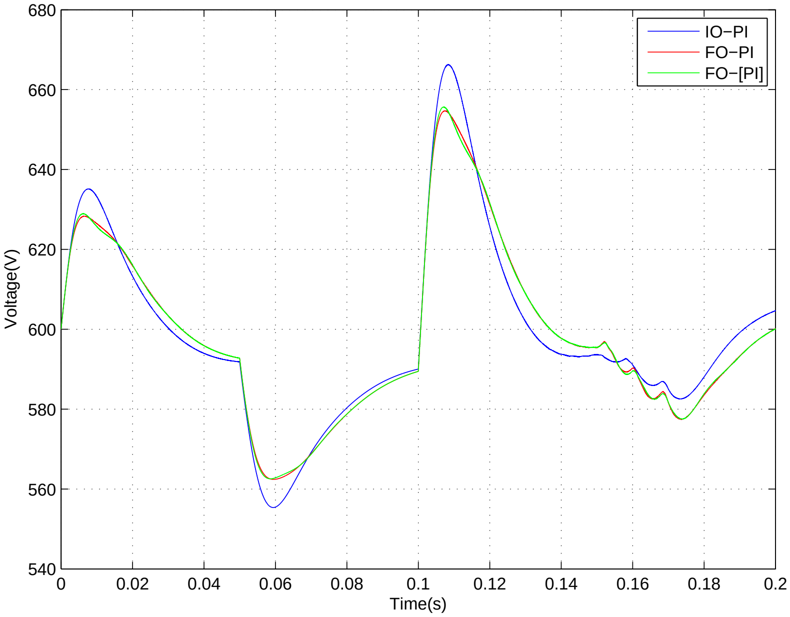

Fig. 5.22: Grid voltage of three-phase grid-connected PV system.

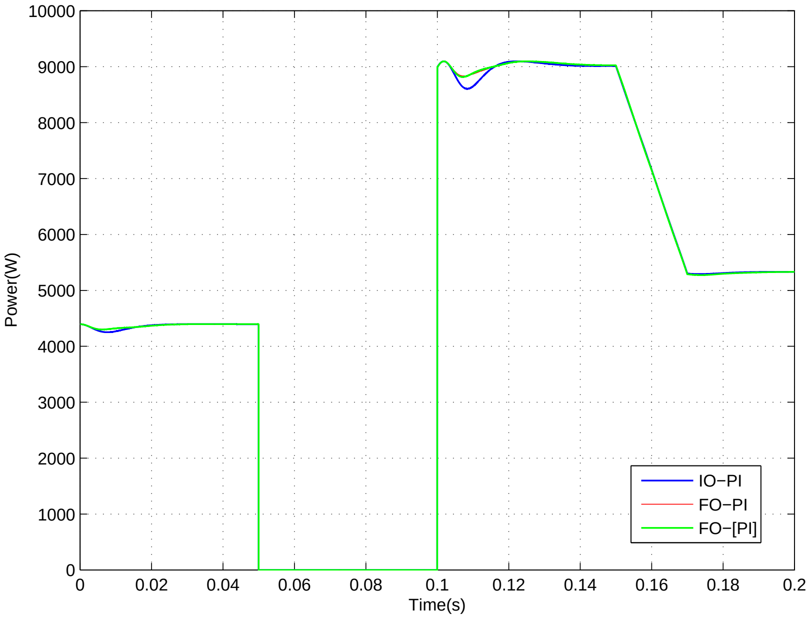

Fig. 5.23: Ouput power of PV panels.

controller. Therefore, using IO-PI controller results less efficiency compared to fractional order controllers.

If the system works under sun irradiation variation profile of Fig. 5.21, the total harmonic distortion (THD) of the injected current to the grid will be as shown in Fig. 5.25. According to these results, a grid-connected PV system, controlled by fractional order controllers, deliver current to the grid with acceptable amounts of THD according to $IEEE929$ and this THD is less than the level of THD of the inverter output current when it is controlled by IO-PI.

To investigate the robustness of the controller, the effect of changing the output filter inductance value on the THD of output current has been evaluated. The simulations have been done with nominal inductance $L = 0.01H$ and $L = 0.012H$. Figure 5.26 illustrates the THD of phase (a) of a three-phase grid-connected PV system when filter has the nominl inductance and also when its inductance increases by 20%. As seen in this figure, IO-PI controller has totally different THDs under different inductances but FO-PI and FO-[PI] have similar THD level and they can tolerate some level of deviations in the system as

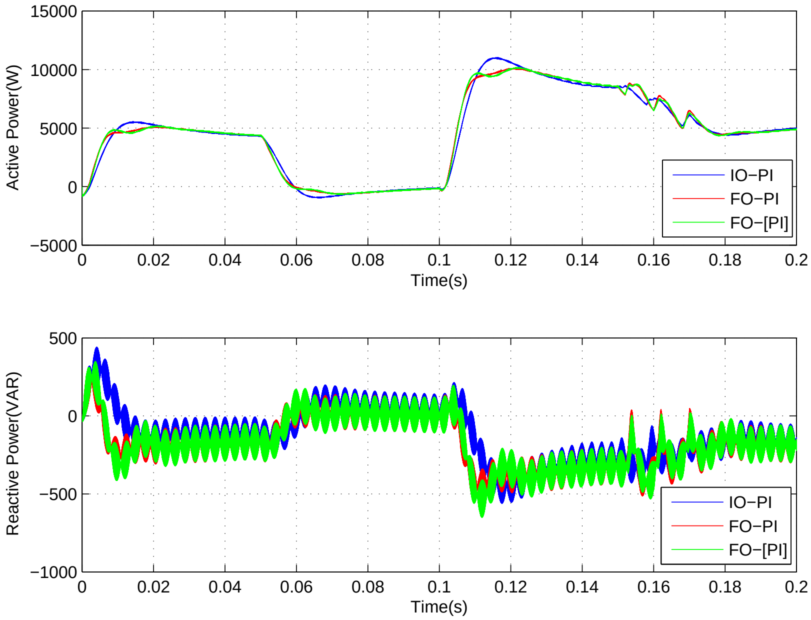

Fig. 5.24: Active and reactive power of the three-phase grid-connected PV system.

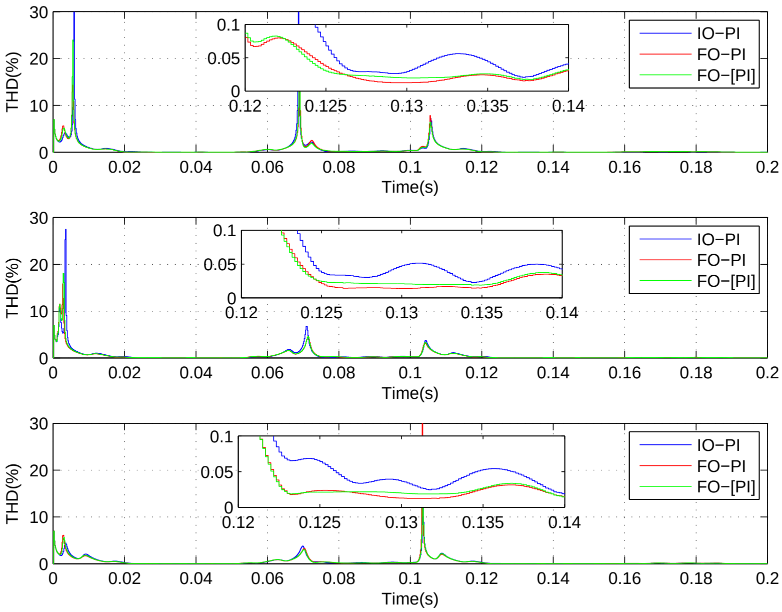

Fig. 5.25: Total harmonic distortion of the three-phase grid-connected system.

expected.

5.4 Summary

The advantages of using FO-PI and FO-[PI] compared to IO-PI in the voltage and current control loops of a three-phase grid-connected PV system was presented in this chapter. According to the simulation studies, FO-PI and FO-[PI] are more robust against the system uncertainties compared to IO-PI. In addition, using FO-PI and FO-[PI] decrease the amount of delivered reactive power to the grid and consequently, increase the efficiency of the system.

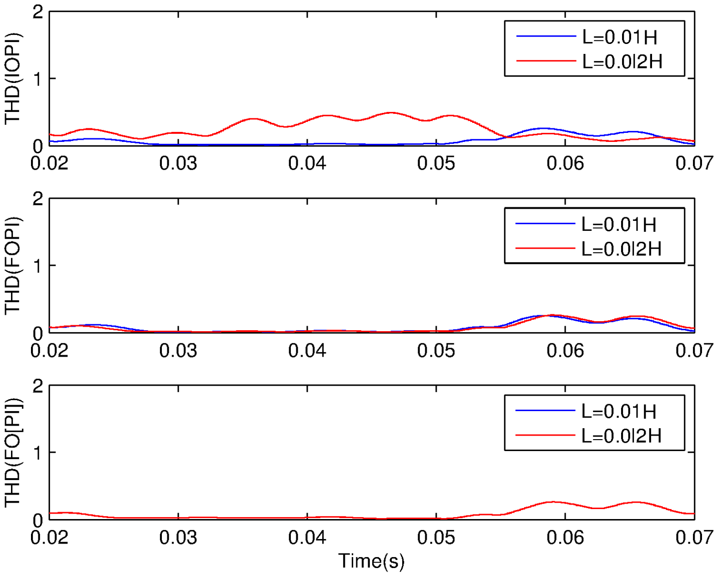

Fig. 5.26: Robustness of controlled grid-connected PV system against output filter indutance deviations.

Chapter 6

Conclusion and Future Works

The main purpose of this dissertation was to develop a close-loop control system for a three-phase grid-connected PV system. The intention of the control system is to achieve peak power point tracking to extract the maximum amount of power from the PV array and control the output current and voltage of the inverter.

A two-level three-phase inverter with an inductive filter was chosen, due to the fact that this topology is more popular and simple in a grid-connected PV system. Although there are many different types of inverters for grid-connected PV systems and some of them have better performance than the considered plant, the goal of this work is to compare different control strategies, and therefore a specific topology used in the benchmark is not an essential aspect in this work.

The main contributions of this research can be summarized as follows:

- This dissertation has introduced two types of MPPT algorithms, fractional order extremum seeking control and BICO extremum seeking control, which have better features compared to the existing MPPT methods.

  First, these two algorithms have shorter rise time and faster convergence rate and they can follow the rapid variations in the environmental conditions. Therefore, the possibility of getting lost from the peak power point tracking is lower in these two proposed MPPT algorithms compared to the previous ones. In addition, faster convergence response may help in reducing the amount of capacitance needed for DC link capacitor. Furthermore, the stability of these two algorithms has been investigated and it has been shown that the BICO ESC and FO-ESC have more stability margin in comparison with IO-ESC. Moreover, a fractional horse power dynamometer has been benchmarked to compare the FO-ESC and IO-ESC performances.

- In the second part of this dissertation, the control-loop performance in a three-phase grid-connected PV system has been improved by using two types of fractional order controllers, FO-PI and FO-[PI]. It has been shown that using these controllers not only improves the efficiency of the system, but also the system can tolerate more deviations in its parameters. These variations may occur because of environmental conditions or aging in the components. By considering the results of this work, it can be concluded that fractional order controllers are less sensitive to the mentioned uncertainties.

  Moreover, fractional order controllers improve the time response of grid-connected PV system by injecting less oscillation to the grid and therefore less THD. This feature improves the efficiency of the system by reducing the losses caused by THD.

Although the work presented in this dissertation has achieved some interesting results from analysis and control point of view for grid-connected systems, many problems remain open and will be the subject of future investigations. The main future research items are:

- The extension of fractional order controllers in the stationary domain for grid connected systems.
- Applying the fractional order controllers and MPPT algorithms to other grid connected PV system topologies for instance the LCL filtering topology.
- Thermal analysis of grid connected system and comparing the thermal losses and amount of stress on the switches in the inverter when the control system is under fractional order controllers and integer order controllers
- Applying distributed-order controllers to the grid connected PV systems.
- Hardware implementation of MPPT algorithms and fractional order controllers.

References

[1] D. L. Chandler, "What can make a dent?" MIT News, Oct. 2011.

[2] Wikipedia, "Solar energy," March 2014. [Online]. Available: http://en.wikipedia.org/wiki/Solar_energy

[3] G. Carr, "Alternative energy will no longer be alternative," *The Economist*, Nov. 2012. [Online]. Available: http://www.economist.com/news/21566414-alternative-energy-will-no-longer-be-alternative-sunny-uplands

[4] NREL, "Best research photovoltaic cell efficiencies," Dec. 2013.

[5] X. Yuan and Y. Zhang, "Status and opportunities of photovoltaic inverters in grid-tied and micro-grid systems," *Proceedings of CES/IEEE 5th International Power Electronics and Motion Control Conference (IPEMC)*, vol. 1, pp. 1–4, Aug. 2006.

[6] D. C. Martins, "Analysis of a three-phase grid-connected PV power system using a modified dual-stage inverter," *International Scholarly Research Notices (ISRN) Renewable Energy*, vol. 2013, pp. 1–18, 2013.

[7] A. Khalifa and E. El-Saadany, "Control of three-phase grid-connected photovoltaic arrays with open loop maximum power point tracking," *Proceedings of IEEE Power and Energy Society General Meeting*, pp. 1–8, 2011.

[8] M. Calais, J. Myrzik, T. Spooner, and V. Agelidis, "Inverters for single-phase grid-connected photovoltaic systems-an overview," *Proceedings of 33rd IEEE Annual Power Electronics Specialists Conference (PESC 02)*, vol. 4, pp. 1995–2000, 2002.

[9] B. Verhoeven, "Utility aspects of grid connected photovoltaic power systems," International Energy Agency Implementing Agreement on Photovoltaic Power Systems, Report IEA PVPS T5-01, 1998.

[10] M. Meinhardt and G. Cramer, "Past, present and future of grid connected photovoltaic- and hybrid-power-systems," *Proceedings of IEEE Power Engineering Society Summer Meeting*, vol. 2, pp. 1283–1288, 2000.

[11] International Energy Agency, "Innovative electrical concepts," International Energy Agency (IEA), Report IEA PVPS T7-7, 2001.

[12] J. Riatsch, H. Stemmler, and R. Schmidt, "Single cell module integrated converter system for photovoltaic energy generation," *Proceedings of Conference on European Power Electronics(EPE97)*, pp. 71–77, 1997.

[13] H. Li, Y. Xu, S. Adhikari, D. T. Rizy, F. Li, and P. Irminger, "Real and reactive power control of a three-phase single-stage PV system and PV voltage stability," UT-Battelle LLC, Tech. Rep., 2012.

[14] J. Carrasco, L. Franquelo, J. Bialasiewicz, E. Galvan, R. Guisado, M. Prats, J. Leon, and N. Moreno-Alfonso, “Power-electronic systems for the grid integration of renewable energy sources: A survey,” *IEEE Transactions on Industrial Electronics*, vol. 53, no. 4, pp. 1002–1016, June 2006.

[15] M. Liserre, R. Teodorescu, and F. Blaabjerg, “Stability of grid-connected PV inverters with large grid impedance variation,” *Proceedings of 35th IEEE Annual Power Electronics Specialists Conference (PESC 04)*, vol. 6, pp. 4773–4779, June 2004.

[16] R. Teodorescu, F. Blaabjerg, U. Borup, and M. Liserre, “A new control structure for grid-connected LCL PV inverters with zero steady-state error and selective harmonic compensation,” *Proceedings of 19th Annual IEEE Applied Power Electronics Conference and Exposition, (APEC ’04)*, vol. 1, pp. 580–586, 2004.

[17] IEEE, “IEEE standard for interconnecting distributed resources with electric power systems,” Standards Coordinating Committee, IEEE Standards 1547, 2003.

[18] S. E. Evju, “Fundamentals of grid connected photovoltaic power electronic converter design,” Ph.D. dissertation, Department of Electrical Power Engineering, Norwegian University of Science and Technology, Jan. 2007.

[19] S. Kjaer, J. Pedersen, and F. Blaabjerg, “A review of single-phase grid-connected inverters for photovoltaic modules,” *IEEE Transactions on Industry Applications*, vol. 41, no. 5, pp. 1292–1306, Sept. 2005.

[20] S. Kjaer, “Design and control of an inverter for photovoltaic applications,” Ph.D. dissertation, Faculty of Engineering and Science at Aalborg University, Jan. 2005.

[21] NREL, “Solar radiation data manual for flat-plate and concentrating collectors,” National Renewable Energy Laboratory, RedBook, 1991.

[22] F. Blaabjerg, Z. Chen, and S. Kjaer, “Power electronics as efficient interface in dispersed power generation systems,” *IEEE Transactions on Power Electronics*, vol. 19, no. 5, pp. 1184–1194, Sept. 2004.

[23] A. Boue, R. Valverde, F. RuzVila, and J. Ponce, “An integrative approach to the design methodology for three phase power conditioners in photovoltaic grid-connected systems,” *Energy Conversion and Management*, vol. 56, pp. 80–95, 2012.

[24] B. McGrath, S. Parker, and D. Holmes, “High performance stationary frame AC current regulation incorporating transport delay compensation,” *Proceedings of 14th European Conference on Power Electronics and Applications (EPE11)*, pp. 1–10, Sept. 2011.

[25] M. Kazmierkowski, R. Krishnan, and F. Blaabjerg, *Control in Power Electroncis: Selected Problems*, 1st ed., ser. 978-0124027725. San Diego: Academic Press, 2002.

[26] S. Buso and P. Mattavelli, *Digital Control in Power Electronics*, ser. 978-1598291124. Denver: Morgan and Claypool Publishers, 2006.

[27] M. Kazmierkowski and L. Malesani, "Current control techniques for three-phase voltage-source PWM converters: A survey," *IEEE Transactions on Industrial Electronics*, vol. 45, no. 5, pp. 691–703, Oct. 1998.

[28] N. Zargari and G. Joos, "Performance investigation of a current-controlled voltage-regulated PWM rectifier in rotating and stationary frames," *IEEE Transactions on Industrial Electronics*, vol. 42, no. 4, pp. 396–401, Aug. 1995.

[29] H. Komurcugil and O. Kukrer, "A novel current-control method for three-phase PWM AC/DC voltage-source converters," *IEEE Transactions on Industrial Electronics*, vol. 46, no. 3, pp. 544–553, June 1999.

[30] C. Ho, V. Cheung, and H. Chung, "Constant-frequency hysteresis current control of grid-connected vsi without bandwidth control," *IEEE Transactions on Power Electronics*, vol. 24, no. 11, pp. 2484–2495, Nov. 2009.

[31] L. Malesani, P. Mattavelli, and P. Tomasin, "Improved constant-frequency hysteresis current control of VSI inverters with simple feedforward bandwidth prediction," *IEEE Transactions on Industry Applications*, vol. 33, no. 5, pp. 1194–1202, Sept. 1997.

[32] Y. Jingrong, S. Mei, and S. Yao, "A novel current control method for grid connected photovoltaic system," *Proceedings of Asia-Pacific Power and Energy Engineering Conference (APPEEC)*, pp. 1–4, March 2011.

[33] M. Odavic, P. Zanchetta, M. Sumner, and Z. Jakopovic, "High performance predictive current control for active shunt filters," *Proceedings of 12th International Power Electronics and Motion Control Conference (EPE-PEMC)*, pp. 1677–1681, Sept. 2006.

[34] F. Blaabjerg, R. Teodorescu, M. Liserre, and A. Timbus, "Overview of control and grid synchronization for distributed power generation systems," *IEEE Transactions on Industrial Electronics*, vol. 53, no. 5, pp. 1398–1409, Oct. 2006.

[35] M. Liserre, F. Blaabjergb, and A. DellAquilaa, "Step-by-step design procedure for a grid-connected three-phase PWM voltage source converter," *International Journal of Electronics*, vol. 91, no. 8, pp. 445–460, 2004.

[36] S. Golestan, M. Monfared, J. Guerrero, and M. Joorabian, "A D-Q synchronous frame controller for single-phase inverters," *Proceedings of 2nd Power Electronics, Drive Systems and Technologies Conference (PEDSTC)*, pp. 317–323, Feb. 2011.

[37] S. R. Nandurkar and M. Rajeev, "Design and simulation of three phase inverter for grid connected photovoltic systems," *Third Biennial National Conference (NCNTE)*, pp. 80–83, Feb. 2012.

[38] J. Selvaraj and N. Rahim, "Multilevel inverter for grid-connected PV system employing digital PI controller," *IEEE Transactions on Industrial Electronics*, vol. 56, no. 1, pp. 149–158, Jan. 2009.

[39] M. Ciobotaru, R. Teodorescu, and F. Blaabjerg, "Control of single-stage single-phase PV inverter," *Proceedings of European Conference on Power Electronics and Applications*, 2005.

[40] E. Villanueva, P. Correa, J. Rodriguez, and M. Pacas, "Control of a single-phase cascaded H-bridge multilevel inverter for grid-connected photovoltaic systems," *IEEE Transactions on Industrial Electronics*, vol. 56, no. 11, pp. 4399–4406, Nov. 2009.

[41] D. Zmood and D. Holmes, "Stationary frame current regulation of PWM inverters with zero steady-state error," *IEEE Transactions on Power Electronics*, vol. 18, no. 3, pp. 814–822, May 2003.

[42] X. Ye, X. Xia, J. Zhang, and Y. Chen, "Fractional analysis and synthesis of the variability of irradiance and PV power time series," *Proceedings of Fractional Differentiation and its Application (FDA)*, May 2012.

[43] J. Sabatier, M. Aoun, A. Oustaloup, G. Gregoire, F. Ragot, and P. Roy, "Fractional system identification for lead acid battery state of charge estimation," *Signal Processing*, vol. 86, no. 10, pp. 2645–2657, 2006.

[44] I. Podlubny, *Fractional Differential Equations. An Introduction to Fractional Derivatives, Fractional Differential Equations, Some Methods of Their Solution and Some of Their Applications.* San Diego: Academic Press, 1999.

[45] C. A. Monje, B. M. Vinagre, V. Feliu, and Y. Chen, "Tuning and auto-tuning of fractional order controllers for industry applications," *Control Engineering Practice*, vol. 16, no. 7, pp. 798–812, 2008.

[46] M. Zamani, M. Karimi-Ghartemani, N. Sadati, and M. Parniani, "Design of a fractional order PID controller for an AVR using particle swarm optimization," *Control Engineering Practice*, vol. 17, no. 12, pp. 1380–1387, 2009.

[47] C. A. Monje, Y. Chen, B. M. Vinagre, D. Xue, and V. Feliu-Batlle, *Fractional-order Systems and Controls: Fundamentals and Applications (Advances in Industrial Control).* New York: Springer, 2010.

[48] A. Calderon, B. Vinagre, and V. Feliu, "Fractional order control strategies for power electronic buck converters," *Signal Processing*, vol. 86, no. 10, pp. 2803–2819, Oct. 2006.

[49] A. J. Calderon, B. M. Vinagre, and V. Feliu, "Linear fractional order control of a DC-DC buck converter," *Proceedings of European Control Conference (ECC03)*, 2003.

[50] R. Melicio, V. Mendes, and J. Catalo, "Fractional-order control and simulation of wind energy systems with PMSG/full-power converter topology," *Energy Conversion and Management*, vol. 51, no. 6, pp. 1250–1258, 2010.

[51] R. Melicio, J. Catalao, and V. Mendes, "Fractional-order control and simulation of wind turbines with full-power converters," *Proceedings of 15th IEEE Mediterranean Electrotechnical Conference (MELECON10)*, pp. 320–325, Apr. 2010.

[52] K.-A. Tehrani, T. Capitaine, L. Barrandon, M. Hamzaoui, S. Rafiei, and A. Lebrun, "Current control design with a fractional-order PID for a three-level inverter," *Proceedings of 14th European Conference on Power Electronics and Applications (EPE 2011)*, pp. 1–7, Sep. 2011.

[53] I. Rasoanarivo, K. ArabTehrani, and F. Sargos, “Fractional order PID and modulated hysteresis for high performance current control in multilevel inverters,” *Proceedings of IEEE Industry Applications Society Annual Meeting (IAS)*, pp. 1–7, Oct. 2011.

[54] H. Malek, Y. Luo, and Y. Chen, “Identification and tuning fractional order proportional integral controllers for time delayed systems with a fractional pole,” *Mechatronics*, vol. 23, no. 7, pp. 746–754, Oct. 2013.

[55] H. J. Haubold, A. M. Mathai, and R. K. Saxena, “Mittag-Leffler functions and their applications,” *Journal of Applied Mathematics*, vol. 2011, 2011.

[56] I. Petras, *Fractional Order Nonlinear Systems, Modeling, Analysis and Simulation.* New York: Springer, 2011.

[57] C. Li, D. Qian, and Y. Chen, “On Riemann-Liouville and Caputo derivatives,” *Discrete Dynamics in Nature and Society*, vol. 2011, 2011.

[58] F. Oberhettinger and L. Baddi, *Tables of Laplace Transforms.* Berlin, New York: Springer-Verlag, 1973.

[59] I. Podlubny, “Geometric and physical interpretation of fractional integration and fractional differentiation,” *Fractional Calculus and Applied Analysis*, vol. 5, no. 4, pp. 367–386, 2002.

[60] D. Valerio and J. S. da Costa, *An Introduction to Fractional Control.* Stevenage, UK: The Institution of Engineering and Technology (IET), 2012, no. 978-1-84919-545-4.

[61] M. S. Tavazoei and M. Haeri, “Chaotic attractors in incommensurate fractional order systems,” *Physica D, Nonlinear Phenomena*, vol. 237, no. 20, pp. 2628–2637, 2008.

[62] Y. Luo and Y. Chen, *Fractional Order Motion Controls.* Chichester, UK: John Wiley & Sons, Ltd, 2012.

[63] Y. Chen, “Ubiquitous Fractional order Controls?” *Proceedings of 2nd IFAC Symposium on Fractional Derivatives and Applications (IFAC FDA06)*, 2006.

[64] Y. Chen and K. L. Moore, “Discretization schemes for fractional-order differentiators and integrators,” *IEEE Transactions on Circuit and Systems*, vol. 49, no. 3, pp. 363–367, Mar. 2002.

[65] C. Jiang, J. Carletta, and T. Hartley, *Advances in Fractional Calculus (Implementation of Fractional-order Operators on Field Programmable Gate Arrays).* New York: Springer, 2007, ch. 5, pp. 333–346.

[66] I. Petras and S. Grega, “Digital fractional order controllers realized by PIC microprocessor: Experimental results,” *Proceedings of the International Carpathian Control Conference (ICCC03)*, pp. 873–876, May 2003.

[67] Y. Luo, Y. Chen, C. Wang, and Y. G. Pi, “Tuning fractional order proportional integral controllers for fractional order systems.” *Journal of Process Control*, vol. 20, pp. 823–831, 2010.

[68] M. A. Mahmud, H. Pota, and M. J. Hossain, "Dynamic stability of three-phase grid-connected photovoltaic system using zero dynamic design approach," *IEEE Journal of Photovoltaics*, vol. 2, no. 4, pp. 564–571, 2012.

[69] S. L. Brunton, C. W. Rowley, S. R. Kulkarni, and C. Clarkson, "Maximum power point tracking for photovoltaic optimization using ripple-based extremum seeking control," *IEEE Transactions on Power Electronics*, vol. 25, no. 10, pp. 2531–2540, 2010.

[70] A. Cupertino, J. deResende, H. Pereira, and S. SelemeJunior, "A grid-connected photovoltaic system with a maximum power point tracker using passivity-based control applied in a boost converter," *Proceedings of 10th IEEE/IAS International Conference on Industry Applications (INDUSCON)*, pp. 1–8, 2012.

[71] M. Kazmierkowski, R. Krishnan, F. Blaabjerg, and J. Irwin, *Control in Power Electronics: Selected Problems*, 1st ed. San Diego: Academic Press, 2002.

[72] A. Mehrizi-Sani, S. Filizadeh, and P. L. Wilson, "Harmonic and loss analysis of space-vector modulated converters," *Proceedings of International Conference on Power Systems Transients (IPST07)*, 2007.

[73] K. Zhou and D. Wang, "Relationship between space-vector modulation and three-phase carrier-based PWM: A comprehensive analysis," *IEEE Transactions on Industrial Electronics*, vol. 49, no. 1, pp. 186–196, 2002.

[74] A. Timbus, M. Liserre, R. Teodorescu, and F. Blaabjerg, "Synchronization methods for three phase distributed power generation systems - An overview and evaluation," *Proceedings of 36th IEEE Power Electronics Specialists Conference (PESC '05)*, pp. 2474–2481, 2005.

[75] J. Enslin, M. Wolf, D. Snyman, and W. Swiegers, "Integrated photovoltaic maximum power point tracking converter," *IEEE Transactions on Industrial Electronics*, vol. 44, no. 6, pp. 769–773, 1997.

[76] B. Bose, P. Szczesny, and R. Steigerwald, "Microcomputer control of a residential photovoltaic power conditioning system," *IEEE Transactions on Industry Applications*, vol. IA-21, no. 5, pp. 1182–1191, Sept. 1985.

[77] R. Mastromauro, M. Liserre, T. Kerekes, and A. DellAquila, "A singlephase voltage-controlled grid-connected photovoltaic system with power quality conditioner functionality," *IEEE Transactions on Industrial Electronics*, vol. 56, no. 11, pp. 4436–4444, Nov. 2009.

[78] T. Esram and P. L. Chapman, "Comparison of photovoltaic array maximum power point tracking techniques," *IEEE Transactions on Energy Conversion*, vol. 22, pp. 439–449, June 2007.

[79] J. Nedumgatt, K. Jayakrishnan, S. Umashankar, D. Vijayakumar, and D. Kothari, "Perturb and observe MPPT algorithm for solar PV systems-modeling and simulation," *Proceedings of Annual IEEE India Conference (INDICON)*, pp. 1–6, Dec. 2011.

[80] R. Alonso, P. Ibaez, V. Martinez, E. Roman, and A. Sanz, “An innovative perturb, observe and check algorithm for partially shaded PV systems,” *Proceedings of 13th European Conference on Power Electronics and Applications (EPE ’09)*, pp. 1–8, Sept. 2009.

[81] N. Femia, G. Petrone, G. Spagnuolo, and M. Vitelli, “Optimization of perturb and observe maximum power point tracking method,” *IEEE Transactions on Power Electronics*, vol. 20, no. 4, pp. 963–973, July 2005.

[82] G. Kish, J. Lee, and P. Lehn, “Modelling and control of photovoltaic panels utilising the incremental conductance method for maximum power point tracking,” *Renewable Power Generation, IET*, vol. 6, no. 4, pp. 259–266, 2012.

[83] A. Safari and S. Mekhilef, “Simulation and hardware implementation of incremental conductance MPPT with direct control method using cuk converter,” *IEEE Transactions on Industrial Electronics*, vol. 58, no. 4, pp. 1154–1161, 2011.

[84] R. Faranda and S. Leva, “Energy comparison of MPPT techniques for PV systems,” *WSEAS Transactions on Power Systems*, vol. 3, no. 6, pp. 1–6, June 2008.

[85] M. Krstic and H. Wang, “Stability of extremum seeking feedback for general nonlinear dynamic systems,” *Automatica*, vol. 36, pp. 595–601, 2000.

[86] M. Guay, D. Dochain, and M. Perrier, “Adaptive extremum seeking control of continuous stirred tank bioreactors with unknown growth kinetics,” *Automatica*, vol. 40, pp. 881–888, 2004.

[87] G. Bastin, D. Nesic, Y. Tan, and I. Mareels, “On extremum seeking in bioprocesses with multivalued cost functions,” *Biotechnology Progress*, vol. 25, pp. 683–689, 2009.

[88] S. Drakunov, U. Ozguner, P. Dix, and B. Ashra, “A ABS control using optimum search via sliding modes,” *IEEE Transactions on Control Systems Technology*, vol. 3, pp. 79–85, 1995.

[89] D. Popovic, M. Jankovic, S. Manger, and A.R.Teel, “An extremum seeking methods for optimization of variable cam timing engine operation,” *Proceedings of American Control Conference (ACC03)*, pp. 3136–3141, June 2003.

[90] K. S. Peterson and A. G. Stefanopoulou, “An extremum seeking control for soft landing of an electromechanical valve actuator,” *Automatica*, vol. 40, pp. 1063–1069, 2004.

[91] H. Wang, S. Yeung, and M. Krstic, “Experimental application of extremum seeking on an axial-flow compressor,” *IEEE Transactions on Control Systems Technology*, vol. 8, pp. 300–309, 2000.

[92] C. Mayhew, R. Sanfelice, and A. Teel, “A robust source-seeking hybrid controllers for autonomous vehicles,” *Proceedings of Amererican Control Conference (ACC07)*, pp. 1185–1190, 2007.

[93] E. Biyik and M. Arcak, "A gradient climbing in formation via extremum seeking and passivity-based coordination rules," *Proceedings of 46th IEEE Conference of Decision and Control (CDC07)*, pp. 3133–3138, 2007.

[94] P. Ogren, E. Fiorelli, and N. Leonard, "Cooperative control of mobile sensor networks: adaptive gradient climbing in a distributed environment," *IEEE Transactions of Automatic Control*, vol. 49, pp. 1292–1302, 2004.

[95] P. Dower, P. Farrell, and D. Nesic, "An extremum seeking control of cascaded raman optical amplifiers," *IEEE Transactions on Control Technology*, vol. 16, pp. 396–407, 2008.

[96] J. Sternby, "An extremum control systems: An area for adaptive control," *Proceedings of International Symposium on Adaptive Systems*, vol. 24, pp. 151–160, 1980.

[97] K. B. Ariyur and M. Krstic, *Real-Time Optimization by Extremum-Seeking Control*. Hoboken: Wiley-Interscience, 2003.

[98] K. J. Astrom and B. Wittenmark, *Adaptive control*. Reading: Addison-Wesley, 1995.

[99] T. Hartley and C. Lorenzo, "Optimal fracitonal order damping," *Proceedings of Design Engineering Technical Conferences and Computers and Information in Engineering Conference (ASME03)*, pp. 737–743, Sept. 2003.

[100] Y. Tan, D. Nesic, and I. Mareels, "On stability properties of a simple extremum seeking scheme," *Proceedings of 45th IEEE Conference on Decision and Control (CDC06)*, pp. 2807–2812, Dec. 2006.

[101] Y.Tan, D. Nesic, and I. Mareels, "On non-local stability properties of extremum seeking control," *Automatica*, vol. 42, no. 6, pp. 889–903, 2006.

[102] R. Leyva, C. Olalla, H. Zazo, C. Cabal, A. Cid-Pastor, I. Queinnec, and C. Alonso, "MPPT based on sinusoidal extremum-seeking control in PV generation," *International Journal of Photoenergy*, vol. 98, no. 4, pp. 529–542, Apr. 2011.

[103] M. Krstic, "Performance improvement and limitations in extremum seeking control," *Systems and Control Letters*, vol. 39, no. 5, pp. 313–326, 2000.

[104] Y. Tarte, Y.-Q. Chen, W. Ren, and K. Moore, "Fractional horsepower dynamometer - A general purpose hardware-in-the-loop real-time simulation platform for nonlinear control research and education," *Proceedings of 45th IEEE Conference on Decision and Control (CDC06)*, pp. 3912–3917, Dec. 2006.

[105] E. Twining and D. Holmes, "Modeling grid-connected voltage source inverter operation," *Proceedings of Australasian Universities Power Engineering Conference (AUPEC01)*, Sept. 2001.

[106] S. Liu, T. Bi, A. Xue, and Q. Yang, "An optimal method for designing the controllers used in grid-connected PV systems," *Proceedings of IEEE International Conference on Power System Technology (POWERCON)*, pp. 1–6, 2012.

[107] bp solar Inc., *BP 365 Manual*, bp alternativenergy Inc., June 2009.

[108] D. Valerio, "Ninteger," Matlab Central File Exchange, Aug. 2005.

[109] Y. Q. Chen, "Impulse response invariant discretization of fractional order low-pass filters discretize [1/(ts + 1)]r with r a real number," Matlab Central File Exchange, 2008.

Vita

Hadi Malek

Personal Info

Email: hadi.malek@ieee.org

Interests: Control in Power Electronics, Renewable Energy Resources, Wireless Power Transfer.

Education

Ph.D. of Electrical Engineering, Dept. of Electrical and Computer Engineering, Utah State University, Logan, (Sep. 2010 - May 2013). (GPA: 4.00)

M.S. of Electrical Engineering, Dept. of Electrical Engineering, Ferdowsi University, Mashhad, (2005-2007). Thesis Title: "Stability Analysis of Nonlinear Fractional Order Systems." (GPA: 3.40)

B.Sc. of Electrical Engineering, Dept. of Electrical Engineering, Ferdowsi University, Mashhad (1996- 2002). Thesis Title: "Designing and Constructing a Mobile Robot." (GPA: 3.61)

Patents

- A. Kiani, H. Malek, M.R. Akbarzadeh T., "Sensorless Speed Controller for DC Motor Using Fractional Kalman Filter," Registration No. 39774, 2007.
- Hadi Malek, YangQuan Chen. "Fractional Order Power Point Tracking," US Non-provisional patent 20130268219, Docket Number: P12002.02. App No.: 13/859,394. (April 2013). Filed Apr 9, 2012.

- H.H. Wu, H. Malek, "Detection Method of Determining Physical Alignment Between Magnetic Couplers for Wireless Power Transfer Systems," Filed patent application, 2013.

Recent Publications

Journal Papers:

- H. Malek, Y.Q. Chen, "**BICO MPPT: A Faster Maximum Power Point Tracker & its Application for PhotoVoltaic Panels**," International Journal of Photoenergy, 2014.
- H. Malek, Y. Luo, Y.Q. Chen, "**Identification and tuning fractional order proportional integral controllers for time delayed systems with a fractional pole**," Mechatronics, No.7, Vol. 23, pp. 746-754, 2013.

Conference Papers:

- H. Malek, Y.Q. Chen, "**Fractional Order Maximum Power Point Tracker for Grid-connected Photovoltaic Systems**," 29th IEEE Applied Power Electronics Conference (APEC14), Forth-Worth,TX, March 2014 (Accepted).
- H. Malek, Y.Q. Chen, "**Fractional Order Controller in A Three Phase Grid-Connected PV Systems**," IEEE American Control Conference, Portland, OR, 2014 (Accepted).
- C. Coopmans, H. Malek, E. Spencer, "**Radiation and Impedance Characteristics of a Circular Loop Antenna Driven by Fractional Order Electronics**," International Design Engineering Technical Conferences (IDETC) and Computers and Information in Engineering Conference (CIE), Portland, OR, Aug. 2013.
- H. Malek, S. Dadras, Y.Q. Chen, "**An Improved Maximum Power Point Tracking Based on Fractional Order Extremum Seekingg Control in Grid Connected Photovoltaic (PV) Systems**," International Design Engineering Technical

Conferences (IDETC) and Computers and Information in Engineering Conference (CIE), Portland, OR, Aug. 2013.

- H. Malek, H. Wu, "**A Model for Calculating the Magnetic and Copper Losses of an Inductive Power Transfer (IPT) Pad**," 28th IEEE Annual Applied Power Electronics Conference and Exposition (APEC), Long Beach, CA, 2013.
- H. Malek, S. Dadras, Y.Q. Chen, "**A Fractional Order Maximum Power Point Tracker: Stability Analysis and Experiments**," IEEE Conference on Decision and Control, pp. 6861-6866, Maui, Hawaii, Dec. 2012.
- H. Malek, S. Dadras, R. Burt, J. Cook, Y.Q. Chen, "**Maximum Power Point Tracking Techniques For Efficient Photovoltaic Microsatellite Power Supply System**," Small Satellite Conference, Logan, UT, 2012.
- H. Malek, Y. Luo, Y.Q. Chen, "**Tuning Fractional Order Proportional Integral Controllers For Time Delayed System with a Fractional Order Pole**," International Design Engineering Technical Conferences and Computers and Information in Engineering Conference, Washingtion, USA, 2011.

Book Chapter:

- D. Huang, Y. Zheng and H. Malek, "**Solar Power Station Monitoring System with Five Remote Functions and Double Intelligent Control Loop**," Informatics in Control, Automation and Robotics, Lecture Notes in Electrical Engineering, vol. 133, pp. 27-34, 2012.